9

Strength and deformation of planetary lithospheres

David L. Kohlstedt

Department of Geology and Geophysics, University of Minnesota, Minneapolis

and

Stephen J. Mackwell

Lunar and Planetary Institute, Houston

Summary

Robotic missions to destinations throughout our solar system have illuminated in increasing detail evidence of past and present tectonics combined with manifestations of internal dynamics. Interpretation of observations, such as sustenance of high mountains on Venus for potentially hundreds of millions of years, formation of the grooved terrain on the surface of Ganymede, and tidally driven tectonics and volcanism on Io, requires the application of realistic constitutive equations describing the rheological properties for the materials that constitute the crusts and interiors of these planetary bodies. Appropriate flow laws can only be derived from careful experimental studies under conditions that may be reliably extrapolated to those believed to exist on and in the planetary body under consideration. In addition, knowledge of the appropriate rheological behavior may, coupled with measurements made from orbiting satellites, enable the determination of geophysical properties, such as heat flow, that are otherwise not quantifiable without an expensive surface mission. In this chapter, we review the current state of knowledge of the rheological properties of materials appropriate to understanding tectonic behavior and interior dynamics for the terrestrial planets as well as the major Jovian satellites. We then discuss the utility of experimentally constrained constitutive equations in understanding large-scale processes on Venus, Mars, Europa, Ganymede and Io.

1 Introduction

Historically, much of our understanding of the deformation behavior of planetary materials derives from experimental investigations undertaken to explore the mechanical properties of minerals and rocks as related to tectonic processes on

Planetary Tectonics, edited by Thomas R. Watters and Richard A. Schultz. Published by Cambridge University Press.

our own planet, Earth. Since the early 1980s, however, a few laboratory studies of rock strength have been undertaken specifically to address questions raised in the planetary community. In this chapter on strength and deformation of planetary lithospheres, we draw on examples from recent research related to the rheological properties of two planets and three planetary satellites. From these case studies and the larger body of literature for Earth, we develop the understanding of rock deformation necessary to analyze quantitatively the dynamic behavior of planetary bodies.

This chapter is laid out in four sections. In the first, we introduce the basic mechanisms and governing equations for flow of crystalline materials by examining the case of ice deformation within the context of Jupiter's icy satellites, Europa and Ganymede. In the second, we explore laboratory constraints on lithospheric strength, and we describe the concept of a strength envelope, which defines an upper limit to rock strength as a function of depth as applied to Earth's twin, Venus. In the third, we extend the constitutive flow equations to emphasize the role of water in the mechanical properties of nominally anhydrous silicate minerals within the framework of possible importance to the early history of Mars. In the fourth, we amplify on the effect of partial melting on the strength of rocks, a topic of central importance to deformation of Jupiter's moon, Io. Taken together, these four sections provide an integrated overview of the rheological behavior of rocks within the framework of the flow and strength of the lithospheres of planetary bodies.

1.1 Flow of rocks: Europa and Ganymede

The need for experimentally determined flow laws for water ice in understanding and interpreting planetary features and processes has become acute in the past several decades. Observations of the icy Galilean satellites from Voyager 1 and 2 in addition to Galileo reveal surfaces that have evolved significantly over time, with evidence of recent tectonic and potentially volcanic activity, as well as impact cratering. Europa and Ganymede are also believed to have icy shells overlaying liquid water layers, where conditions may be appropriate for the development of life. Experimentally determined rheological properties can be used to constrain the processes that formed these surface features, to model the ability of the surface to retain tectonic or impact structures, and even to allow determination of the thickness of the icy shells. Rheological (flow) laws are also useful in modeling the water-ice polar caps on Mars, and potentially provide useful constraints on flow of an icy regolith needed to understand the formation of features such as the large slumps evident on the flanks of Olympus Mons.

On Earth, the rheological properties of ice dictate the flow of glaciers and ice sheets. Hence, several laboratory and numerous field studies have explored in some

detail the flow behavior of ice I, the low-pressure phase of ice relevant to planetary bodies. This work has been extended with deformation experiments on ice in the broader context of planetary tectonics, first undertaken by Durham and colleagues (for a review, see Durham and Stern, 2001). In their ground-breaking work, these researchers developed a cryogenic high-pressure apparatus that allowed them to deform relatively coarse grained ice at reasonably high stresses entirely within the plastic flow regime, without the complications introduced by fracturing along grain boundaries that limited the applicability of results from earlier studies.

1.2 Mechanisms of deformation

As with other crystalline materials, ice deforms by several different mechanisms involving zero-dimensional (point), one-dimensional (line), and two-dimensional (planar) defects. That is, plastic deformation occurs by diffusion of ions, motion of dislocations, and sliding along grain boundaries. Broadly speaking, deformation mechanisms can be divided into two categories, those that are controlled by diffusion of ions (diffusion creep) and those that are governed by propagation (glide, climb, and cross slip) of dislocations (dislocation creep). In both cases, the relative motion of neighboring grains by ductile movement along their common interface (i.e., grain boundary sliding), a process regulated by ionic diffusion or dislocation motion, can be an essential process. For a given material such as ice, each deformation mechanism is characterized by a unique dependence of strain rate (viscosity) on parameters such as stress, grain size, temperature, and pressure. Hence, each mechanism will dominate over a limited range of these conditions. For example, as discussed below, diffusion creep tends to be most important in fine-grained rocks at low differential stresses, while dislocation creep often dictates the rate of deformation in coarse-grained rocks at larger differential stresses.

The flow behavior of a crystalline material is generally expressed in terms of its viscosity, η. In general, viscosity is a function of the imposed differential stress, σ, temperature, T, confining pressure, P, elements of the microstructure, S, and activities, a, or fugacities, f, of the chemical components expressed as (e.g., Evans and Kohlstedt, 1995)

$$\eta = \eta(\sigma, T, P, S_1, S_2, \ldots, a_1, a_2, \ldots, f_1, f_2, \ldots). \tag{9.1}$$

Microstructural elements include parameters such as grain size, subgrain size, texture and fabric, dislocation density, and, if more than one phase is present, their proportions, morphology, and distributions. For silicate minerals or rocks, chemical activities and fugacities of components include the activity of silica, a_{SiO_2}, and iron oxide, a_{FeO}, and fugacities include oxygen fugacity, f_{O_2}, and water fugacity, f_{H_2O}. In experimental studies of the flow behavior of ice and silicate rocks, deformation

results are frequently expressed in terms of strain rate, $\dot{\varepsilon}$, rather than viscosity, with the two quantities related by

$$\eta \equiv \frac{\sigma}{\dot{\varepsilon}} \cdot \tag{9.2}$$

1.2.1 Deformation by ionic diffusion coupled with grain boundary sliding

Diffusion creep can be divided into two regimes based on whether the diffusive flux is dominated by transport along grain boundaries or through grain matrixes (grain interiors). Both processes yield Newtonian viscosities, that is, viscosities that are independent of differential stress. Restated in terms of strain rate, the strain rate is linearly proportional to differential stress. Additionally, in both diffusion creep regimes, strain rate increases as the characteristic diffusion distance decreases, that is, with decreasing grain size. The strain rate – stress – grain size relationship thus takes the general form

$$\dot{\varepsilon}_{\text{diff}} \propto \frac{\sigma}{d^p} \cdot \tag{9.3}$$

Models predict a grain size exponent in Equation (9.3) of $p = 2$ if grain matrix (interior) diffusion dominates the diffusion flux (Nabarro, 1948; Herring, 1950) and $p = 3$ if grain boundary diffusion governs (Coble, 1963). These original formulations of the flow laws for diffusion creep considered deformation of a single spherical grain. Subsequent analyses have emphasized the importance of grain boundary sliding in polycrystalline materials as an essential part of diffusion creep (Liftshitz, 1963; Raj and Ashby, 1971). If grain boundaries are too weak to support shear stresses, the creep process can be considered to be one in which grain boundary sliding is accommodated by diffusion both through grain matrixes (interiors) and along grain boundaries. As is common, we refer to this deformation mechanism of grain boundary sliding with diffusion accommodation simply as diffusion creep.

Since grain boundary (gb*)* and grain matrix (gm) diffusion are independent/parallel processes, Equation (9.3) can be written to include the dependence of strain rate on the grain matrix and grain boundary diffusivities, D_{gm} and D_{gb} (Raj and Ashby, 1971):

$$\dot{\varepsilon}_{\text{diff}} = 14\left(\frac{\sigma V_{\text{m}}}{\text{R}T}\right)\left(D_{\text{gm}} + \pi\frac{\delta}{d}D_{\text{gb}}\right)\left(\frac{1}{d^2}\right), \tag{9.4}$$

where V_{m} is the molar volume, R is the gas constant, and δ is the grain boundary width; δ is on the order of 1 nm for most materials important in planetary applications (e.g., Carter and Sass, 1981; Ricoult and Kohlstedt, 1983). In diffusion creep, grain size and grain boundary width correspond to microstructural elements introduced in Equation (9.1).

The primary effects of temperature and pressure on creep rate (viscosity) enter through the grain matrix and grain boundary diffusivities both of which have the form

$$D_{\mathrm{gm/gb}} = D^{\mathrm{o}}_{\mathrm{gm/gb}} \exp\left(-\frac{E_{\mathrm{gm/gb}} + PV_{\mathrm{gm/gb}}}{\mathrm{R}T}\right), \tag{9.5}$$

where $E_{\mathrm{gm/gb}}$ and $V_{\mathrm{gm/gb}}$ are the activation energy and activation volume, respectively, for grain matrix or grain boundary diffusion. With decreasing grain size, the contribution of grain boundary diffusion to deformation becomes more significant than the contribution due to grain matrix diffusion. This point is captured in Equation (9.4) since $\dot{\varepsilon}_{\mathrm{gb}} \propto 1/d^3$, while $\dot{\varepsilon}_{\mathrm{gm}} \propto 1/d^2$. Furthermore, based on Equation (9.5), grain boundary diffusion contributes more to the creep rate than does grain matrix diffusion at low temperatures since normally $E_{\mathrm{gb}} < E_{\mathrm{gm}}$.

1.2.2 Deformation by dislocation processes

Several distinct mechanisms for deformation by dislocation motion – which takes place by glide, climb and cross slip – have been considered in the materials science literature; compilations and descriptions of dislocation creep mechanisms are recorded in Poirier (1985) and Evans and Kohlstedt (1995). In this chapter, we will primarily discuss glide, in which dislocations move in their slip or glide plane, and climb, in which dislocations require diffusion to move normal to their slip plane. Broadly, dislocation mechanisms of deformation can be divided into low-temperature processes in which dislocation glide dominates and high-temperature mechanisms in which dislocation climb controls the rate of deformation (Weertman, 1999). Laboratory and field studies of the rheological behavior of ice I have generally emphasized the latter in analyses of deformation results.

At high temperatures (roughly $T \geq T_{\mathrm{m}}/2$), dislocation climb as well as glide and cross slip contribute to deformation. The bulk of the strain results from dislocation glide, while the strain rate is controlled by climb or cross slip. Flow laws in this dislocation creep regime are generally written in the form of a power law (Weertman, 1999):

$$\dot{\varepsilon}_{\mathrm{disl}} = \mathrm{A}_{\mathrm{disl}}\,\sigma^{n} \exp\left(-\frac{E_{\mathrm{disl}} + PV_{\mathrm{disl}}}{\mathrm{R}T}\right). \tag{9.6}$$

In the dislocation creep regime, the stress exponent typically lies in the range $3 \leq n \leq 5$. Strain rate does not depend on grain size, provided that there are a sufficient number of slip systems to fulfill the von Mises (1928) criterion (discussed below) or, at least, the relaxed von Mises criterion (Paterson, 1969). In this case, viscosity is non-Newtonian, that is, a function of differential stress. For many materials, the activation energy for dislocation creep is equal to the activation

energy for grain matrix diffusion; this observation holds for ice for which the activation energy for dislocation creep is equal to that for self-diffusion of either hydrogen or oxygen (Weertman, 1983). Therefore, the strain rate is written as a function of the grain matrix diffusion coefficient

$$\dot{\varepsilon} \propto D_{\mathrm{gm}} \propto \exp\left(-\frac{E_{\mathrm{gm}} + PV_{\mathrm{gm}}}{\mathrm{R}T}\right), \tag{9.7}$$

suggestive of an important role of dislocation climb in controlling the rate of plastic deformation (Weertman, 1968, 1999).

For ice and rock samples with irregular, three-dimensional grain shapes to deform homogeneously by dislocation creep without dilatation resulting from the formation of cracks or voids, several slip systems must simultaneously operate in all of the grains in the aggregate. Based on purely geometric arguments, von Mises (1928) demonstrated that five independent slip systems must operate within each mineral grain for homogeneous deformation. The bulk of the strain can be accommodated by glide on two or three of the slip systems, while the other slip systems take up only minor amounts of strain in order to minimize strain heterogeneity and avoid development of cracks and voids. In this case, the aggregate strength is expected to lie intermediate between the strengths of the weakest and the strongest of the required slip systems and to have constitutive parameters dominated by the strongest required slip system. If deformation occurs by climb as well as glide, three slip systems suffice for homogeneous deformation (Groves and Kelly, 1969). Similarly, processes such as grain boundary and grain matrix diffusion as well as grain boundary sliding often serve as a further accommodation process, hence necessitating fewer active slip systems. If grain boundary sliding contributes to the deformation, the aggregate flow law may show a dependence on grain size, consistent with the enhanced role of this process at finer grain sizes.

Many metals and some ceramics are composed of crystalline grains with high symmetry, such that the von Mises criterion is easily met. However, in most rocks, the crystalline grains have relatively low symmetry and, hence, the number of active slip systems is limited. Thus, despite the relative weakness of the easiest slip system in a mineral, the aggregate strength may be very high due to the necessity for dislocation glide on an energetically unfavorable slip system. For example, in ice, slip is significantly easier on the basal plane than on non-basal slip systems. Activation of non-basal slip in single crystals requires stresses a factor of 10 to 100 greater than required for the basal slip system. The strength of polycrystalline ice with a coarse grain size ($\sim$1–10 mm) lies between that of single crystals oriented for basal slip, with dislocations gliding on the basal plane of ice, and those oriented for non-basal slip, as illustrated in the log–log plot of strain rate as a function of differential stress in Figure 9.1.

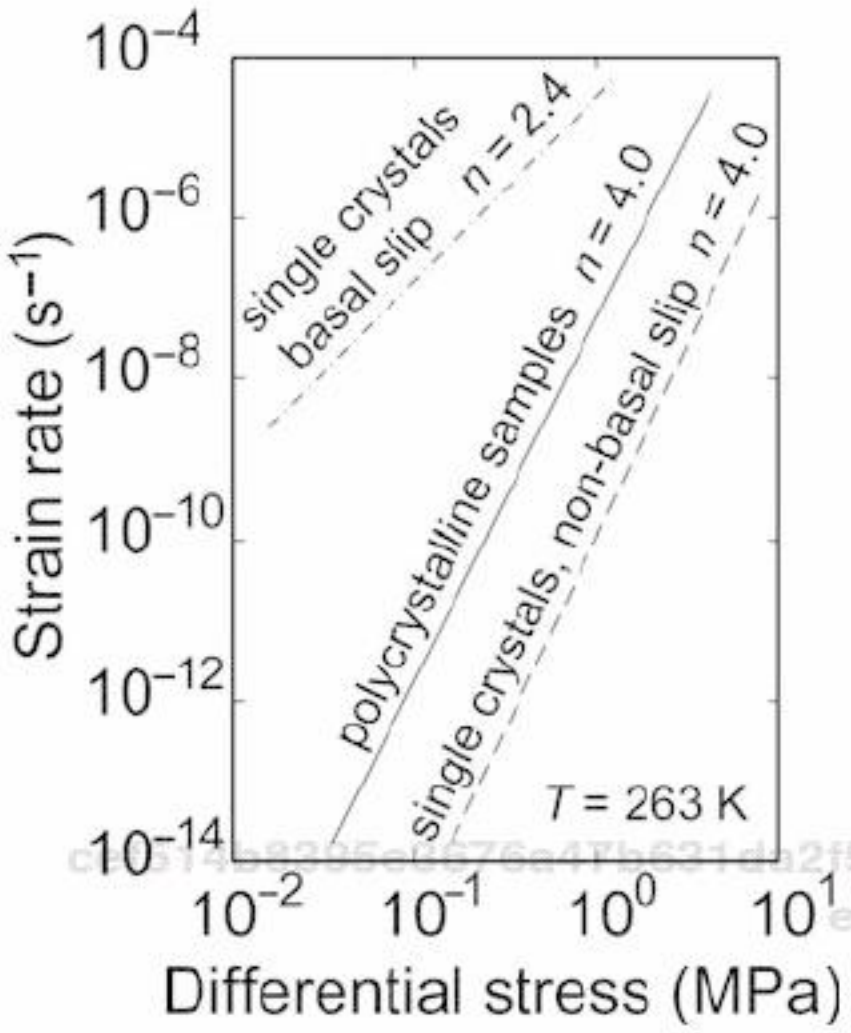

Figure 9.1. Log–log plot of strain rate as a function of differential stress, illustrating the strength of coarse-grained polycrystalline ice relative to that of single crystals of ice oriented for slip on the basal plane and single crystals of ice oriented for slip on non-basal planes. Note that the differential stress required to deform polycrystalline samples at a given strain rate lies between the values for slip on the hard and easy slip systems in ice. Comparison of the slopes, that is, the stress exponent n, in Equation (9.6), of these three lines suggests that slip on non-basal systems controls the rate of deformation, while the relative positions of the lines indicates that basal slip contributes significantly to flow. Modified from Goldsby and Kohlstedt (2001).

The significant contrast in strength of the various slip systems in minerals such as ice means that strain-producing, non-dislocation processes may become active at stresses below those required to activate the stronger slip systems. In particular, grain boundary sliding can be very important in ice and rock samples deforming by dislocation creep. As the rate of grain boundary sliding depends on the size of the sliding interface, this phenomenon displays a dependence on grain size, with finer grain sizes favoring the activation of grain boundary sliding. Grain boundary sliding is also often characterized by a smaller value of the stress exponent than observed in dislocation creep. The resultant flow law will otherwise closely resemble a standard flow law for dislocation (power-law) creep.

1.2.3 Deformation by dislocation processes coupled with grain boundary sliding

As in the diffusion creep regime, grain boundary sliding can contribute significantly to deformation in the dislocation creep regime, such that it is appropriate to discuss a creep regime in which dislocation motion is accompanied by grain boundary sliding. In detail, grain boundary sliding in the dislocation creep regime differs from that in the diffusion creep regime due to movement of dislocations along grain boundaries; hence, in this regime, grain boundary sliding is sometimes referred to as enhanced or "stimulated" grain boundary sliding (Kaibyshev, 1992). In this regime, termed here the dislocation – grain boundary sliding (disl–gbs) regime, strain rate is again a function of grain size, as well as a non-linear function of differential stress:

$$\dot{\varepsilon}_{\text{disl–gbs}} = \mathrm{A}_{\text{disl–gbs}} \frac{\sigma^n}{d^p} \exp\left(-\frac{E_{\text{disl–gbs}} + PV_{\text{disl–gbs}}}{\mathrm{R}T}\right). \tag{9.8}$$

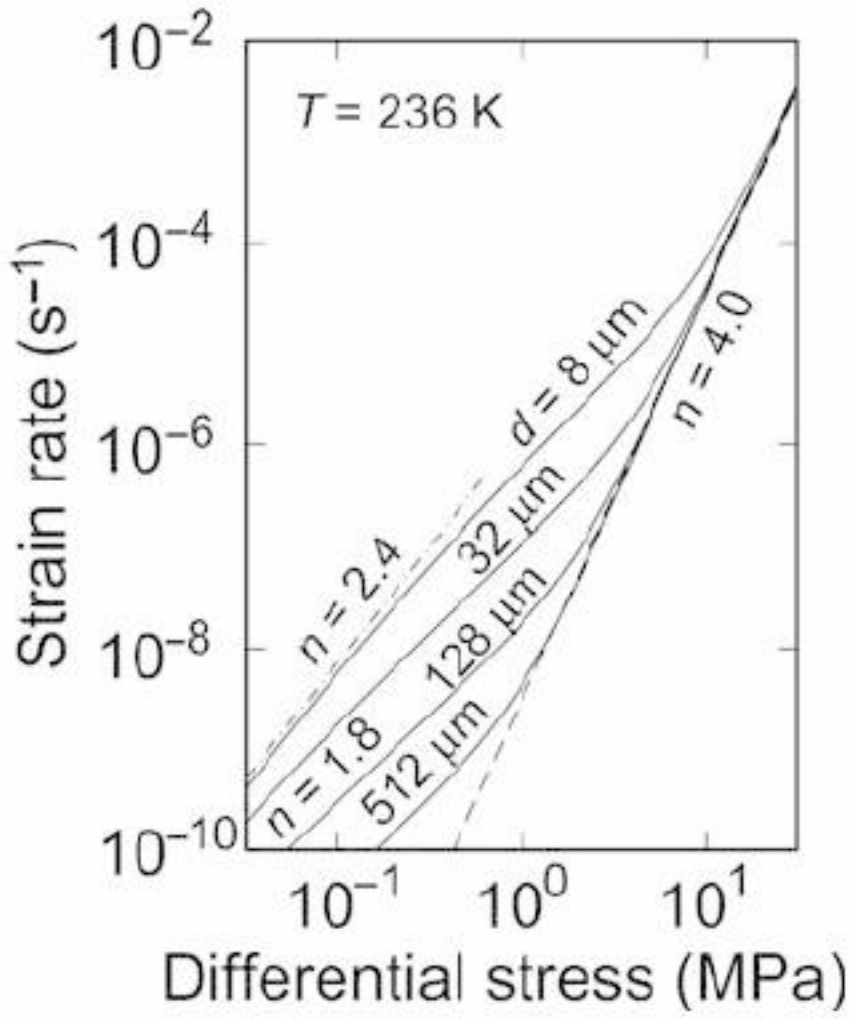

Figure 9.2. Log–log plot of viscosity as a function of differential stress for fine-grained polycrystalline ice with grain sizes of 8, 32, 128, and 512 μm. The flow law for coarse-grained ice deforming in the dislocation creep regime is indicated by the dashed line of slope $n = 4.0$, while the flow law for single crystals of ice oriented for slip on the basal plane is included as a dot-dashed line of slope $n = 2.4$. Between these two bounds, polycrystalline ice flows by grain boundary sliding accommodated by dislocation movement in the dislocation – grain boundary sliding regime characterized by a slope of $n = 1.8$.

Models for this creep regime yield values of $n = 2$, $p = 2$ and $n = 3$, $p = 1$ (Gifkins, 1972; Langdon, 1994), where the former values of n and p were derived for the case in which grains are free of subgrains (sometimes stated as "grain size smaller than subgrain size"), while the latter pair of values applies when the grain size is larger than the subgrain size. Laboratory experiments demonstrate that flow of fine-grained ice is, in fact, characterized by $n = 1.8$ and $p = 1.4$ (Goldsby and Kohlstedt, 2001; Durham *et al.*, 2001). As illustrated in Figure 9.2, the dislocation – grain boundary sliding regime dominates flow at low differential stresses and finer grain sizes, while dislocation creep dominates at higher differential stresses and coarser grain sizes. As grain size increases, the transition from dislocation creep to dislocation – grain boundary sliding creep moves to lower differential stresses. At the low differential stresses ($\leq$0.1 MPa) appropriate for glaciers, the flow behavior of coarse-grained ice observed in *in situ* field studies is dominated by the dislocation – grain boundary sliding flow law determined from laboratory experiments (Goldsby, 2006).

1.2.4 Creep of ice I

A constitutive equation describing the creep of ice thus consists of at least three flow regimes. Diffusion creep, dislocation creep, and dislocation – grain boundary sliding creep operate largely independently. Thus, the constitutive equation has the form

$$\dot{\varepsilon} = \dot{\varepsilon}_{\text{diff}} + \dot{\varepsilon}_{\text{disl-gbs}} + \dot{\varepsilon}_{\text{disl}}. \tag{9.9a}$$

As diffusion creep appears to operate at differential stresses and grain sizes well below those explored in the laboratory and those appropriate for flow in glacial

and planetary ice bodies, we eliminate this term from Equation (9.9a). In addition, Goldsby and Kohlstedt (2001) have argued that the dislocation – grain boundary sliding regime can be viewed as the operation of two interdependent/serial processes: basal glide and grain boundary sliding. Therefore, in Figure 9.2, at a given grain size and strain rate, the mechanism of deformation changes from dislocation creep ($n = 4.0$) to grain boundary sliding controlled creep ($n = 1.8$). Goldsby (2006) has suggested that for $d > 1$ mm, $\sigma > 10^{-4}$ MPa, and $T > 220$ K, the flow of ice can be well described by simplifying Equation (9.9a) to

$$\dot{\varepsilon} \approx \dot{\varepsilon}_{\text{disl–gbs}} + \dot{\varepsilon}_{\text{disl}}, \tag{9.9b}$$

where $n = 1.8$, $p = 1.4$ in the dislocation – grain boundary sliding regime and $n = 4.0$, $p = 0$ in the dislocation creep regime.

Deformation experiments undertaken to study the flow of ice with applications to satellites of the outer planets have built on an extensive literature in the glaciology field (see references in Durham and Stern, 2001; Goldsby, 2006; Iverson, 2006). In turn, recent experiments on ice designed to investigate the tectonic behavior of icy satellites, such as Europa and Ganymede, have impacted investigations of flow of ice sheets and glaciers (e.g., Cuffey *et al.*, 2000a,b). Prior to the late 1990s, the results of much of the work on the rheological properties of ice were interpreted in terms of creep in the dislocation regime as given by an equation of the form of Equation (9.6). In this regime, flow of ice was earlier described with a stress exponent of $n = 3$ with $E = 139$ kJ/mol, following the work of Glen (1952, 1955). An extensive series of experiments by Durham *et al.* (1983, 1997) at high pressures, however, demonstrated that values of $n = 4.0$ and $E = 61$ kJ/mol are more appropriate in the dislocation creep regime.

Within the past decade, a concerted effort has been made to explore the diffusion creep regime of ice. Since diffusion creep is expected to dominate over dislocation creep in fine-grained samples, cylinders of ice I were cycled from ice I to ice II and then back to ice I by increasing and then rapidly decreasing pressure (Stern *et al.*, 1997). Nucleation of new grains upon crossing the phase boundary resulted in ice grains a few microns across. To explore the effect of grain size on creep rate, samples were systematically heated for prescribed times to promote grain growth. While these experiments failed to identify a diffusion creep regime with $n = 1$ and $p = 3$, they did encounter an extended creep regime within which strain rate was markedly dependent on grain size (Goldsby and Kohlstedt, 2001; Durham *et al.*, 2001). As described above, this grain size sensitive creep regime is characterized by robust values for the stress exponent of $n = 1.8$ and the grain size exponent of $p = 1.4$ with an activation energy of 49 kJ/mol. The presence of numerous four-grain junctions in deformed samples (as opposed to three-grain junctions found in textural equilibrium) suggests that grain boundary sliding and grain switching

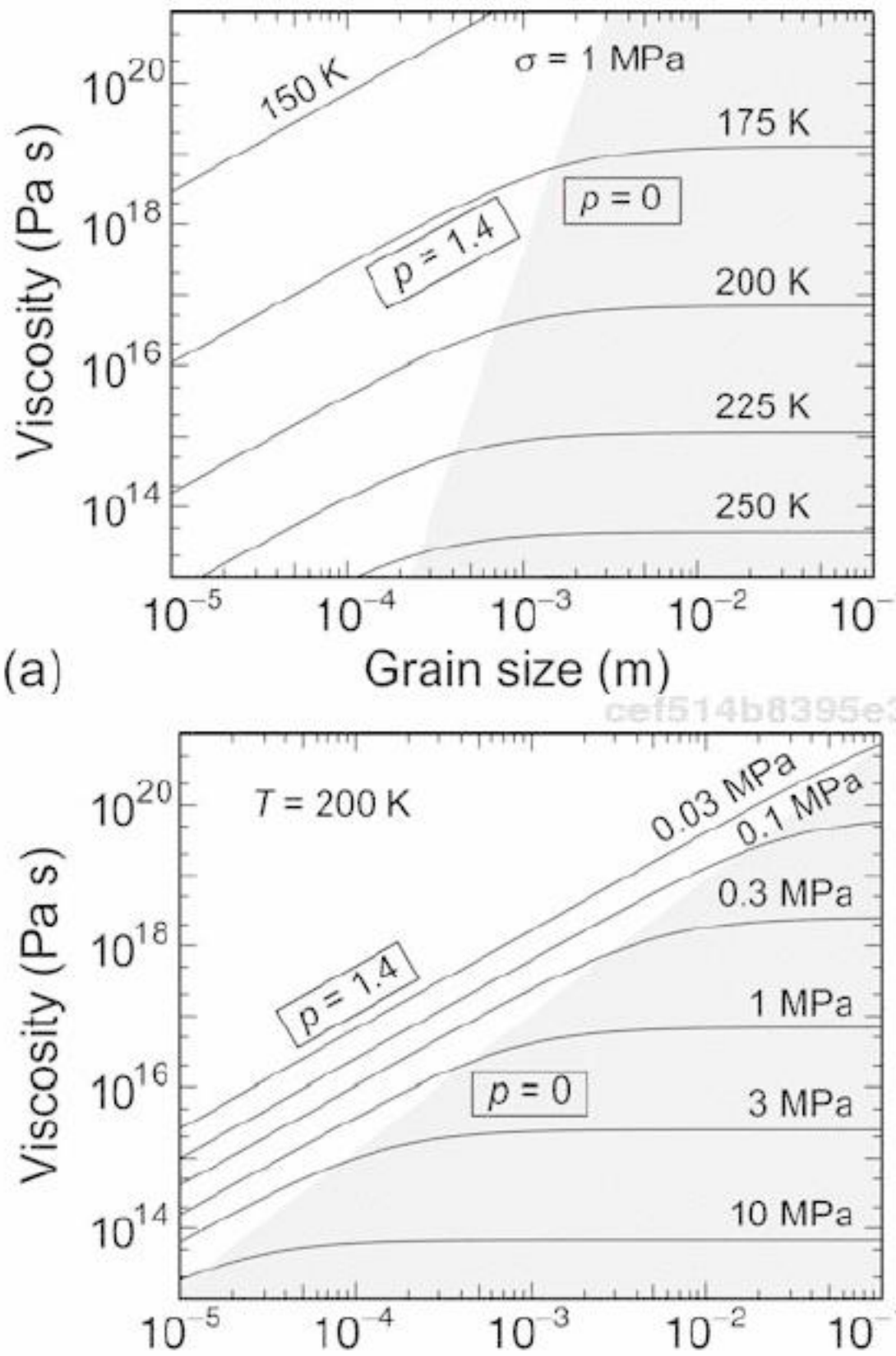

Figure 9.3. Log–log plots of viscosity as a function of grain size at (a) fixed differential stress of 1 MPa and (b) fixed temperature of 200 K. Dislocation creep dominates the viscosity at large grain sizes (shaded regions on the right of (a) and (b)), while dislocation – grain boundary sliding creep dominates at smaller grain sizes. Strain rate is independent of grain size ($p = 0$) in the former regime, while strain rate increases with decreasing grain size in the latter regime ($p = 1.4$). In (a), the transition between the two regimes occurs at smaller grain size with increasing temperature. In (b), the transition between the two regimes occurs at smaller grain size with increasing differential stress.

events played an important role. Hence, this regime was identified as one in which dislocation creep is accompanied by grain boundary sliding, as described by Equation (9.8).

The effects of temperature, differential stress, and grain size on the flow of ice due to the combined effects of dislocation creep and dislocation – grain boundary sliding as described by Equation (9.9b) are illustrated in the log–log plots of viscosity as a function of grain size in Figures 9.3a and 9.3b. These figures explore the effect of activation energy (temperature dependence), stress exponent

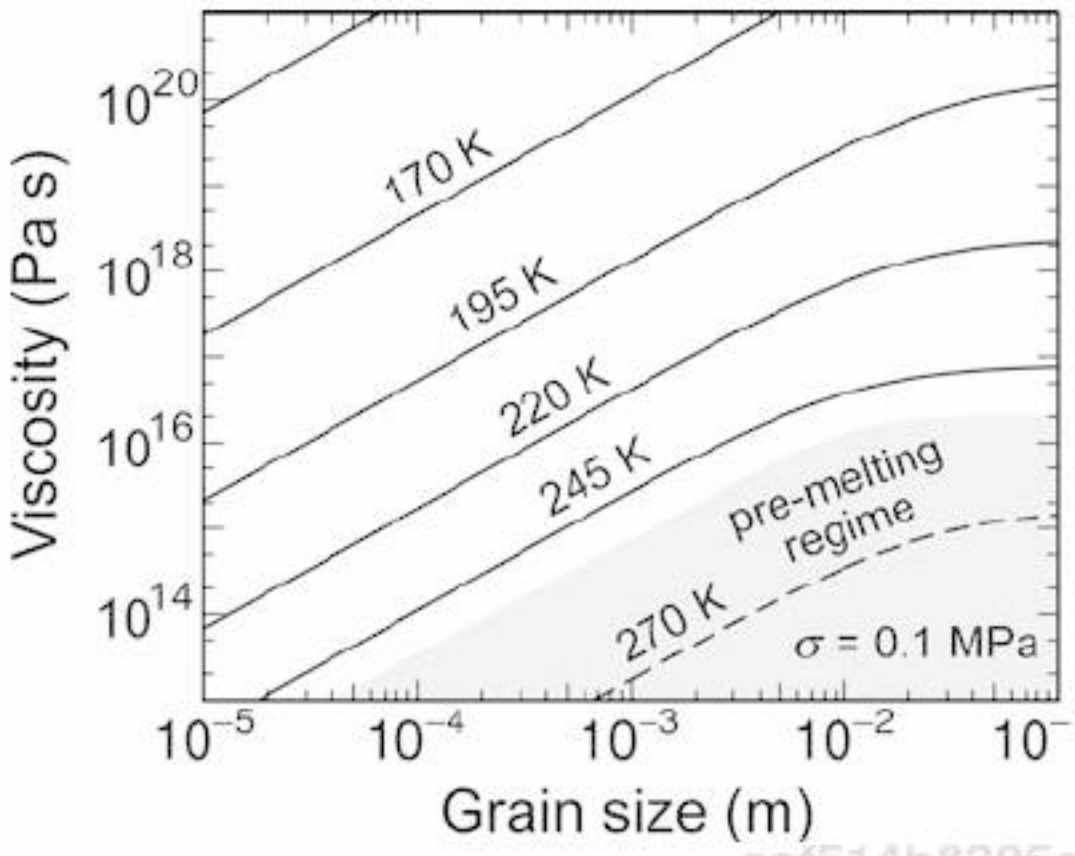

Figure 9.4. Log–log plot of strain rate as a function of grain size at a constant differential stress of 0.1 MPa for temperatures both below and above the pre-melting temperature of ~255 K. The temperature interval between constant-temperature curves is 25 K. With increasing temperature between 170 and 245 K, the contours become progressively closer. However, the spacing between the curve for 245 K and the curve for 270 K is significantly wider than that between the curves for 220 K and 245 K, reflecting the marked increase in activation energy from ~50 to ~180 kJ/mol in crossing the pre-melting point.

(stress dependence), and grain size exponent (grain size dependence) on creep rate. In both Figures 9.3a and 9.3b, the contribution to the plastic flow from the grain-size sensitive, dislocation – grain boundary sliding creep regime increases with decreasing grain size. Based on Figure 9.3a, the dislocation creep regime extends to lower grain size as temperature increases, reflecting the higher activation energy in this regime. Based on Figure 9.3b, the dislocation creep regime extends to smaller grain sizes at higher stress because the stress exponent is larger in the dislocation creep regime ($n = 4.0$) than in the dislocation – grain boundary sliding regime ($n = 1.8$).

Above ~255 K, the flow behavior of ice is dramatically affected by the apparent onset of pre-melting at grain boundaries (Duval *et al.*, 1983; Dash *et al.*, 1995). Deformation of ice occurs more rapidly for a given grain size and temperature than predicted from experimental data obtained at lower temperatures. The disproportionately large decrease in viscosity at temperatures above 255 K is clear in the log–log plot of viscosity as a function of grain size in Figure 9.4. The apparent activation energy at $T > 255$ K increases to ~180 kJ/mol in the diffusion creep regime and to ~190 kJ/mol in the dislocation – grain boundary sliding creep regime (Goldsby and Kohlstedt, 2001). A detailed summary of flow law parameters is presented in Table 1 of Durham and Stern (2001) and in Goldsby (2006).

1.3 Application to Europa and Ganymede

The constitutive equation describing the flow of ice I has been used in analyses of the tectonic behavior of Europa and Ganymede. Two problems related to the topography on Ganymede have been analyzed based on the combined flow laws for dislocation and dislocation – grain boundary sliding creep in ice I. First, the upper limit on the relaxation time for impact craters was calculated based on flow by solid-state creep. Apparent retention ages for craters on Ganymede are $\leq$1 Gyr (Passey and Shoemaker, 1982; Zahnle *et al.*, 1998). Finite element models of crater relaxation lead to the conclusion that crater topography can be sustained against viscous relaxation for billions of years, consistent with observation (Dombard and McKinnon, 2000). Second, formation of grooved terrain on Ganymede as a result of extensional plastic instability has been examined. Early analysis of this problem based on dislocation flow of ice led to the conclusion that a necking instability could not explain the ridge–trough topographic relief (Herrick and Stevenson, 1990). However, models including the grain-size sensitive, dislocation – grain boundary sliding creep regime yielded instabilities with topographic wavelengths consistent with those observed for the grooved terrain on Ganymede (Dombard and McKinnon, 2001).

Laboratory-determined flow properties of ice also provide constraints on the tectonic behavior of the ice shell on Europa (McKinnon, 1999; Ruiz and Tejero, 2000, 2003; Barr *et al.*, 2004). Models have examined the possibility of convection in a thin ice shell as a mechanism for transporting heat efficiently to the surface, as opposed to heat flow entirely by conduction. The results of these models depend critically on the flow laws used to characterize ice deformation. For example, Ruiz and Tejero (2003) conclude that convection could occur in the ice shell on Europa, accounting for the high heat flow associated with tidal heating, only if ice deforms primarily by the dislocation – grain boundary sliding mechanism. These researchers further conclude that the thickness of the ice shell is in the range ~15 to 50 km, consistent with morphology and size of impact craters (Schenk, 2002).

2 Strength envelopes: Venus

In the dynamics of Earth and other planetary bodies, many of the most fundamental processes that we seek to understand involve solid-state deformation of minerals and rocks. To model this behavior adequately, we must understand the processes involved in deformation as appropriate to the planetary setting and, when possible, utilize experimentally derived data to constrain the models. Application of experimental results is not always feasible due to limitations of the models, computational constraints, or uncertainty about the nature and conditions in the regions

under consideration. However, utilization of experimentally derived mechanical data in problems of planetary dynamics and tectonics will usually provide a greater understanding than simplified models, whether or not a perfect fit to observation is obtained. Models incorporating experimental results that clearly do not fit observational data also provide important constraints on planetary processes.

Application of experimentally derived and field-correlated mechanical property data for minerals and rocks to processes in planetary interiors requires an understanding of both the nature of the planetary body and the limitations of the experiments themselves. Injudicious application of experimental data in planetary models generally leads to inappropriate conclusions and, ultimately, to an underestimation of the true merit of experimental work. At the simplest level, experimental measurements can be applied to issues of rheological behavior through illustrations of strength distributions in the lithosphere, such as the strength envelope concept (Sibson, 1977; Goetze and Evans, 1979; Brace and Kohlstedt, 1980; Kohlstedt *et al.*, 1995). In such diagrams, the strength of rock is plotted against depth in the planetary body, under the assumptions of uniform lateral distribution of deformation, constant rate of deformation with depth, and a specific dependence of temperature on depth. Such models, though simple, allow an appreciation of issues such as depth of the seismogenic zone, integrated strength of the lithosphere, identification of zones of maximum strength in the lithosphere, distribution of vertically stratified zones of weakness, and potential detachment of crust and mantle. However, these simplified models include assumptions that will not hold in all environments. For example, rheological properties describing plastic flow, which define the behavior at depths greater than a few kilometers, are strongly temperature dependent, making the selection of an appropriate temperature profile critical. Also, the use of a depth-independent strain rate on the assumption of uniform lateral distribution of deformation ignores the abundant evidence of plastic shear zones in the continental crust of Earth. Water also has a major effect on mechanical properties for all deformation processes and with all lithologies. However, water may be present only episodically, and fluid pressures may vary significantly both laterally and vertically.

In addition, most rocks within the interior of the terrestrial planets are polyphase aggregates, composed of several minerals in differing volumetric ratios, each with characteristic morphologies and mechanical properties. Aggregate behavior will be a complex integration of the properties of individual phases with contributions due to interactions between phases (for example, interphase boundaries have very different properties than grain boundaries). For deformation in the convecting upper mantle of the terrestrial planets, dislocation creep can be reasonably approximated by the behavior of polycrystalline olivine (Zimmerman and Kohlstedt, 2004), as olivine is the predominant and weakest major mineral. However, such simplifications are not always possible, and rocks of gabbroic composition have rheologies

that require a volumetric averaging of the behavior of the pyroxene and plagioclase feldspar components (Mackwell *et al.*, 1998). Consequently, strength envelopes based on single mineral flow behavior may not adequately model flow at depth. In summary, application of strength envelopes must be made judiciously with as complete an understanding of the thermal, tectonic, hydrologic, and lithologic setting as is possible, and using the appropriate flow laws.

2.1 The strength envelope model

2.1.1 Brittle deformation

In strength envelope models, deformation in the most shallow portion of the lithosphere is governed by sliding on existing fault surfaces, as described by Byerlee's law (Byerlee, 1978). For a fault with a normal at 60° from the maximum principal stress, σ_1, Byerlee's law can be written as (Sibson, 1974; Brace and Kohlstedt, 1980; McGarr *et al.*, 1982; McGarr, 1984; Kohlstedt *et al.*, 1995)

$$\sigma_1 - P_P = 4.9(\sigma_3 - P_P) \qquad \sigma_3 - P_P < 100\,\text{MPa} \tag{9.10a}$$

$$\sigma_1 - P_P = 3.1(\sigma_3 - P_P) + 210 \qquad \sigma_3 - P_P > 100\,\text{MPa}, \tag{9.10b}$$

where σ_3, the minimum principal stress, equals the lithostatic pressure, and P_P is the pore pressure. The stress supported by a rock mass deforming by frictional sliding depends predominantly on the lithostatic pressure, is largely independent of temperature and strain rate, and, to first order, does not vary substantially between rock types. Of course, the maximum principal stress that can be supported by frictional sliding is limited. If the fracture strength, σ_f, is reached, by an increase either in the local stress or in the pore fluid pressure, the rock may deform by cataclasis, rather than localized sliding on preexisting faults (see e.g., Kohlstedt *et al.*, 1995).

2.1.2 Semi-brittle deformation

Semi-brittle deformation becomes important at stresses lower than the fracture stress when dislocation glide becomes activated at points of stress concentration and/or when fluid-assisted grain boundary diffusion (pressure solution creep) allows some relaxation of the stress. While some attempts have been made to quantify the boundary between fully brittle (frictional sliding or fracture) and semi-brittle (brittle plus plastic) behavior (e.g., Chester, 1988), we will follow the observation-based assumption from Kohlstedt *et al.* (1995) that semi-brittle behavior is initiated when the plastic flow strength of the rock is about five times the frictional strength. This transition stress is often referred to as the brittle–ductile transition (BDT).

As depth increases, increasing temperature enables a transition from semi-brittle processes to fully plastic flow, which is only possible if the lithostatic pressure, σ_3, is sufficient to suppress brittle processes. This stress-induced transition (referred to as the Goetze criterion, C. Goetze, private communication, 1975; Kohlstedt *et al.*, 1995) occurs approximately when

$$\sigma_1 - \sigma_3 = (\sigma_3 - P_P). \tag{9.11}$$

This criterion defines the maximum differential stress ($\sigma_1 - \sigma_3$) that can be supported by a rock through purely plastic processes and defines the brittle–plastic transition (BPT). Between the BDT and the BPT, the strength of the rocks is rather ill-defined, as a range of brittle and plastic processes all contribute to deformation (Evans and Kohlstedt, 1995; Kohlstedt *et al.*, 1995). In this region, the strength envelope defined by the end-member behaviors alone will provide only an upper limit on lithospheric strength, particularly at the highest strength regions. Deformation is likely to be localized, as often observed in the field, for example, in the form of mylonites (e.g., Sibson, 1977).

2.1.3 Plastic flow

At depths at which the temperature is high enough for purely plastic processes to dominate, deformation of the rocks is controlled by micro-mechanical mechanisms such as dislocation glide, dislocation climb, and diffusion creep (see, e.g., Poirier, 1985; Kohlstedt *et al.*, 1995). In this regime at lower temperatures and higher stresses, dislocation glide dominates; dislocations within individual mineral grains are constrained to move along crystallographically controlled glide planes. At higher temperatures, diffusion becomes fast enough to enable diffusion creep and to promote dislocation creep processes that involve both climb and glide of dislocations, with diffusion-controlled climb rate-limiting deformation. For rocks with relatively large grain sizes, dislocation creep is likely to control aggregate behavior, whereas for rocks with finer grain sizes, diffusion creep is favored. As dislocations are crystallographically controlled and move on glide planes, homogeneous deformation of an aggregate by dislocation processes requires motion of dislocations on multiple slip systems, as delineated by von Mises (1928) and discussed in the sections on Europa and Mars. As the minerals that comprise the dominant rock types in the interior of terrestrial planets generally lack a sufficient number of easy slip systems for deformation to occur homogeneously, some additional component of strain accommodation, such as grain boundary sliding or diffusion, is usually required. Both diffusion and dislocation creep processes are thermally activated and can be described by a flow law (see section on Europa and, e.g., Kohlstedt *et al.*, 1995) with an Arrhenius dependence of strain rate on temperature and pressure, as described by Equations (9.5–9.8). Strain rate may also depend on other

aspects of the thermodynamic environment, such as oxygen fugacity (for iron-bearing silicates), activity of component oxides, and water fugacity. For example, in the dislocation creep regime, mantle olivine deforms a factor of ~8 faster when oxygen fugacity is buffered near Fe/FeO than when buffered at Ni/NiO (Keefner *et al.*, 2005).

2.1.4 Water weakening

Water is known to produce a weakening of rock throughout Earth's interior in the brittle, brittle–plastic, and plastic deformation regimes. At shallow depths, weakening results from a decrease in the loading across fault surfaces due to the fluid pressure; at greater depths it may result from weakening of fault surfaces due to the presence of platy hydrous minerals with easy cleavage planes parallel to the fault plane, or due to decreases in the intracrystalline or intercrystalline strength of the minerals/rocks themselves. In particular, the presence of water has been observed to reduce the high-temperature strength of most silicates, including quartzite (Gleason and Tullis, 1995; Post *et al.*, 1996), feldspar (Rybacki and Dresen, 2000), pyroxene (Ross and Nielsen, 1978; Bystricky and Mackwell, 2001; Chen *et al.*, 2006), and olivine (Chopra and Paterson, 1984; Mackwell *et al.*, 1985; Karato *et al.*, 1986; Mei and Kohlstedt, 2000a,b; Karato and Jung, 2003; see also section on Mars). This weakening effect has been correlated to increased rates of dislocation climb within mineral grains, as well as enhanced rates of intracrystalline (grain matrix) diffusion and grain boundary diffusion. In addition, increased water activity enhances grain growth and recovery processes such as recrystallization, which also affect the mechanical behavior of a rock mass. Thus, any model for deformation of the interior of a planetary body must allow for the possible role of water.

2.1.5 Strength envelope for oceanic lithosphere

Oceanic crust on Earth is composed of rocks derived from basalt; as such, mechanical properties appropriate to basaltic or gabbroic rocks should provide a reasonable approximation to the behavior of this region. However, the ocean crust is relatively thin (~6 km), and quite cold, so that deformation is primarily brittle and occurs by frictional sliding on systems of faults. Fluid circulation occurs to significant depths (Ranero *et al.*, 2003), decreasing the effective pressure within the fault zones. Also, the presence of aqueous fluids results in the formation of hydrous minerals, such as serpentine, which lower the coefficient of friction within the fault zone (Escartin *et al.*, 1997).

Even well into the oceanic upper mantle, deformation by fully plastic processes is not anticipated on the basis of experimental studies of deformation in mantle rocks. It is worth noting that seismic studies have recognized the presence of

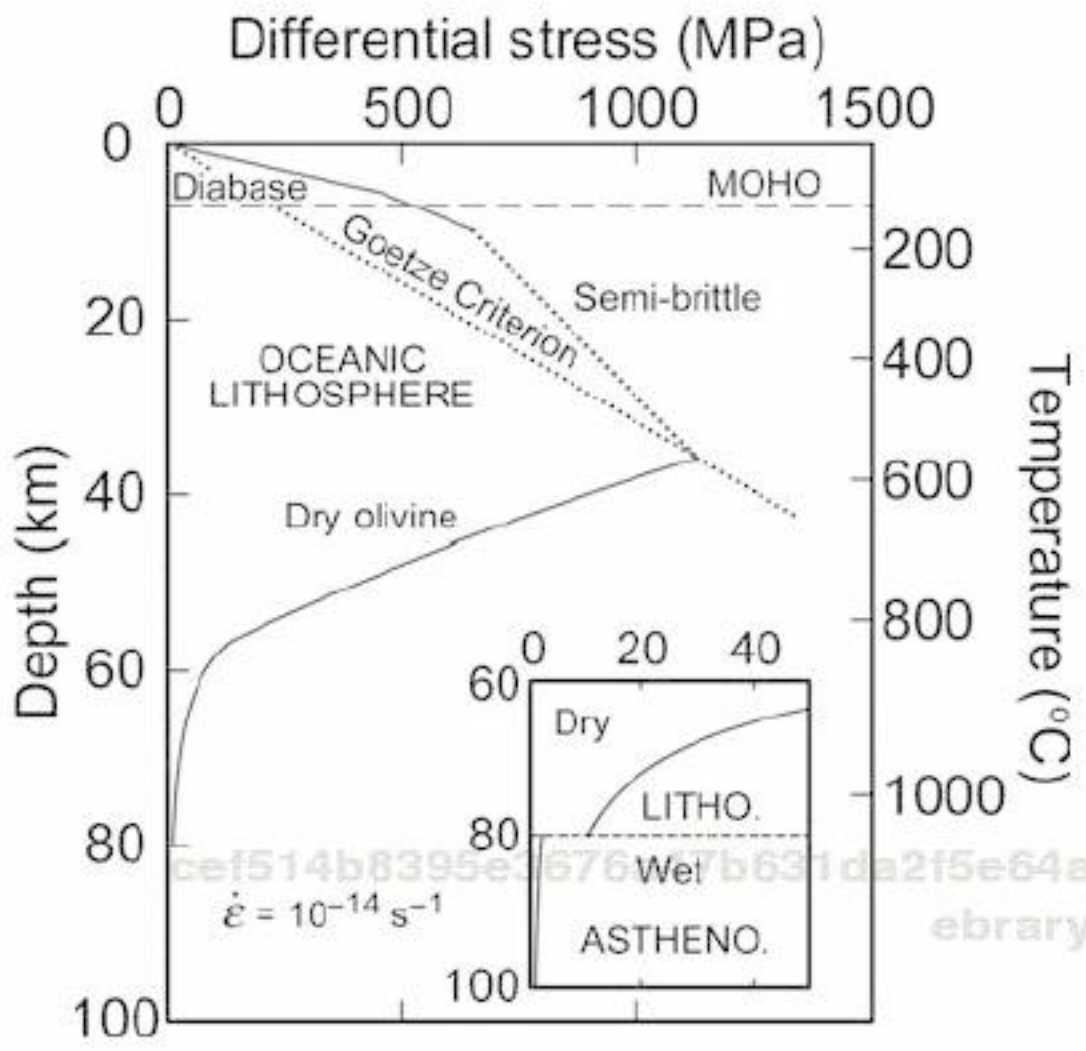

Figure 9.5. Strength envelope plotting rock strength as a function of depth in the Earth for typical oceanic lithosphere deforming at a strain rate of $10^{-14}\ s^{-1}$. An oceanic geotherm from Turcotte and Schubert (1982) for 60 m.y. lithosphere is assumed. The basaltic composition crust of 6 km thickness deforms by frictional sliding, modeled using Byerlee's law. The crust overlies a dry mantle lithosphere, which extends to 80 km depth and is modeled using rheological properties for dry olivine. The zone between approximately 10 and 38 km (the dotted line) is characterized by semi-brittle behavior. Below 80 km, a wet olivine rheology is used to model the asthenosphere, following Hirth and Kohlstedt (1996). The inset shows the contrast in strength between stiff dry lithosphere and convecting wet asthenosphere.

what appear to be shear zones in the uppermost oceanic mantle (e.g., Reston, 1990; Flack and Klemperer, 1990; Ranero *et al.*, 2003). According to the model of Hirth and Kohlstedt (1996) for formation of new oceanic crust at mid-ocean ridges, partial melting of convecting mantle below the ridge results in depletion of the water content of the nominally anhydrous mineral grains due to the strong partitioning of water into the melt phase (see also Karato, 1986; Morgan, 1997). This partitioning results in an olivine-dominated, dry residuum. Thus, the oceanic lithosphere is composed of a mostly dry basaltic crust overlying a dry peridotitic upper mantle, which can be modeled approximately by the rheological properties of dry olivine since olivine is the most abundant and the weakest mineral (Zimmerman and Kohlstedt, 2004). The underlying asthenosphere is part of the convective upper mantle and can be described by the rheological properties of wet olivine. Timescales for diffusion of water from the asthenosphere into the dry lithosphere are slow relative to the rate of plate motion (Hirth and Kohlstedt, 1996).

We constructed a strength envelope diagram in Figure 9.5 for deformation of the oceanic lithosphere under the assumptions of constant rate of deformation across the lithospheric column and no localization in the plastic deformation regime. We used the oceanic geotherm for 60-m.y. old lithosphere from Turcotte and Schubert (1982, pp. 163–167). The brittle upper lithosphere, incorporating mostly the crust, was modeled using a frictional sliding law (Byerlee, 1978) with hydrostatic pore pressure. A substantial semi-brittle regime is bounded above by the criterion that some plastic accommodation process will become activated when the stress required for frictional sliding reaches ~1/5 of the plastic flow stress for the rock. The deeper bound on the semi-brittle regime is defined by the Goetze criterion (Equation 9.11), which states that brittle processes will contribute to bulk

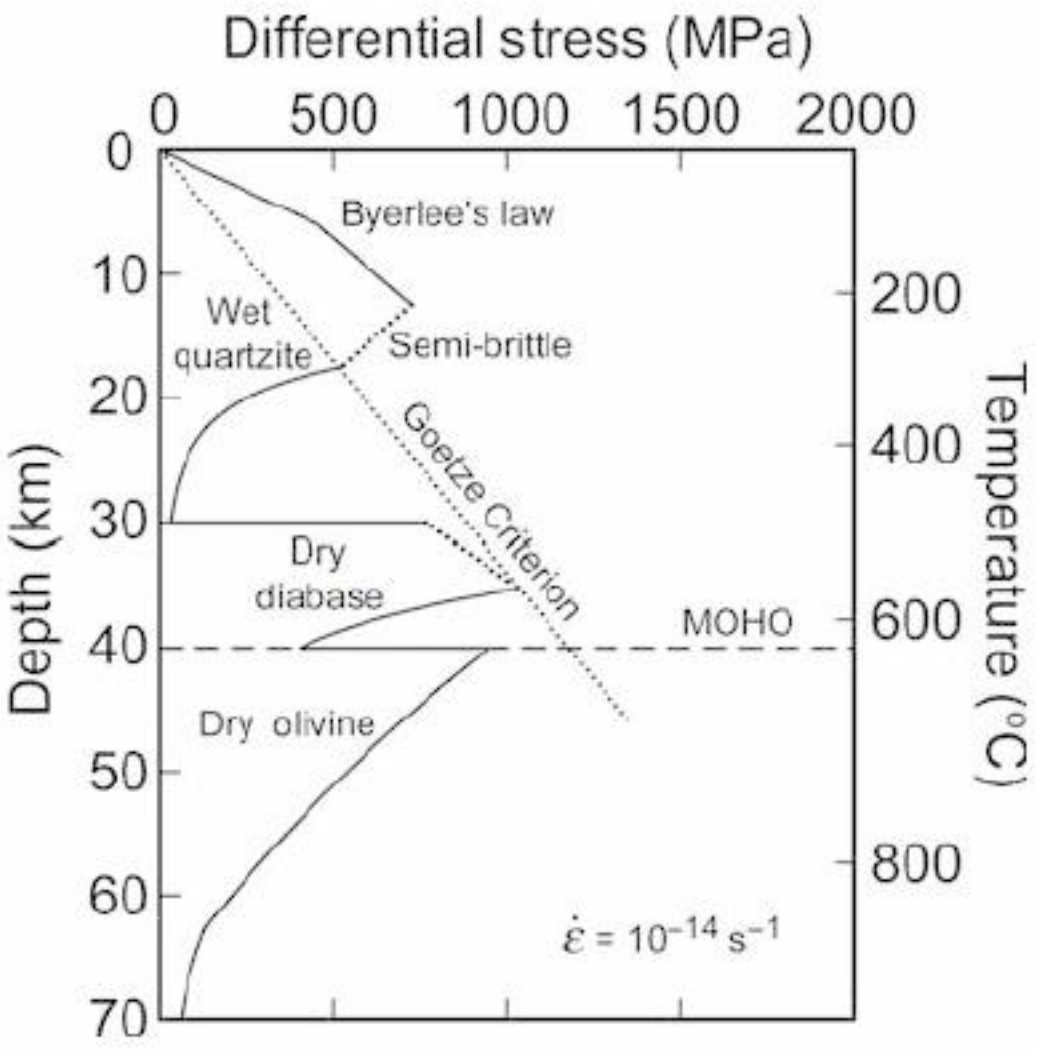

Figure 9.6. Strength envelope plot showing rock strength as a function of depth in the Earth for a model continental lithosphere deforming at a strain rate of 10^{-14} s^{-1}. A continental geotherm from Chapman (1986) for a surface heat flow of 60 mW/m was assumed. An upper crust of wet quartzite deforms at shallow depths by frictional sliding, and greater depths by dislocation creep. A dry lower crust (at amphibolite–granulite metamorphic conditions) composed of gabbroic composition rocks is modeled using rheological properties for dry diabase. Deformation in the olivine-rich mantle lithosphere is modeled by dislocation glide of dry olivine to about 60 km depth and by dislocation creep of dry olivine at greater depths. Semi-brittle regions exist in both the upper crust and lower crust; these regions are bounded below by the Goetze criterion.

deformation as long as the differential stress is greater than the overburden pressure. The actual rock strength between these bounds is not well constrained by laboratory experiments or field observations.

The plastic upper lithospheric mantle was modeled using a low-temperature deformation (dislocation glide) model for olivine (Goetze, 1978; Evans and Goetze, 1979) at temperatures $\leq$800 °C and a high-temperature dry dunite (dislocation, power law) flow law (Chopra and Paterson, 1984) at higher temperatures. An activation volume of 15×10^{-6} m^3/mol was used for deformation in both regimes. In the inset in Figure 9.5, a marked decrease in strength occurs in the transition from the dry, more rigid lithosphere to the wet, convecting asthenosphere, as noted by Hirth and Kohlstedt (1996).

2.1.6 Strength envelope for continental lithosphere

In a simplified lithology for Earth's continental lithosphere, an upper crust composed of wet quartzite overlies a dry lower crust (assuming granulite facies metamorphism) of gabbroic rocks, which overlies a wet or dry uppermost mantle composed mostly of olivine-rich rock (dunite). In cratonic settings, the lithospheric upper mantle is likely to be dry, consistent with the long residence time for cratonic keels over the history of Earth. Near active margins, a wet olivine rheology may be more appropriate.

Following this simplified lithology and assuming constant strain rate throughout the lithospheric column, as well as no localization in the plastic regime, we used a continental geotherm for a surface heat flow of 60 mW/m (Chapman, 1986) to plot a strength envelope for the continental lithosphere in Figure 9.6. In this figure, the uppermost brittle crust is described by a frictional sliding law (Byerlee, 1978) with

pore fluid pressure equal to the hydrostatic pressure. The fully plastic portion of the upper crust is modeled by deformation of wet quartzite (Gleason and Tullis, 1995). The plastic lower crust is modeled by creep of dry diabase (Mackwell *et al.*, 1995, 1998); the lower continental crust is generally believed to be comparatively dry due to amphibolite–granulite facies metamorphic conditions. For the uppermost mantle lithosphere, we use the low-temperature, dislocation glide model for deformation of olivine (Goetze, 1978; Evans and Goetze, 1979) and the high-temperature, dry dislocation flow law for dunite (Chopra and Paterson, 1984). Again, we assumed a value for the activation volume of 15×10^{-6} m^3/mol for plastic deformation of olivine. Semi-brittle behavior is observed at mid- and lower-crustal conditions, as indicated by the dotted lines in Figure 9.6.

2.1.7 Localization

Even within the fully plastic regime, deformation may become localized with the development of shear zones, as is commonly observed even at depths greater than 10–15 km (Ramsey, 1980). Montési and Zuber (2002) and Montési and Hirth (2003) have analyzed such localization in terms of a feedback loop involving grain size reduction that results in strain weakening. Their basic argument is that dynamic recrystallization reduces the grain size, causing a rock to weaken by enhancing the contributions of grain size sensitive creep mechanisms (i.e., diffusion creep and/or dislocation – grain boundary sliding creep) as well as by reducing the dislocation density within the grains. A key element of their analyses is the evolution of grain size, which is controlled by a competition between grain size reduction due to dynamic recrystallization and grain size increase due to grain growth. This trade-off between grain growth and dynamic recrystallization provides a natural regulator for stress buildup in the lithosphere; as stress increases, grain size in the deforming (shear) zone decreases, allowing easier deformation through dislocation – grain boundary sliding and/or diffusion creep processes and, thus, causing the stress to drop. Such a feedback system tends to stabilize preexisting plastic shear zones.

Support for this mechanism for localization can be drawn from experimental deformation results on clinopyroxene aggregates and olivine aggregates, both of which exhibit a decrease in strength (at a given strain rate and temperature) with decreasing grain size, well within the dislocation creep regime (Bystricky *et al.*, 2000; Bystricky and Mackwell, 2001; Hirth and Kohlstedt, 2003). These observations are consistent with deformation by a dislocation – grain boundary sliding process. For olivine under laboratory conditions, sample strength has been observed to decrease by a factor of about three in going from the dislocation creep regime to the dislocation – grain boundary sliding regime. Although localization will result in higher strain rates in the zone of deformation relative to pervasive flow, the reduced

strength of the material in the shear zone should more than offset these higher rates of deformation, stabilizing or enhancing localization. Shear displacements along plastic shear zones may also promote increased localization due to shear heating in regions of greatest strain rate. In addition, the presence of a fluid phase can lead to strain localization as discussed in our section on Io (Hier-Majumder and Kohlstedt, 2006; Kohlstedt and Holtzman, 2009).

2.1.8 Lithospheric deformation: the global picture

Taking all of the various aspects of deformation in Earth's lithosphere into consideration, we develop cartoons to represent a variety of plate tectonic scenarios likely to exist on Earth, as illustrated in Plate 26. In the first illustration, oceanic lithosphere (albeit shown with exaggerated crustal thickness) with a relatively dry upper crust overlies a dry, strong lower crust; uppermost mantle deforming by dislocation glide overlies a region that flows by power-law dislocation creep. The model in the second illustration is similar but with a wet lower crust, as might be found in the back-arc setting, where hydrous fluids can permeate into the lower crust from dewatering of the underlying slab. The model for a dry continental craton in the third illustration has a dry, strong crust overlying a dry, strong upper mantle, which may also be distinct mineralogically from the underlying wet convecting mantle (asthenosphere). While only illustrations, the sketches lay out the distribution and nature of strain that is possible in various geologic settings on Earth. Localization of deformation occurs not only in the brittle field but also in the semi-brittle regime and even in the plastic deformation regime of the lower crust and uppermost mantle.

2.2 Application to Venus

2.2.1 The role of water

On Earth, the rheological properties of the lithosphere are strongly influenced by even trace amounts of water dissolved in nominally anhydrous silicate minerals. This effect, often termed "water weakening" or "hydrolytic weakening," is developed in more detail in the section on Mars. In contrast to Earth, the lithosphere on Venus is expected to be thoroughly dehydrated due to high surface temperatures and extensive volcanic degassing, which are likely to have also gradually dehydrated the Venusian interior (Kaula, 1990). While the process of crustal formation probably generated a largely dry crust, subsequent plutonic activity may have resulted in episodic flushing of fluids along fault zones and associated production of hydrous minerals. Although sustained pore fluid pressure along faults seems unlikely, the presence of hydrous minerals may promote some localized weakness within the fault zone.

The comparative dryness of the Venusian lithosphere will affect the rheological behavior throughout; in the shallow crust, the pore pressure will be zero, so that

Equations (9.10a) and (9.10b) can be simplified to

$$\sigma_1 - \sigma_3 = 3.9\sigma_3 \qquad \sigma_3 < 100\,\mathrm{MP}a \tag{9.12a}$$

$$\sigma_1 - \sigma_3 = 2.1\sigma_3 + 210 \qquad \sigma_3 > 100\,\mathrm{MPa}, \tag{9.12b}$$

increasing the stress required for sliding on faults relative to the water-present situation. At greater depths, the absence of fluid and consequent lack of pressure-solution deformation processes will also strengthen the semi-brittle regime. The effective absence of water associated with faults may not only strengthen them but also inhibit their formation, as noted by Regenauer-Lieb *et al.* (2001) and Regenauer-Lieb and Kohl (2003).

At temperatures sufficiently high for fully plastic processes to occur, deformation of the crustal and mantle components of the lithosphere is likely to occur by dislocation creep or dislocation – grain boundary sliding processes. Constraints on crustal rheology come from the experimental work of Mackwell *et al.* (1995, 1998) on rocks of basaltic composition. These experiments were performed under dry conditions on samples of natural diabase extracted from basaltic dikes in Maryland and South Carolina, USA. The samples contain mostly plagioclase feldspar and pyroxene (augite and hypersthene), with minor oxide and hydrous minerals; prior to deformation, the samples were heat treated at high temperature to remove hydrous components. The measured strengths for the diabase are intermediate between those for plagioclase (Shelton and Tullis, 1981; Rybacki and Dresen, 2000; Dimanov *et al.*, 2003) and pyroxene (Bystricky and Mackwell, 2001), with most deformation accommodated by dislocation creep within the plagioclase feldspar grains. The more plagioclase-rich Columbia diabase is distinctly weaker than the more pyroxene-rich Maryland diabase under otherwise identical deformation conditions. In addition, dry diabase is not much lower in strength than olivine-rich rocks deformed under dry conditions (e.g., Chopra and Paterson, 1984; Karato *et al.*, 1986; Mei and Kohlstedt, 2000b).

As noted above, the formation of basaltic crust on Venus over time, with the resultant dehydration of the olivine-rich residuum, combined with the lack of an effective path for returning water into the Venusian interior, has probably resulted in a depletion of water in the interior of this planet. Such a loss of volatiles from the interior would likely be even more severe if a cyclic pattern of planetary resurfacing occurred, as envisioned by Turcotte (1993, 1995). A dehydrated mantle will be characterized by a significantly higher viscosity than on Earth due to the absence of water weakening of the major minerals under conditions that are otherwise similar. For example, at uppermost mantle conditions on Earth, the viscosity decrease due to water pressure equal to lithostatic pressure would be equivalent to a reduction in temperature of ~100 K (about a factor of ten in viscosity). Thus, in order for a mostly dehydrated Venus to dissipate internal heat, especially given the high surface temperature, it is likely that the interior of Venus is hotter than the interior

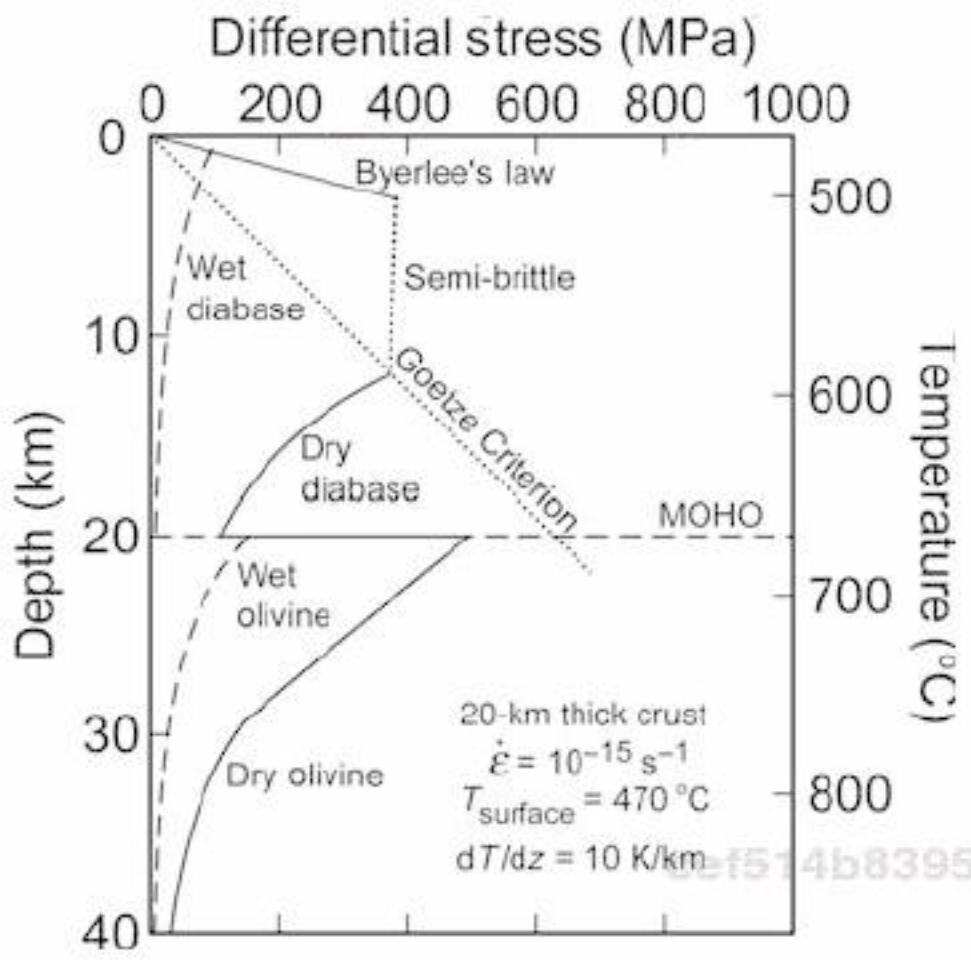

Figure 9.7. Strength envelope plotting rock strength as a function of depth in Venus for a lithosphere deforming at a strain rate of $10^{-15}\ s^{-1}$. We assumed a surface temperature of 470 °C, a thermal gradient of 10 K/km, and a crustal thickness of 20 km, conditions believed to be appropriate for Venus. A dry crust of basaltic composition was modeled at shallow depths by a frictional sliding law (Byerlee's law) and at greater depths by rheological properties for dry diabase deforming by dislocation creep. A significant region of semi-brittle behavior controls deformation over much of the crust. Rheology properties for wet diabase, included for comparison, predict an unrealistically weak crust for Venus. The mantle lithosphere, which is presumed to be strongly depleted in water, is modeled using rheological properties for dislocation glide (to about 30 km depth) and dislocation creep (at greater depths) for olivine under dry conditions. Due to long-term water loss from the mantle, no wet asthenosphere is expected on Venus.

of Earth. Solomatov and Moresi (2000) have used convection theory to argue that the mantle of Venus should be ~200 K hotter than the mantle of Earth, a difference in temperature that is more than sufficient to compensate for the lack of water weakening in the interior. Nonetheless, the model for a dry, stiff lithosphere on Earth overlying a wet asthenosphere (Hirth and Kohlstedt, 1996) does not translate to Venus, where the lack of water means that an anomalously weak asthenospheric layer is absent. As a result, while the lithospheric plates on the surface of Earth move largely independently of the convecting mantle, lithospheric deformation and mantle convection on Venus will be strongly mechanically coupled. The prediction of strong coupling is consistent with that previously deduced by Herrick and Phillips (1992) and Bindschadler *et al.* (1992) from Magellan observations of tectonic structures on Venus.

2.2.2 *Strength envelopes for Venus*

The strength envelope in Figure 9.7 is plotted for conditions believed to be appropriate for the lithosphere of Venus, with a crustal thickness of 20 km, a strain

rate of 10^{-15} s^{-1}, a surface temperature of 470 °C, and a geothermal gradient of 10 K/km. It is noteworthy that previous creep tests on diabase samples from the same or similar localities (Caristan, 1982; Shelton and Tullis, 1981) were significantly affected by small amounts of water present in the samples in the form of hydrous minerals that likely formed during near-surface weathering. As is evident in Figure 9.7, dried samples of diabase (Mackwell *et al.*, 1995, 1998) yield viscosities that are much larger than those predicted from the previous work and are more consistent with the observations of long-term passive maintenance of topography on Venus.

Several general inferences can be made on the basis of strength envelopes for Venus, such as the one in Figure 9.7. Much of the strength of the lithosphere resides in the crust, due to the high strength of basaltic-composition rocks under dry conditions. Passive maintenance of topography may thus be possible for at least tens of millions of years. The strength contrast between crust and mantle is quite modest, so that no lower crustal weak zone (the jelly sandwich model) is predicted based on experimental work on dry systems. Thus, surface tectonics will likely be coupled to strain throughout the lithosphere. Unlike the case for Earth, a wet, weak asthenosphere is absent so that convection and lithospheric deformation will be strongly coupled. In addition, regional and planetary-scale tectonics will likely directly reflect underlying mantle processes such as convection.

It must, however, be noted that the choice of parameters in Figure 9.7 is only poorly constrained by observation, with significant uncertainty in crustal thickness, strain rate, and geothermal gradient. To assess in general terms the effects of variations in crustal thickness, strain rate, and geothermal gradient, we can contrast the strength envelopes in Figure 9.8 with that in Figure 9.7. Such strength envelopes, which are based on experimentally determined rheological properties, lead to several general observations. (1) By comparing Figure 9.8a with Figure 9.7, the main effect of increasing crustal thickness (from 20 km to 30 km) is that more of the lithospheric strength resides in the crustal region; otherwise, the general conclusions based on Figure 9.7 still hold. (2) As demonstrated in Figure 9.8b, an increase in strain rate results in a much stronger lithosphere but otherwise has no effect on the conclusions drawn from Figure 9.7, as the relationship between strain rate and stress in the plastic regime is very similar for olivine and diabase. (3) As manifested in Figure 9.8c, a decrease in thermal gradient in the lithosphere markedly increases the strength of the lithosphere but otherwise does not affect the overall conclusions, as the activation energies for deformation of olivine and diabase are not so dissimilar. It should also be noted that, while a single thermal gradient throughout the lithosphere is clearly an oversimplification, alternative models lack any stronger basis in observation. In fact, one of the strongest constraints on the thermal gradient comes from modeling the thermal profile on the

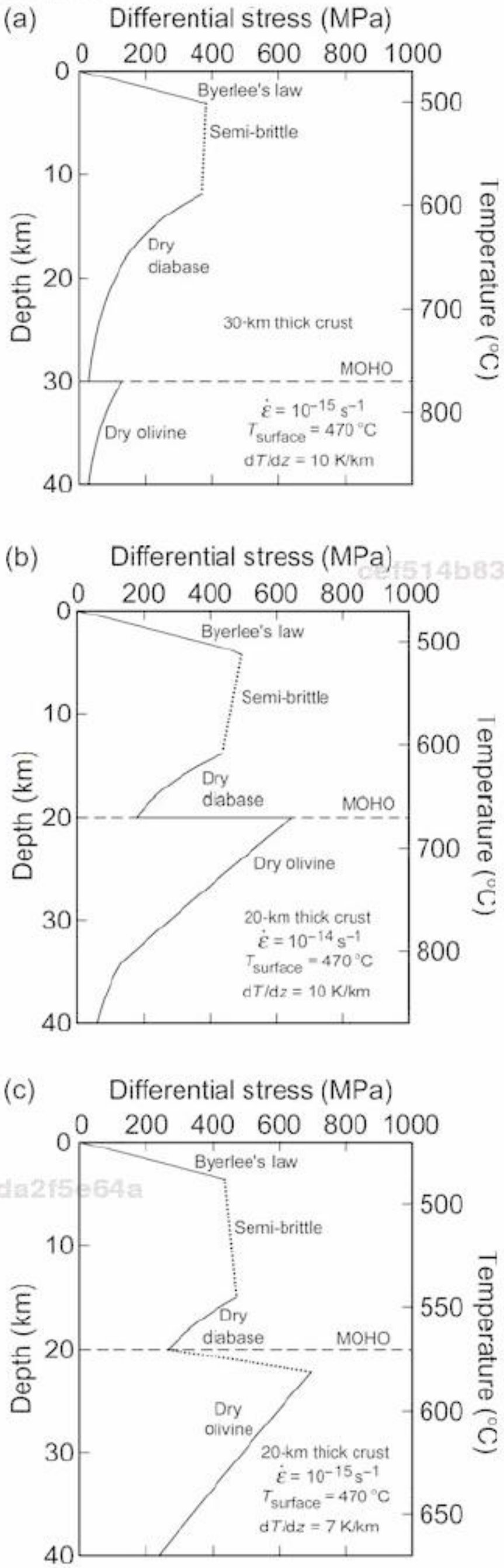

Figure 9.8. Strength envelope plotting rock strength as a function of depth in Venus to illustrate the effects of variation in (a) crustal thickness, (b) strain rate, and (c) thermal gradient by comparison to the boundary conditions used in Figure 9.7. Increasing crustal thickness resulted in a somewhat weaker lithosphere overall, while both increased strain rate and decreased thermal gradient strengthened the lithosphere. However, despite these changes in overall strength, all models still predict a strong lithosphere and strong mechanical coupling between crustal and mantle regions.

basis of observation combined with experimental measurements of deformation behavior (Phillips *et al.*, 1997).

Overall, the strength envelopes for Venus based on experimental deformation of dry diabase and olivine are consistent with our current knowledge of the history of this planet, in contrast to models based on rheological properties for undried rocks. These strength envelopes provide the basis for arguments in favor of stagnant lid dynamics for Venus and Mars, and they give substance to the conclusion that recycling of water into terrestrial planetary interiors is necessary for the maintenance of plate tectonics. Without such a return path for water, planetary interiors gradually dehydrate, making convective processes more difficult and potentially necessitating an increase in internal temperature to maintain effective dissipation of internal heat. Removal of volatiles from the interior of a terrestrial planet may also result in the loss of an anomalously weak asthenospheric layer and the promotion of a stronger coupling between the convecting mantle and the relatively rigid lithosphere.

3 Water weakening: Mars

Early in the planet's history, the lithosphere of Mars may have been significantly weaker than the lithosphere of Earth. The primary difference in rheological behavior is related to the difference in Fe content of mantle rocks, with the Martian mantle being about twice as rich in Fe as Earth's mantle (Rubie *et al.*, 2004). Iron influences the strength of rocks in two ways. Based on experience with olivine, strength decreases with increasing Fe content (e.g., Ricoult and Kohlstedt, 1985; Bai *et al.*, 1991). In addition, water solubility and hence water weakening are more pronounced in Fe-rich samples than in Fe-poor rocks (Zhao *et al.*, 2004).

To develop the theoretical framework necessary to understand one of the mechanisms by which water can weaken silicate minerals and rocks, we return to the description of diffusion-controlled dislocation creep and examine the diffusion coefficient in more detail. One of the often-cited models is that of Weertman (1968), in which dislocation sources emit dislocations that glide on parallel planes. The edge portions of the dislocations glide until two on nearby planes trap one another. To allow other dislocations emitted by the same sources to continue to glide, the edge dislocations climb toward each other and annihilate. Hence, a great deal of the strain is accomplished by glide, but the strain rate is controlled by climb. The resulting strain rate is proportional to the rate of diffusion, as described by Equations (9.6) and (9.7).

To discuss the effect of water on the rheological properties of olivine, we start with a description of its role in relaxing the von Mises (1928) criterion of homogeneous deformation requiring five independent slip systems. Next we examine

the dependence of strain rate (viscosity) on water concentration and then introduce a mechanism by which water might weaken nominally anhydrous minerals. Finally, we explore the possible implication of water on the viscosity of the Martian mantle.

3.1 Deformation under hydrous conditions

3.1.1 The von Mises criterion and the role of water

For the orthorhombic mineral olivine at high temperature and low stress, the easiest slip systems are (010)[100] and (001)[100], both involving dislocations with the shortest Burgers vector, [100]. The notation (010)[100] indicates that the slip plane is (010) and the slip direction [100]. Activation of the (010)[001] system requires stresses roughly a factor of three greater than for the systems with [100] Burgers vectors (Bai *et al.*, 1991). While the (100)[001] system has been activated in experiments investigating the (001)[100] slip system, it has not been possible to quantify its behavior, other than to note that slip systems involving dislocations with [001] Burgers vectors are more difficult to activate than the slip systems involving dislocations with [100] Burgers vectors (Durham *et al.*, 1985). However, by analogy to slip with the [100] Burgers vector, it is likely that (100)[001] may be comparable to or slightly stronger than (010)[001]. Under anhydrous deformation conditions, the strength of coarse-grained dunite lies near that of the strongest slip system, (010)[001], as illustrated in Figure 9.9, indicating that at least some activation of this slip system is required to deform the aggregate. In this case, three independent slip systems are activated of the five required by the von Mises criterion for homogeneous deformation of an aggregate; the von Mises criterion is relaxed because deformation is not rigorously homogeneous and some strain is undoubtedly taken up by diffusion. In contrast, the strength of fine-grained dunite lies near that for the weakest slip system, (010)[100]. In addition, the strain rate is grain size dependent, suggestive of a significant role of grain boundary sliding while still well within the dislocation creep regime, as described by Equation (9.8) (Wang, 2002; Hirth and Kohlstedt, 2003).

A clear role for water in de-emphasizing the limitations imposed by the von Mises criterion can be shown for olivine-rich rocks. At experimental conditions with $f_{H_2O} \approx 300$ MPa, water decreases the strength of olivine single crystals oriented to favor slip on each of the slip systems by a factor of ~2, as demonstrated by comparing results plotted in Figure 9.9 for anhydrous conditions with those plotted in Figure 9.10 for hydrous conditions (Mackwell *et al.*, 1985). This weakening effect is correlated with an increase in dislocation climb, likely reflecting enhanced diffusion rates for silicon in olivine under wet conditions (Mackwell *et al.*, 1985; Costa and Chakraborty, 2008). At the same time, the strength of coarse-grained

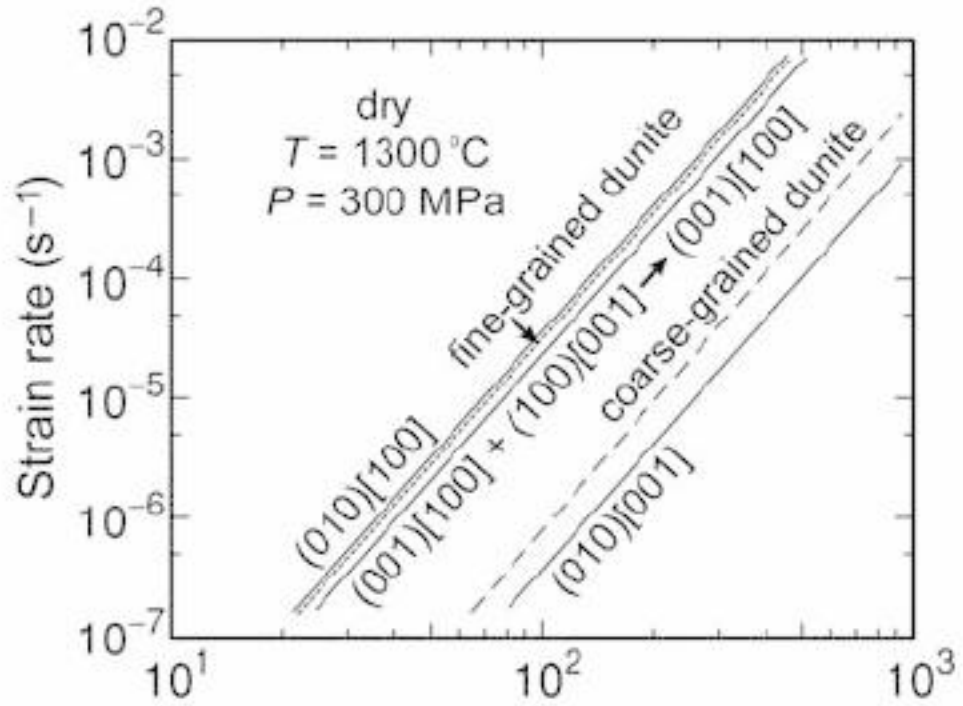

Figure 9.9. Log–log plot of strain rate as a function of differential stress for olivine single crystals (solid lines), as well as fine-grained (short-dash line) and coarse-grained (long-dash line) dunite deformed under anhydrous conditions. The olivine single crystals are oriented to maximize the resolved shear stress and thus slip on the (010)[100], (001)[100] plus (100)[001], and (010)[001] slip systems. Deformation of crystals oriented to activate the (001)[100] slip system plus the (100)[001] slip system is dominated by the former. Note the proximity of the fine-grained dunite flow behavior to that of the weak slip system (010)[100] and the proximity of the coarse-grained dunite flow behavior to that of the hardest slip system, (010)[001].

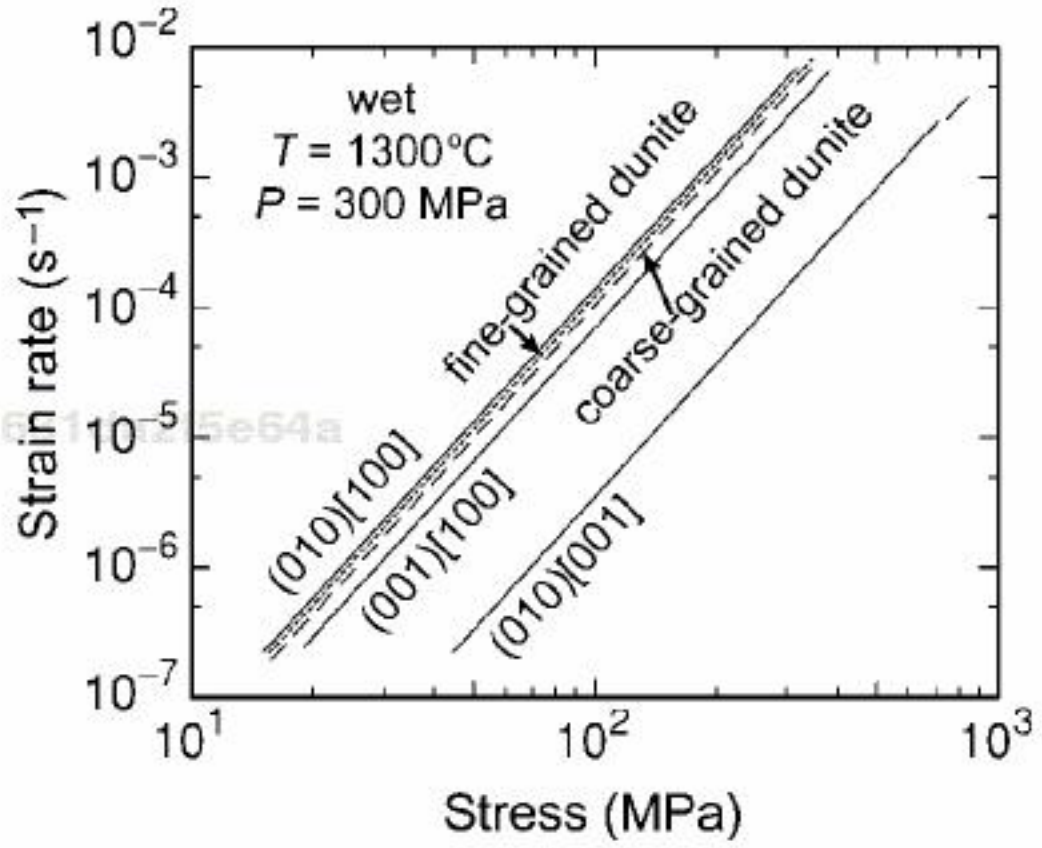

Figure 9.10. Log–log plot of strain rate as a function of differential stress for olivine single crystals (solid lines), as well as fine-grained (short-dash line) and coarse-grained (long-dash line) dunite deformed under hydrous conditions. The olivine single crystals are oriented to maximize the resolved shear stress and thus slip on the (010)[100], (001)[100] plus (100)[001], and (010)[001] slip systems. Deformation of crystals oriented to activate the (001)[100] slip system plus the (100)[001] slip system is dominated by the former. Note the proximity of both the fine-grained and the coarse-grained dunite flow behavior to that of the weakest slip system, (010)[100].

dunite exhibits a factor of >4 weakening effect (Chopra and Paterson, 1984), falling near the strength of the easiest slip systems, (010)[100] and (001)[100]; under hydrous conditions, the strengths of coarse-grained and fine-grained dunite are similar, as illustrated in Figure 9.10. Thus, in the presence of water, the need for slip on the (010)[001] slip system is decreased and only two independent slip systems appear to be required for plastic deformation of the aggregate. The reduction in the number of independent slip systems required by the von Mises criterion from five to two probably reflects the increased rates of grain matrix diffusion and, hence, of dislocation climb (Mackwell *et al.*, 1985) as well as relaxation of the constraint of homogeneous deformation throughout the sample.

3.1.2 Comparison of deformation under anhydrous and hydrous conditions

Deformation experiments on polycrystalline samples of olivine demonstrate that strain rate increases approximately linearly with increasing water fugacity (Mei and Kohlstedt, 2000a,b). The flow law under hydrous conditions can then be expressed as a modified form of Equation (9.6) as

$$\dot{\varepsilon} = \mathrm{A} f_{\mathrm{H_2O}}^{r} \frac{\sigma^n}{d^p} \exp\left(-\frac{E + PV}{\mathrm{R}T}\right), \tag{9.13a}$$

or in terms of viscosity as

$$\eta = \frac{1}{\mathrm{A}} \frac{d^p}{f_{\mathrm{H_2O}}^{r} \sigma^{n-1}} \exp\left(\frac{E + PV}{\mathrm{R}T}\right). \tag{9.13b}$$

In the diffusion creep regime, $r \approx 1$ (Mei and Kohlstedt, 2000a), while in the dislocation creep regime, $r \approx 1$ to 1.2 (Mei and Kohlstedt, 2000b; Karato and Jung, 2003). The stress exponent $n = 1$ and grain size exponent $p = 3$ in the diffusion creep regime, while $n = 3.5$ and $p = 0$ in the dislocation creep regime (Hirth and Kohlstedt, 2003). The viscosity of dunite as a function of pressure under hydrous conditions is compared to that for dunite under anhydrous conditions in Figure 9.11, using the flow parameters reported by Karato and Jung (2003). The viscosity of samples deformed under anhydrous conditions increases with increasing pressure due to the explicit pressure dependence in Equation (9.6). In contrast, the viscosity of samples deformed under hydrous conditions initially decreases rapidly and then more gradually with increasing pressure due to competition between the implicit effect of water fugacity, which increases with increasing pressure under water-saturated conditions (Pitzer and Sterner, 1994), and the explicit effect of pressure in Equation (9.13b). If this plot were extended beyond a pressure of ~3 GPa for the samples deformed under water-saturated conditions, the strain rate would begin to increase with increasing pressure; this region has yet to be investigated experimentally.

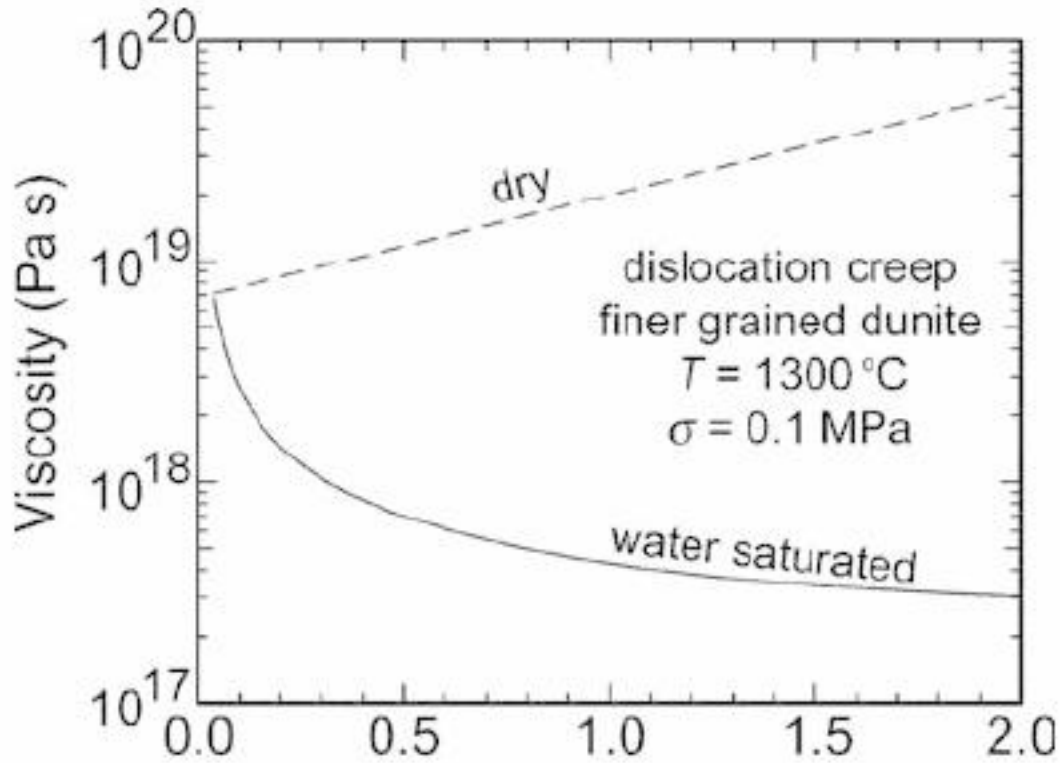

Figure 9.11. Semi-log plot of viscosity versus pressure for dunite in the dislocation creep regime. Under anhydrous (dry) conditions, viscosity increases with increasing pressure based on an exponential dependence of strain rate on pressure, Equation (9.6). Under hydrous (wet) conditions, viscosity decreases with increasing pressure due to the approximately linear dependence of strain rate on water fugacity, Equation (9.13b), since water fugacity increases with increasing pressure under water-saturated conditions (e.g., Pitzer and Sterner, 1994). This implicit effect of water fugacity on viscosity with increasing pressure is offset to some degree by the explicit exponential increase in viscosity with increasing pressure in Equation (9.13b).

3.1.3 The importance of point defects in ionic diffusion and diffusion-controlled creep

The key issue in discussing the effect of water on diffusion in nominally anhydrous minerals is the mechanism by which protons, introduced into grains in the presence of water, affect the diffusion coefficients for the constituent ions. Ionic diffusivities are determined by the concentration and diffusivity (i.e., mobility) of the point defects (vacancies and interstitials) involved in the diffusion process. As the most completely studied mineral in this regard is olivine, $(Mg_{1-x}Fe_x)_2SiO_4$, we will focus on it. If diffusion of a specific ion, for example Si, occurs dominantly by a vacancy mechanism, then the ionic self-diffusivity is given by

$$D_{\mathrm{Si}} = X_{\mathrm{V_{Si}}} D_{\mathrm{V_{Si}}}, \tag{9.14}$$

where D_{Si} is the diffusion coefficient for Si, $X_{\mathrm{V_{Si}}}$ is the concentration of silicon vacancies, and $D_{\mathrm{V_{Si}}}$ is the diffusion coefficient of silicon vacancies. Since the concentration of silicon vacancies is very small ($\sim 10^{-12}$ to $\sim 10^{-6}$), it is clear that $D_{\mathrm{Si}} \ll D_{\mathrm{V_{Si}}}$. For minerals composed of several ions, self-diffusivities for each of the ions will have the form given by Equation (9.14).

In minerals composed of more than one ion, the strain rate described by Equation (9.4) for diffusion creep or Equation (9.7) for dislocation creep is determined

by the slowest diffusing species traveling along its fastest path, either through grain matrices (interiors) or along grain boundaries. This situation arises because the fluxes of all of the species that make up the crystalline grains are coupled in order to maintain stoichiometry (Ruoff, 1965; Poirier, 1985; Dimos *et al.*, 1988; Jaoul, 1990; Schmalzried, 1995). In the case of olivine, $D_{\mathrm{Me}} \gg D_{\mathrm{O}} > D_{\mathrm{Si}}$ (Me = octahedrally coordinated metal cations: Buening and Buseck, 1973; Misener, 1974; Hermeling and Schmalzried, 1984; Nakamura and Schmalzried, 1984; Jaoul *et al.*, 1995; Chakraborty, 1997; O: Gerard and Jaoul, 1989; Ryerson *et al.*, 1989; Si: Houlier *et al.*, 1990; Dohmen *et al.*, 2002), such that the effective diffusion coefficient, D_{eff}, that limits the rate of deformation is (Dimos *et al.*, 1988)

$$D_{\mathrm{eff}} = \frac{D_{\mathrm{O}} D_{\mathrm{Si}}}{D_{\mathrm{O}} + 4D_{\mathrm{Si}}} \approx D_{\mathrm{Si}}. \tag{9.15}$$

In Equation (9.1), the dependencies of viscosity (strain rate) on the activities and fugacities of the chemical components enter through the concentrations of point defects. In the specific case described by Equation (9.15), these point defects are vacancies and interstitials on the silicon sublattice. The defect diffusivities (mobilities) are not significantly affected by the activities or fugacities of chemical components (Dieckmann and Schmalzried, 1977a,b; Dieckmann *et al.*, 1978; Schmalzried, 1981, pp. 174–175; Shewmon, 1983, pp. 155–160; Nakamura and Schmalzried, 1984). Therefore, the question to be answered is "how does water affect the concentration of vacancies and interstitials on the silicon sublattice in olivine?"

3.1.4 Point defects in olivine under anhydrous conditions

As the basis for addressing this question, it is instructive to first consider diffusion in olivine under anhydrous conditions. Two steps are needed in order to determine the dependencies of the concentrations of point defects on component activities and fugacities. The fact that Fe is present not only as Fe^{2+} but also in small concentrations ($\sim 10^{-3}$–10^{-5}) as Fe^{3+} is critical. First, it is necessary to specify the charge neutrality condition, which for olivine is (e.g., Sockel, 1974; Greskovich and Schmalzried, 1970; Schmalzried, 1978)

$$[\mathrm{Fe}^{\bullet}_{\mathrm{Me}}] = 2[\mathrm{V}''_{\mathrm{Me}}]; \tag{9.16}$$

the point defects involved in the charge neutrality condition are referred to as the majority defects. The Kröger–Vink notation (Kröger and Vink, 1956) is introduced in discussing point defect chemistry to specify the species, site (subscript), and charge (superscript). The square brackets denote concentration relative to the formula unit or lattice molecule and will be used interchangeably with the symbol X. As an example, $X_{\mathrm{V}_{\mathrm{Me}}} \equiv [\mathrm{V}''_{\mathrm{Me}}]$. Charge is referenced to the perfect lattice, with a

dot indicating a positive charge and a slash denoting a negative charge, both relative to the neutral charge of a normally occupied site, as indicated by an $\times$. In general, the charge neutrality condition is not *a priori* known for any particular mineral and must be determined experimentally by studying properties such as thermogravimetry, ionic conductivity, electrical conductivity, and point defect relaxation kinetics.

Second, defect reactions must be written in terms of structural elements of the ideal crystal, point defects in the ideal crystal treated as quasi-particles, and chemical components of the system (Schmalzried, 1981 pp. 37–57, 1995 pp. 27–37). It is useful to explore a point defect reaction involving the majority point defects, that is, Fe^{3+} on a metal cation Me site, $Fe^{\bullet}_{Me}$, and a vacant metal cation site, V''_{Me}. Numerous point defect reactions can be written that involve these two point defects, but we focus on one that involves just these two defects:

$$\frac{1}{2}O_2(srg) + MeSiO_3(srg) + Me^{\times}_{Me} + 2Fe^{\times}_{Me} = 2Fe^{\bullet}_{Me} + V''_{Me} + Me_2SiO_4(srg), \tag{9.17}$$

where srg designates a site of repeatable growth, such as a dislocation or grain boundary. The law of mass action applied to Equation (9.17) yields

$$\frac{[Fe^{\bullet}_{Me}]^2[V''_{Me}]a_{ol}}{a_{en}[Fe^{\times}_{Me}]^2[Me^{\times}_{Me}](f_{O_2}/f^{o}_{O_2})^{1/2}} = K_{17}(T, P, X_{Fa}), \tag{9.18}$$

where Fa indicates fayalite, Fe_2SiO_4, ol indicates olivine, Me_2SiO_4, en denotes enstatite, $MeSiO_3$, and $f^{o}_{O_2}$ is the reference state oxygen fugacity. In writing Equation (9.18), it is assumed that the concentrations of the point defects are dilute so that their activities can be replaced by their concentrations. If Equations (9.16) and (9.18) are combined with $a_{ol} = 1$, since olivine is present, and $[Me^{\times}_{Me}] \approx 1$, as it differs from unity only by the concentration of vacancies on the metal cation sublattice, $\sim 10^{-4}$, then

$$[Fe^{\bullet}_{Me}] = 2[V''_{Me}] = 2^{1/3}[Fe^{\times}_{Me}]^{2/3}(f_{O_2}/f^{o}_{O_2})^{1/6}a^{1/3}_{en}K^{1/3}_{17}(T, P, X_{Fa}). \tag{9.19}$$

The dependence of the concentration of Si vacancies is now obtained by considering a reaction involving Si vacancies and one or more of the point defects already considered. For example,

$$O_2(srg) + Me_2SiO_4(srg) + Si^{\times}_{Si} + 4Fe^{\times}_{Me} = 4Fe^{\bullet}_{Me} + V''''_{Si} + 2MeSiO_3(srg). \tag{9.20}$$

The law of mass action yields

$$\begin{aligned}[V''''_{Si}] &= [Fe^{\bullet}_{Me}]^{-4}[Fe^{\times}_{Me}]^4(f_{O_2}/f^{o}_{O_2})a^{-2}_{en}K_{20}(T, P, X_{Fa}) \\ &= [Fe^{\times}_{Me}]^{4/3}(f_{O_2}/f^{o}_{O_2})^{1/3}a^{-10/3}_{en}\frac{K_{20}(T, P, X_{Fa})}{2^{4/3}K^{4/3}_{17}(T, P, X_{Fa})},\end{aligned} \tag{9.21}$$

where again the relations $a_{ol} = 1$ and $[Si_{Si}^{\times}] \approx 1$ are used; the second equality in Equation (9.21) is obtained by using the relation for $[Fe_{Me}^{\bullet}]$ from Equation (9.19). Therefore, if Si diffuses by a vacancy mechanism and as vacancy diffusivity is not significantly affected by the activities or fugacities of chemical components,

$$D_{Si} \propto [V_{Si}^{''''}] \propto [Fe_{Me}^{\times}]^{4/3} f_{O_2}^{1/3} a_{en}^{-10/3}, \tag{9.22}$$

where the oxygen fugacity and enstatite activity dependencies of diffusivity and thus of diffusion-controlled creep rate are shown explicitly (see Equation 9.1).

Tracer diffusion experiments of Si, the slowest diffusing species through grain interiors in olivine, suggest that the rate of silicon diffusion decreases with increasing oxygen fugacity; specifically, $D_{Si} \propto f_{O_2}^{-0.19}$ (Houlier *et al.*, 1990). This inverse dependence of Si diffusivity on oxygen fugacity has been interpreted as indicating that Si is diffusing by an interstitial mechanism rather than by a vacancy mechanism, since $[Si_i^{\bullet\bullet\bullet\bullet}] \propto [V_{Si}^{''''}]^{-1}$ (also see Equation 9.22). In contrast, creep experiments on olivine single crystals and olivine-rich rocks reveal that strain rate increases with increasing oxygen fugacity (Kohlstedt and Hornack, 1981; Kohlstedt and Ricoult, 1984; Jaoul, 1990; Bai *et al.*, 1991; Jin *et al.*, 1994; Keefner *et al.*, 2005), suggesting that diffusion of Si may not be limiting the rate of creep. Recent diffusion experiments carried out under anhydrous conditions, however, demonstrate two important points: first, $D_O \gg D_{Si}$, and second, the activation energy for self-diffusion of Si of ~530 kJ/mol (Dohmen *et al.*, 2002) is essentially identical to the activation energy for high-temperature creep of olivine (Chopra and Paterson, 1984; Hirth and Kohlstedt, 2003). This value of the activation energy for Si diffusion is almost a factor of two larger than the value reported previously (Houlier *et al.*, 1990) and approximately a factor of two larger than the activation energies for self-diffusion of O (Dohmen *et al.*, 2002) and Me (Chakraborty, 1997). Dohmen *et al.* (2002) note that the analysis of the Si diffusion data by Houlier *et al.* (1990) was seriously affected by very short diffusion distances, which resulted in an underestimation of the activation energy by almost a factor of two (290 versus 530 kJ/mol) and an associated large uncertainty in the dependence of Si diffusivity on oxygen fugacity. For the present example, therefore, we assert that the high-temperature rate of creep of olivine-rich rocks is controlled by Si diffusing by a vacancy mechanism, but the reader must be aware that not all alternative models can be safely rejected (for further discussion, see Kohlstedt, 2006, 2007).

3.1.5 Point defects in olivine under hydrous conditions

With the introduction of water into the surrounding environment, protons diffuse rapidly into nominally anhydrous minerals (Mackwell and Kohlstedt, 1990; Kohlstedt and Mackwell, 1998, 1999; Wang and Zhang, 1996; Hercule and Ingrin, 1999; Carpenter Woods *et al.*, 2000; Woods, 2000; Stalder and Skogby, 2002;

Blanchard and Ingrin, 2004) and influence the point defect chemistry (i.e., point defect concentrations) and thus diffusivities of all of the ionic species. Although our understanding of the point defect chemistry of olivine and other nominally anhydrous silicate minerals under hydrous conditions is far from complete, certain aspects are well constrained by experiment and theory.

Theoretical calculations by Brodholt and Refson (2000) and Braithwaite *et al.* (2003) for olivine under hydrous conditions reveal the importance of point defect associates formed between one or more hydroxyl ions, $(\mathrm{OH})^{\bullet}_{\mathrm{O}}$, and a silicon and/or a metal cation vacancy. Both conclude that the most energetically favorable mechanism for introducing protons into olivine is by the defect associate $\{\mathrm{V}''''_{\mathrm{Si}} - 4(\mathrm{OH})^{\bullet}_{\mathrm{O}}\}^{\times}$. Here, the curly brackets, {}, denote a defect associate, which is often written as $(4\mathrm{H})^{\times}_{\mathrm{Si}}$, indicating four protons in close proximity to a vacant Si site, the so-called hydrogarnet defect. While this shorthand is convenient, the physical meaning is best described as a defect associate, which avoids the implicit suggestion that protons lie physically within the vacant site. Braithwaite *et al.* (2003), however, argue that the defect associate $\{\mathrm{V}''''_{\mathrm{Si}} - 4(\mathrm{OH})^{\bullet}_{\mathrm{O}}\}^{\times}$, should yield an O–H stretching band that is, in fact, not observed in infrared spectra. Therefore, they conclude that the most common water-derived point defect involving a silicon vacancy is the defect associate $\{\mathrm{V}''''_{\mathrm{Si}} - 3(\mathrm{OH})^{\bullet}_{\mathrm{O}}\}'$, stabilized by a charge compensating defect such as $\mathrm{Fe}^{\bullet}_{\mathrm{Me}}$.

In this contribution, we explore the possible role of the defect associate $\{\mathrm{V}''''_{\mathrm{Si}} - 3(\mathrm{OH})^{\bullet}_{\mathrm{O}}\}'$ in the charge neutrality conditions. However, we emphasize the importance of $(\mathrm{OH})^{\bullet}_{\mathrm{O}}$ rather than $\mathrm{Fe}^{\bullet}_{\mathrm{Me}}$ as the stabilizing, charge-compensating defect because the concentration of $(\mathrm{OH})^{\bullet}_{\mathrm{O}}$ increases systematically with increasing water fugacity and is not limited by the total amount of Fe present in the system. As for the anhydrous case, we start by writing the charge neutrality condition:

$$[(\mathrm{OH}^{\bullet}_{\mathrm{O}})] = [\{\mathrm{V}''''_{\mathrm{Si}} - 3(\mathrm{OH})^{\bullet}_{\mathrm{O}}\}'] \equiv [(3\mathrm{H})'_{\mathrm{Si}}]. \tag{9.23}$$

The dependence of the concentrations of these two defects on water fugacity can be obtained by examining a reaction involving both of them:

$$2\mathrm{H_2O(srg)} + \mathrm{Me_2SiO_4(srg)} + \mathrm{Si}^{\times}_{\mathrm{Si}} + \mathrm{O}^{\times}_{\mathrm{O}} = (\mathrm{OH})^{\bullet}_{\mathrm{O}} + (3\mathrm{H})'_{\mathrm{Si}} + 2\mathrm{MeSiO_3(srg)}. \tag{9.24}$$

The law of mass action applied to Equation (9.24) combined with Equation (9.23) yields

$$[\{\mathrm{V}''''_{\mathrm{Si}} - 3(\mathrm{OH})^{\bullet}_{\mathrm{O}}\}'] = [(\mathrm{OH})^{\bullet}_{\mathrm{O}}] = (f_{\mathrm{H_2O}}/f^{\mathrm{o}}_{\mathrm{H_2O}})^{1} a_{\mathrm{en}}^{-1} K_{24}^{1/2}(T, K, X_{\mathrm{Fa}}), \tag{9.25}$$

where $f^{\mathrm{o}}_{\mathrm{H_2O}}$ is the reference state water fugacity. One can write similar equations for defect associates in which 1, 2 or 4 protons are associated with a silicon vacancy. However, based on the work of Braithwaite *et al.* (2003), the $(3\mathrm{H})'_{\mathrm{Si}}$ defects are the

Si defects present in greatest concentration. The total concentration of Si vacancies is then expressed as

$$\begin{aligned} X_{V_{Si}}^{total} &= [V_{Si}''''] + [\{V_{Si}'''' - (OH)_O^\bullet\}'''] + [\{V_{Si}'''' - 2(OH)_O^\bullet\}''] \\ &\quad + [\{V_{Si}'''' - 3(OH)_O^\bullet\}'] + [\{V_{Si}'''' - 4(OH)_O^\bullet\}^\times] \\ &\approx [\{V_{Si}'''' - 3(OH)_O^\bullet\}'] \\ &\propto f_{H_2O}^1. \end{aligned} \tag{9.26}$$

Since silicon vacancies and protons diffuse much more rapidly than silicon ions, defect associates such as $\{V_{Si}'''' - 3(OH)_O^\bullet\}'$ should be able to diffuse quickly and contribute directly to Si diffusion (Brodholt and Refson, 2000; Wang *et al.*, 2004; Hier-Majumder *et al.*, 2005); a silicon atom can hop into such a defect, displacing the protons, which move into the site vacated by the silicon. In this regard, it is instructive to recall that hydrogen ions in nominally anhydrous minerals can be thought of in three different but related ways. First, strictly speaking, hydrogen ions occupy interstitial sites denoted by $H_i^\bullet$. Second, hydrogen ions reside in close proximity to oxygen ions as indicated by the notation $(OH)_O^\bullet$ and detected as OH-stretching bands in infrared spectra. Third, hydrogen ions are protons, $p^\bullet$, which diffuse much faster than Me, O, and Si. In reality, hydrogen ions in a silicate lattice are all of these, as interstitial hydrogens are generally bonded into the oxygen lattice and are relatively easily mobilized as protons. From the diffusion perspective, therefore, it is useful to replace the defect associate $\{V_{Si}'''' - 3(OH)_O^\bullet\}'$ with $\{V_{Si}'''' - 3p^\bullet\}'$. Although the water fugacity dependence of Si diffusion has yet to be determined experimentally, diffusion experiments demonstrate that Si diffuses a factor of >100 times faster under hydrous conditions (1300 °C, 2 GPa) than under anhydrous conditions (1300 °C, 0.1 MPa) (Costa and Chakraborty, 2008) due effectively to an increase in the number of silicon vacancies that are stabilized due to the presence of protons. It should be noted that, even under hydrous conditions, Me diffusion is still orders of magnitude faster than Si or O diffusion (Hier-Majumder *et al.*, 2005), so that $D_{Me} > D_O \geq D_{Si}$ under both anhydrous and hydrous conditions.

In the previous studies, it was proposed that deformation of olivine under hydrous conditions is rate-limited by diffusion of Si by an interstitial mechanism (Mei and Kohlstedt, 2000a,b; Karato and Jung, 2003). However, neither study took into account defect associates such as the one described by Equations (9.25) and (9.26). Here, we emphasize the importance of defect associates formed between protons and Si vacancies, based on theoretical calculations that predict that the concentration of these defect associates increases rapidly with increasing water concentration (Brodholt and Refson, 2000; Braithwaite *et al.*, 2003). Therefore, under hydrous conditions, the approximate linear dependence of strain rate on water fugacity in Equation (9.13) is consistent with climb-controlled creep in

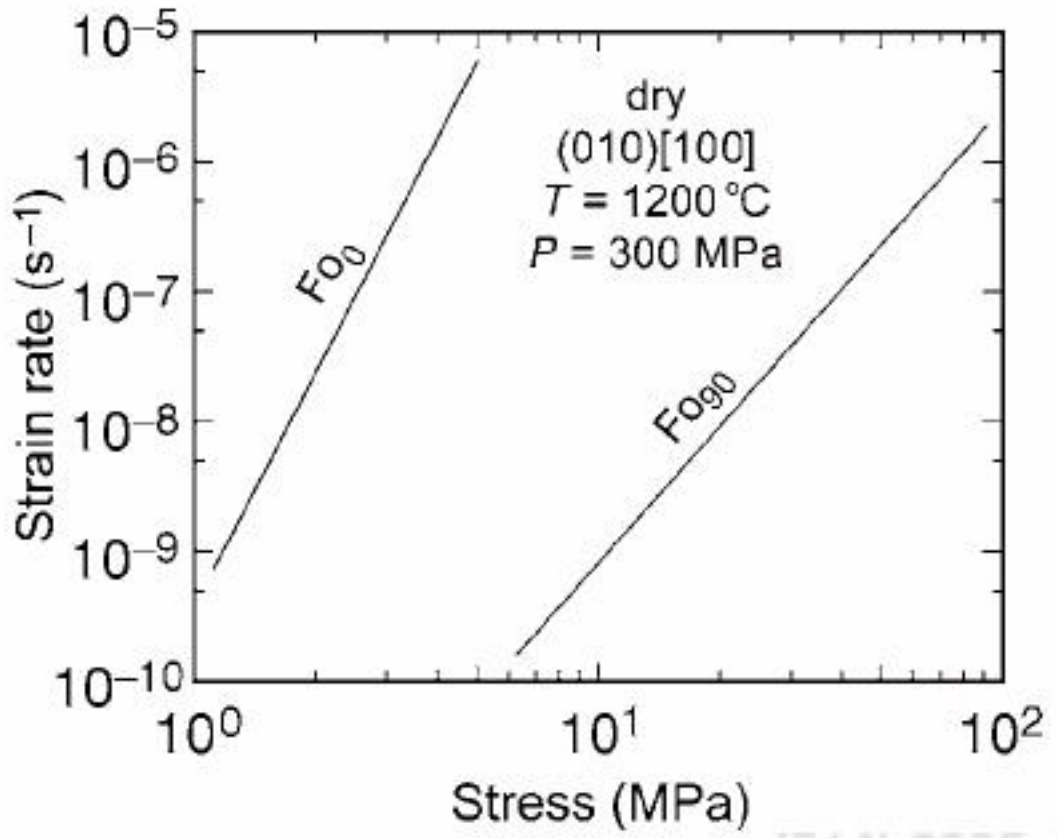

Figure 9.12. Comparison of strain rate as a function of differential stress for single crystals of Fo_0 (Ricoult and Kohlstedt, 1985) and Fo_{90} (Bai *et al.*, 1991). At a given strain rate, fayalite crystals are over an order of magnitude weaker than Fe-poor samples.

which the climb rate is governed by a vacancy mechanism, Equations (9.25) and (9.26).

3.2 Application to Mars

Analyses of mantle minerals contained within Martian meteorites indicate that the Martian interior is characterized by olivines with a higher iron content (about Fo_{80}) than on Earth (about Fo_{90}), and by mantle silicates that have water contents not so different from terrestrial examples, although there is some debate about the true mantle water budget for the interior of Mars. The viscosity of the mantle of Mars compared to that of Earth will be influenced by two factors. First, deformation experiments on single crystals of olivine demonstrate that, at a given temperature and strain rate, strength decreases with increasing Fe content (e.g., compare Ricoult and Kohlstedt, 1985 with Bai *et al.*, 1991). This point is illustrated in Figure 9.12, which compares the flow law for Fo_{90} with that for Fo_0. This general type of behavior is anticipated from the difference in solidus temperature, T_s, of these crystals with $T_s(Fo_{90}) \approx 2130$ K and $T_s(Fo_0) \approx 1478$ K combined with the difference in iron content and thus in point defect chemistry. A common scaling law, used to compare the rate of deformation of materials with the same structure but different melting points, is based on the solidus temperature through the activation energy. Specifically, the activation energy in Equation (9.6) is replaced such that $E/R = gT_s$, where the value of g depends upon the system of interest (Weertman, 1970; Weertman and Weertman, 1975). A value of $E = 540$ kJ/mol provides a good description of the temperature dependence of creep rate for single crystals of Fo_{90}

(Bai *et al.*, 1991), that is, g ≈ 30. For this value of g, the predicted difference in strain rate for Fo_{90} and Fo_0 at 1200 °C is ~6×10^5, a value in reasonable agreement with that obtained by comparison of the creep data for these compositions in Figure 9.12. If we now take this approach to predict the relative strain rates at fixed stress for a temperature of 1200 °C, we obtain a factor of 2 to 3 faster strain rate for Fo_{80} than for Fo_{90} at a given differential stress. (Note that recently published experimental results demonstrate that this difference in strain rate is roughly correct; however, a detailed examination of the data reveals that scaling based on solidus temperature alone is not sufficient to predict fully the experimental results (Zhao *et al.*, 2009).)

Second, in addition to the direct effect of Fe on viscosity, water weakening is anticipated to increase with increasing Fe content because the solubility of protons/hydrogen increases with increasing Fe concentration in olivine. Based on laboratory experiments (Zhao *et al.*, 2004), the solubility of hydrogen, C_H, can be expressed as

$$C_H \propto f^1_{H_2O} \exp\left(\frac{\beta X_{Fa}}{RT}\right), \tag{9.27}$$

with $\beta \approx 97$ kJ/mol. This dependence of proton/hydrogen solubility in olivine enters through the Gibbs free energy for incorporation of protons into olivine, a quantity that is sensitive to the Fe:Mg ratio. Given the linear dependence of hydrogen concentration on water fugacity in Equation (9.27), the strain rate in Equation (9.13a) can be written as

$$\dot{\varepsilon} \propto C_H^r \exp\left(\frac{r\beta X_{Fa}}{RT}\right). \tag{9.28}$$

At 1200 °C, the effect of increased water solubility in Fo_{80} crystals relative to that in Fo_{90} crystals results in a factor of 2.2 ($r = 1$) to 2.6 ($r = 1.2$) increase in strain rate. Therefore, in addition to the direct effect of more Fe-rich olivine being weaker than less Fe-rich olivine, the indirect effect of increased water solubility in Martian olivine introduces an additional weakening effect. Combined, we anticipate a factor of ≥5 difference between the viscosity of the Martian mantle and Earth's mantle (assuming water saturation in both bodies and similar temperature distributions), as illustrated in Figure 9.13. Of course, neither the temperature nor the water content of the Martian interior is well constrained, so that this estimate is a maximum potential contrast in viscosity for Earth versus Mars. If present-day Mars is significantly cooler than Earth, as one might argue based on its smaller size, and if the interior water content is similar to or less than in Earth, then the Martian interior might be much more viscous.

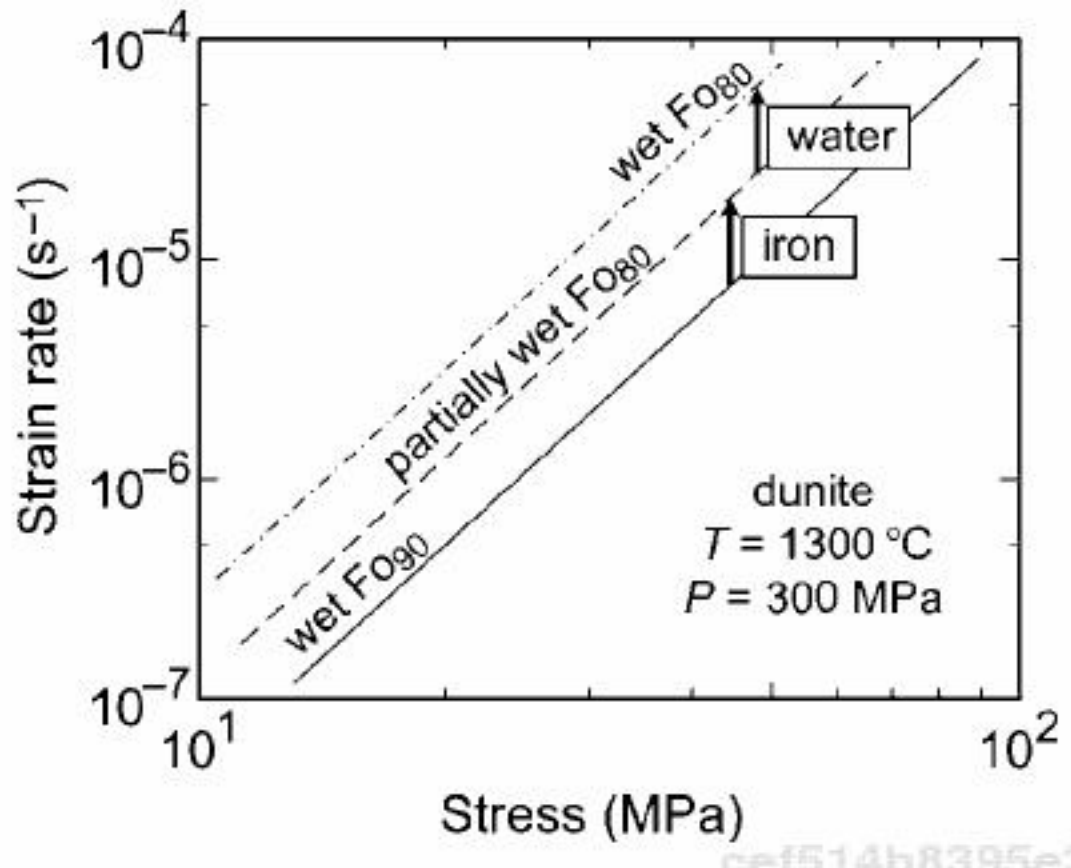

Figure 9.13. Log–log plot of strain rate versus differential stress illustrating the effect on creep rate behavior of increasing iron content in olivine. Based on Figure 9.12, at a given stress, the strain rate increases as iron content increases. In addition, water solubility increases with increasing iron content, thus further increasing the strain rate.

It is interesting to speculate about the potential effect on the tectonic history of Mars if the Martian mantle is weaker than Earth's mantle. Present-day Mars lacks plate tectonics, and the only evidence consistent with an episode of plate tectonics earlier in its history is the poorly understood magnetic reversal structures recorded in the southern highlands (Connerney, 1999). Thus, Martian mantle dynamics have been dominated by stagnant-lid convection over much of its history (Reese *et al.*, 1998), rather than Earth-like plate tectonics for which heat dissipation occurs predominantly through subduction of cold oceanic lithosphere. In stagnant-lid mode, most heat dissipation occurs through volcanic activity and, potentially, through crustal delamination. On Mars, abundant evidence of plumes exists in the formation of Tharsis Rise and in the very long effusive history of the massive volcanoes, including Olympus Mons and the Tharsis volcanoes.

While few true constraints exist on the evolution of a stagnant-lid planet as a function of mantle water content, it seems reasonable to assume that lower viscosities resulting from iron enrichment and higher water content than Earth would favor more active convection and effective heat transport from the deep interior to near the surface. A feedback system involving increased internal temperatures driving convective vigor, and consequent thermal erosion of the lithosphere, would tend to maintain a lithospheric thickness that permitted sufficient heat loss to stabilize the interior dynamics of the planet. The observation of a thick lithosphere on Mars would appear to argue that the mantle viscosity is higher than on Earth. Hence, even though the iron content of the Martian interior is relatively high, mantle viscosity is actually higher than on Earth because the temperature is lower and/or the water

content is depleted in the Martian interior, perhaps due to early water loss. Such early water loss and gradually decreasing temperature might allow development of a stagnant lid following an early period of plate tectonics.

4 Partial melting: Io

On Earth, the rheological behavior of partially molten rocks has been studied largely in the context of deformation and melt transport at mid-ocean ridges and in mantle plumes, where viscosities on the order of 10^{18} to 10^{20} Pa s are expected (Hirth and Kohlstedt, 1996; Ito *et al.*, 2003). Deformation experiments on partially molten lherzolites (Cooper and Kohlstedt, 1984, 1986; Bussod and Christie, 1991; Zimmerman and Kohlstedt, 2004), harzburgites (Bai *et al.*, 1997), and mixtures of olivine plus mid-ocean ridge basalt (MORB) (Hirth and Kohlstedt, 1995a,b) demonstrate only a modest reduction in viscosity with the addition of a small amount of melt; for a melt fraction $\varphi = 0.05$, viscosity decreases by a factor of ~4 relative to melt-free samples. On Io, the most volcanically active body in our solar system, magma transports tidally generated heat out of the mantle to the surface. Models of heat dissipation of tidal energy needed to balance the surface heat flux on Io require relatively low viscosities, as low as 10^8 to 10^{12} Pa s if dissipation occurs dominantly in a low-viscosity asthenosphere or on the order of 10^{16} to 10^{17} Pa s if dissipation takes place mantle wide (Segatz *et al.*, 1988; Tackley *et al.*, 2001). These lower values for viscosity require very large melt fractions, while the higher values necessitate very high temperatures and/or melt contents significantly greater than present in partially molten rocks beneath mid-ocean ridges on Earth.

4.1 Deformation of partially molten rocks

4.1.1 Effect of melt on deformation

The influence of melt on the deformation behavior of partially molten rocks depends critically on the grain-scale distribution of the melt phase (e.g., Kohlstedt, 1992, 2002; Xu *et al.*, 2004). The melt distribution, in turn, is usually described in terms of two parameters, the dihedral angle, θ, and the melt fraction, φ (von Bargen and Waff, 1986). The dihedral angle, the angle between two crystalline grains in contact with a liquid phase, is illustrated in Figures 9.14 and 9.15. Physically, the dihedral angle is a measure of the solid–solid interfacial energy, γ_{ss}, (e.g., grain boundary energy) relative to the solid–liquid interfacial energy, γ_{sl}:

$$\cos\left(\frac{\theta}{2}\right) = \frac{\gamma_{ss}}{2\gamma_{sl}}. \tag{9.29}$$

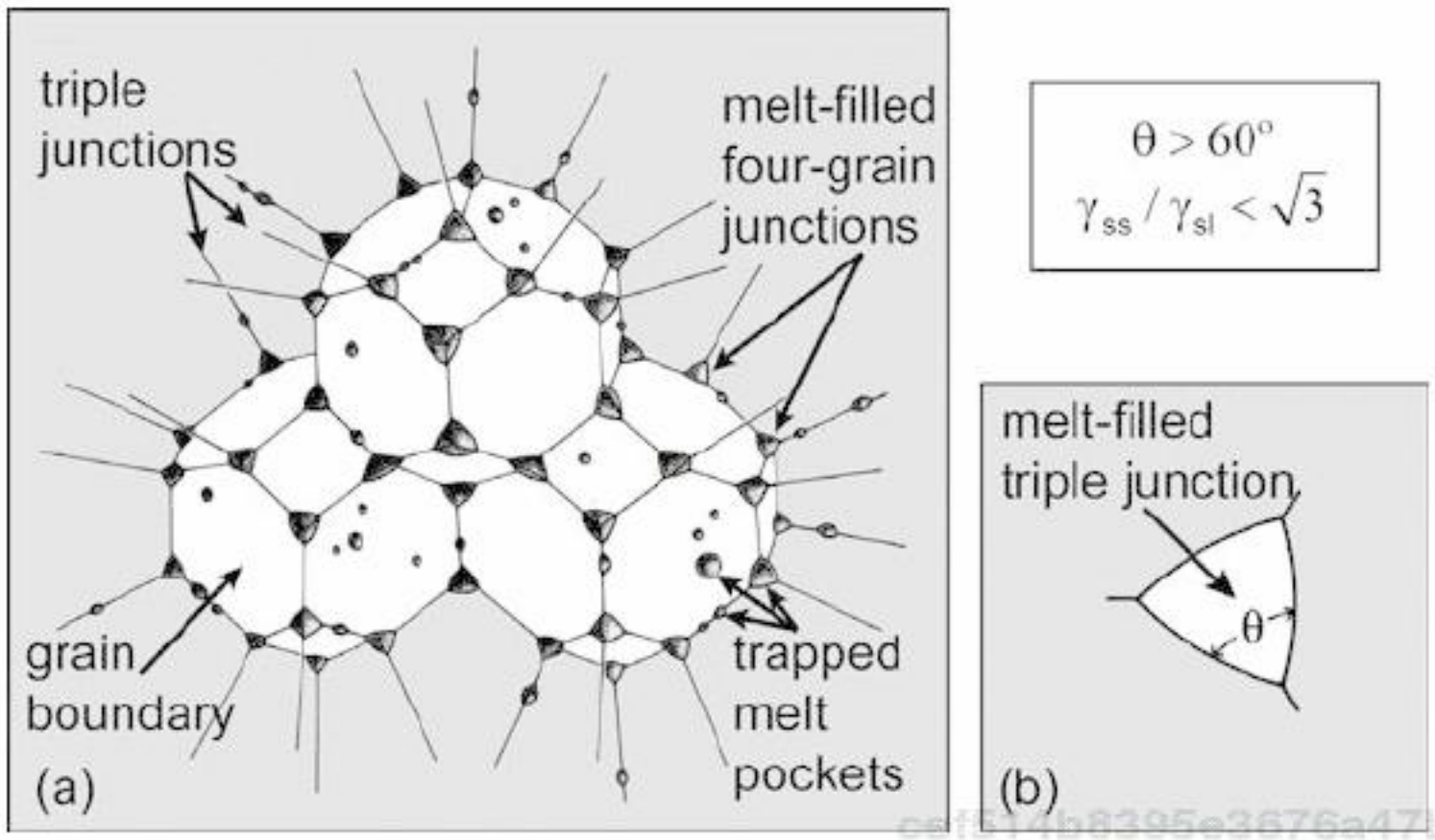

Figure 9.14. Melt distribution for solid–liquid system in which $\theta > 60°$. Melt is confined to isolated pockets, at least below a critical melt fraction. (a) Three-dimensional drawing of melt distribution illustrating trapped melt at four-grain junctions, in three-grain junctions, and on grain boundaries. (b) Two-dimensional cross-sectional view through melt pocket trapped along triple junction in (a). Modified from Lee *et al.* (1991).

In terms of dihedral angle or, equivalently, interfacial energies, three distinct regimes can be defined. (1) For solid–liquid systems in which the solid–liquid interfacial energy is relatively large (i.e., $\gamma_{ss} < \sqrt{3}\,\gamma_{sl}$), grain boundaries are favored over solid–liquid interfaces. Such systems are characterized by a large dihedral angle, $\theta > 60°$, with the fluid confined to isolated pockets, at least below a critical melt fraction (von Bargen and Waff, 1986), as illustrated in Figure 9.14. Examples of such systems involving silicate rocks include hydrous fluids, at least at modest pressures and high temperatures (Watson and Brenan, 1987; Brenan and Watson, 1988; Lee *et al.*, 1991; Holness and Graham, 1991; Holness, 1993; Mibe *et al.*, 1998; Hier-Majumder and Kohlstedt, 2006), and metal-sulfide melts, at least at low to modest pressures (Minarik *et al.*, 1996; Ballhaus and Ellis, 1996; Gaetani and Grove, 1999; Hustoft and Kohlstedt, 2006). (2) For solid–liquid systems in which the solid–liquid energy is relatively small (i.e., $\gamma_{sl} \leq \gamma_{ss}/2$), the fluid forms a thin film along all of the grain boundaries, and the solid–fluid system is characterized by $\theta = 0°$. Dihedral angles approaching zero have been observed in some analogue systems such as camphor-benzoic acid eutectic (Takei, 2000; Takei and Shimizu, 2003) and in some high-temperature structural ceramic materials (Lange *et al.*, 1980; Clarke, 1987). (3) For intermediate conditions with $0 < \theta \leq 60°$ (i.e., $\sqrt{3}\,\gamma_{sl} \leq \gamma_{ss} < 2\gamma_{sl}$), liquids form interconnected networks along triple junctions, as illustrated in Figure 9.15. Partially molten silicates frequently fall into this category (Waff and Bulau, 1979; Toramaru and Fujii, 1986), as do important analogue

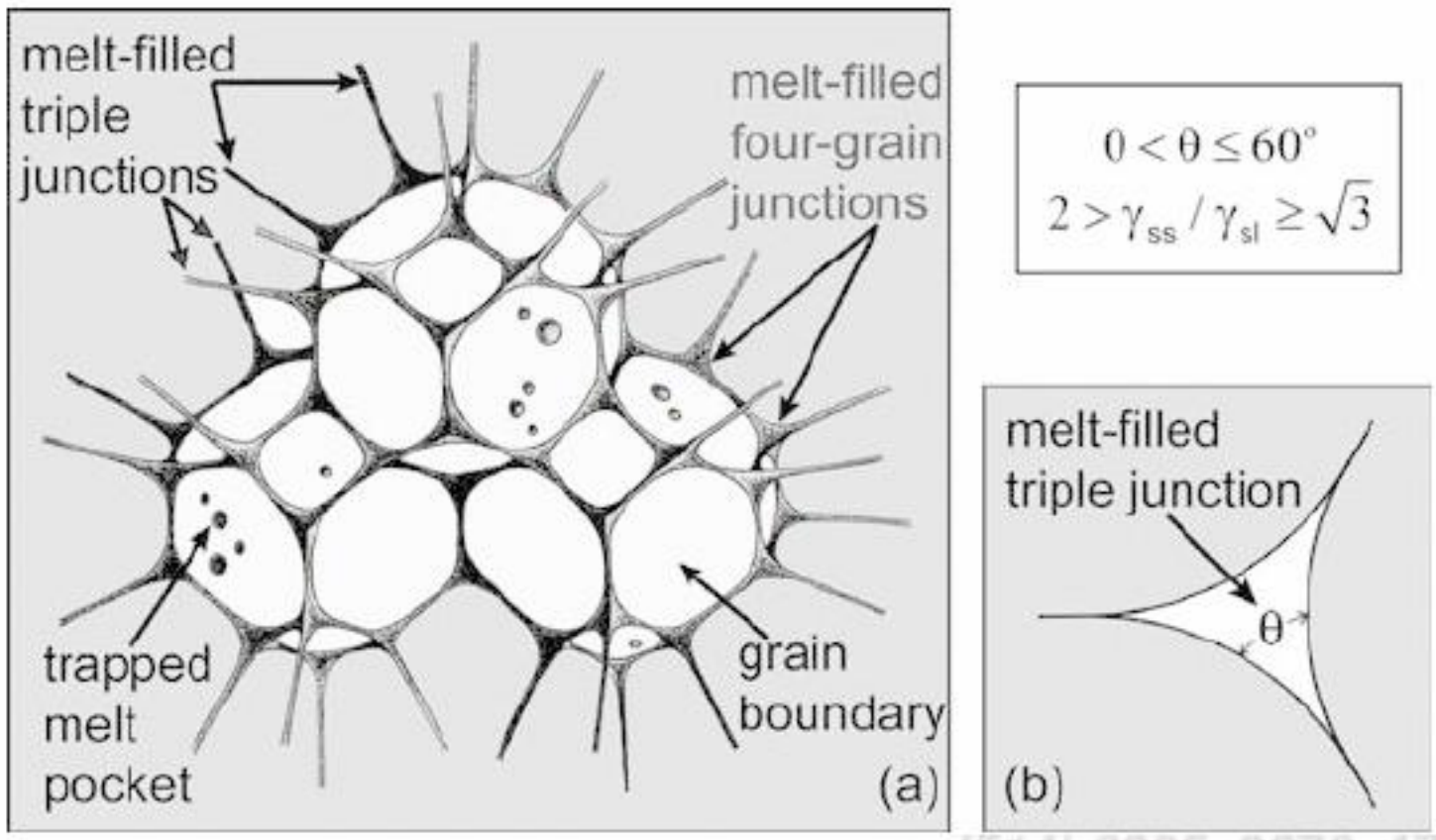

Figure 9.15. Melt distribution for solid–liquid system in which $0 < \theta \leq 60^\circ$. Melt is distributed along all triple junctions and in all four-grain junctions, even at very small melt fractions. (a) Three-dimensional drawing of melt distribution illustrating melt tubules along triple junctions passing through four-grain junctions. Melt can be trapped on grain boundaries. (b) Two-dimensional cross-sectional view through melt-filled triple junction viewed in three dimensions in (a). Modified from Lee *et al.* (1991).

materials used to study the effect of a liquid phase on acoustic properties (Takei, 2000).

In a recent series of papers, Takei (1998, 2000, 2001, 2002) has emphasized characterization of melt distribution in terms of the wetness parameter, ψ,

$$\psi = \frac{A_{sl}}{A_{sl} + 2A_{ss}}, \tag{9.30}$$

where A_{sl} and A_{ss} are the solid–liquid and solid–solid interfacial areas; in brief, ψ is the ratio of the wetted area to the total interfacial area for each grain. In her papers, Takei discusses the wetness as the link between microscopic melt distribution and macroscopic properties. Hence, wetness can be taken as a state parameter, such as introduced in Equation (9.1). In an isotropic solid–liquid system at thermodynamic equilibrium, wetness incorporates both the dihedral angle and melt fraction (e.g., von Bargen and Waff, 1986); as the dihedral angle decreases and/or melt fraction increases, ψ increases. Wetness is an important parameter for characterizing melt distribution because, unlike the combination of dihedral angle and melt fraction, wetness can be determined for solid–liquid systems that have anisotropic interfacial energies (i.e., cannot be described by a single dihedral angle). In addition, wetness can be measured, either directly from micrographs or indirectly from properties such as seismic velocities, under non-hydrostatic (i.e., deformation) conditions (Takei, 2001).

For each of the three types of melt morphology noted above, the influence of the fluid phase of the viscosity of the fluid–rock system is different. (i) In the case of a non-wetting liquid at small melt fractions in which liquid is confined to isolated pockets, the liquid only modestly influences viscosity. The primary effect of the liquid phase is to reduce the amount of grain-to-grain contact and thus increase the local stress. Since the fluid is not interconnected, it cannot significantly enhance diffusion mass transport (Chen and Argon, 1979; Tharp, 1983). (ii) If the liquid phase totally wets the grain boundaries, the rates of ionic diffusion are generally significantly enhanced relative to rates of diffusion along melt-free grain boundaries. As a result, the contribution of diffusion creep in which grain boundary transport dominates is greatly enhanced. This effect could be expressed by replacing D_{gb} in Equation (9.4) with D_{film}, where typically $D_{film} \gg D_{gb}$ (e.g., Elliot, 1973; Rutter, 1976; Raj, 1982). It should be noted that it is the flux of ions along grain boundaries that is important in determining the rate of diffusion creep, not simply the grain boundary diffusivity. Hence, if the solubilities of ions that compose the crystalline grains are negligible in the film, then the deformation rate will not be significantly enhanced (Gust *et al.*, 1993), since flux is proportional to the product of diffusivity times concentration. (iii) If the fluid phase is restricted to triple junctions, it influences the deformation behavior of partially molten rocks in at least two ways (Cooper *et al.*, 1989). First, the presence of melt reduces the load-bearing area of a rock, thus increasing the local differential stress. Second, because diffusion through melt is significantly faster than diffusion through melt-free grain boundaries, the presence of melt in triple junctions effectively reduces the distance that ions have to diffuse in traveling from regions of compression to regions of tension (or lower compressive stress), thus increasing the contribution of diffusion creep.

Flow laws developed to describe creep of melt-bearing rocks have the general form

$$\dot{\varepsilon}_{\varphi} \equiv \dot{\varepsilon}(\theta,\varphi) = \dot{\varepsilon}_{\varphi=0}\mathcal{F}(\theta,\varphi), \tag{9.31}$$

where $\dot{\varepsilon}_{\varphi=0}$, the strain rate of a melt-free sample, takes on the appropriate form from the equations written above for diffusion and dislocation creep. Based on an analysis of diffusion creep rate-limited by grain boundary diffusion with a melt distribution for an isotropic melt–solid system, $\mathcal{F}(\theta,\varphi)$ is given by (Cooper *et al.*, 1989)

$$\mathcal{F}(\theta,\varphi) = \left(\frac{1}{1-(\Delta d'/d')}\right)^2_{sc}\left(\frac{1}{1-(\Delta d'/d')}\right)^2_{se} = \left(\frac{1}{1-\varphi^{1/2}g(\theta)}\right)^4. \tag{9.32}$$

In this analysis, a fraction of the grain boundary contact, $\Delta d'/d'$, is replaced by melt. In Equation (9.32), the subscripts *sc* and *se* indicate the effects of strain rate enhancement due to rapid diffusion (short-circuit, *sc*, diffusion) through the melt phase, and of local stress enhancement (*se*) due to the reduction of grain-to-grain contact on creep rate, respectively. The term $g(\theta)$ is given by

$$g(\theta) = \frac{1.06 \sin(30^\circ - (\theta/2))}{\left(\frac{1+\cos\theta}{\sqrt{3}} - \sin\theta - \frac{\pi}{90}(30^\circ - (\theta/2))\right)^{1/2}}. \tag{9.33}$$

A recent extension of this model for diffusion creep of partially molten rocks from two dimensions to three dimensions, including the observed anisotropic wetting of grains, has been initiated by Takei and Holtzman (2009a,b,c). In this 3-D model, the viscosity of a partially molten rock is expressed in terms of grain boundary wetness. This model for deformation in the diffusion creep regime predicts a factor of five decrease in viscosity with a very small increase in melt fraction from $\varphi = 0$ to $\varphi = 0.001$, a result not anticipated by the Cooper-Kohlstedt model. This factor of five decrease in viscosity associated with an increase in φ from 0 to 0.001 has yet to be verified experimentally. One possible explanation for this observation is that, in general, samples synthesized for physical property measurements contain a trace amount of melt. This melt forms due to impurities introduced from the crushing and grinding processes or due to inclusions within the olivine crystals used to prepare the powders from which samples are fabricated (Faul and Jackson, 2006). Therefore, truly melt-free samples ($\varphi = 0$) have not for the most part formed the baseline for examining the effect of melt on creep of mantle rocks.

In reality, melt has a larger effect on strain rate than that predicted by Equations (9.31) to (9.33), in part at least because melt wets not only all of the triple junctions but also some fraction of the grain boundaries due to the anisotropic wetting properties of most crystalline materials (e.g., Cooper and Kohlstedt, 1982; Waff and Faul, 1992; Hirth and Kohlstedt, 1995a), as illustrated with the transmission electron micrograph in Figure 9.16. In addition, the fraction of grain boundaries wetted by melt increases with increasing melt fraction (Hirth and Kohlstedt, 1995a) and, as discussed below, melt distribution is markedly affected by deformation (Kohlstedt and Zimmerman, 1996; Zimmerman *et al.*, 1999; Holtzman *et al.*, 2003a,b). Also, the presence of melt at triple junctions helps to mitigate the buildup of stresses at these three grain junctions, thus relaxing constraints on grain boundary sliding (Hirth and Kohlstedt, 1995b). Although these factors have yet to be incorporated into a comprehensive model for deformation, the dependence of creep rate on the melt fraction of partially molten ultramafic rocks is reasonably well described by the empirical relation (Kelemen *et al.*, 1997)

$$\mathcal{F}(\theta,\varphi) = \exp(\alpha(\theta)\varphi), \tag{9.34}$$

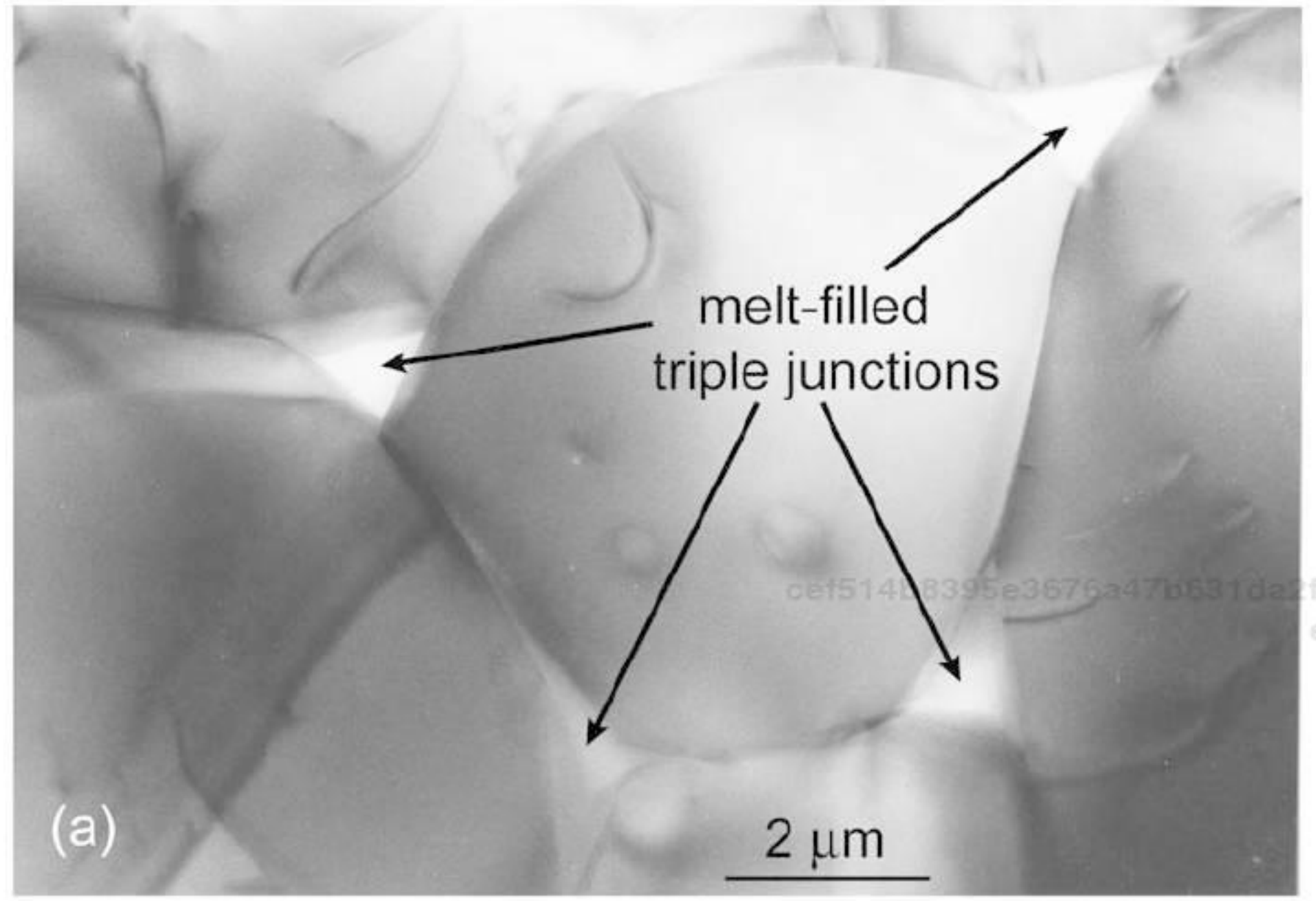

Figure 9.16. Transmission electron micrographs of melt distribution in partially molten aggregate of olivine plus mid-ocean ridge basalt. Melt is present in all triple junctions, as well as along some grain boundaries. From Kohlstedt (2002) with permission from MSA.

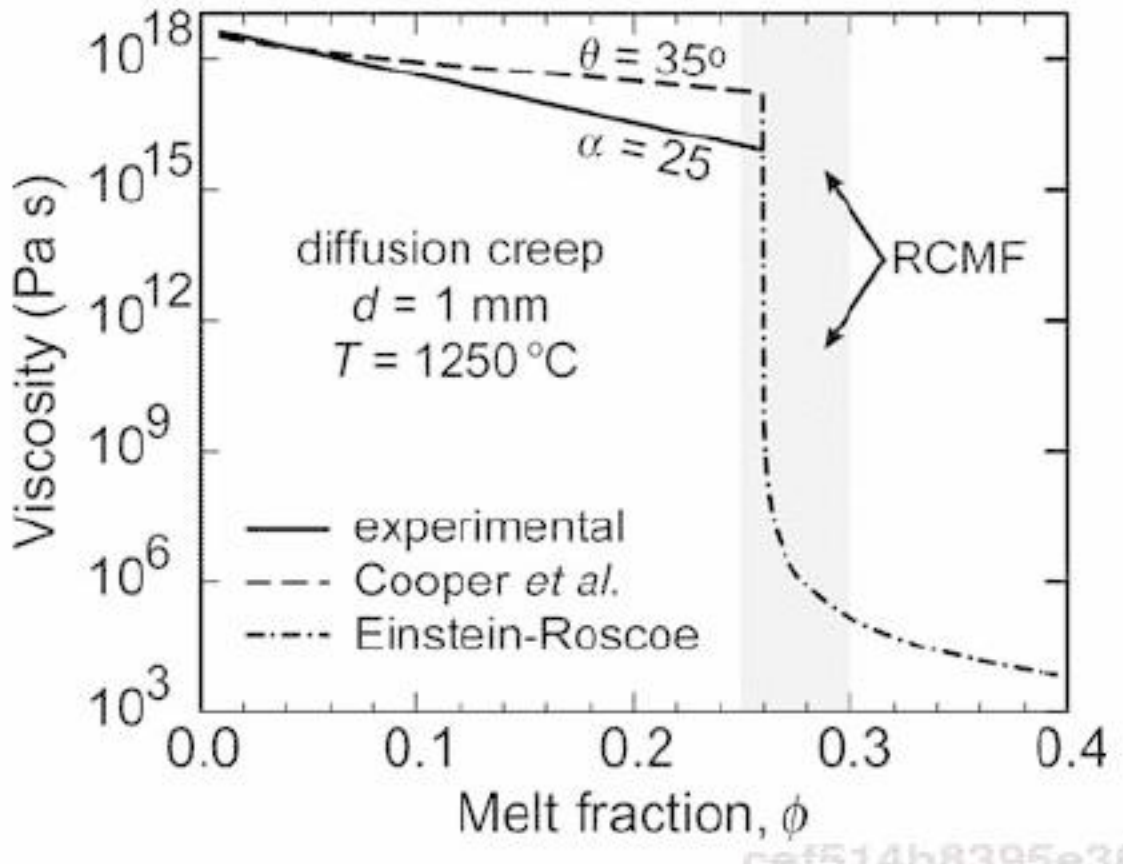

Figure 9.17. Semi-log plot of viscosity as a function of melt fraction for the diffusion creep regime. The dashed line is based on Equations (9.31) and (9.32) for $\theta = 35^\circ$. The solid line is an empirical fit of experimental data to Equation (9.34) with $\alpha = 25$. The dot-dashed line is an extrapolation to higher melt fractions using the Einstein-Roscoe relationship in Equation (9.35). The shaded region identifies the rheologically critical melt fraction for the olivine plus basalt system based on experiments by Scott and Kohlstedt (2006).

with the value of $\alpha(\theta)$ being somewhat larger in the dislocation creep regime than in the diffusion creep regime (Mei *et al.*, 2002; Zimmerman and Kohlstedt, 2004). It should be noted that the recent 3-D model of Takei and Holtzman (2009a) also provides a good fit to the experimental data for deformation of partially molten rocks in the diffusion creep regime, at least for $\varphi \geq 0.01$.

At very high melt fractions, a transition occurs from deformation that is largely controlled by a framework of grains to one governed by a suspension of grains in a melt. In the olivine plus basalt system, this transition occurs for a rheologically critical melt fraction (RCMF) in the range $0.25 \leq \varphi \leq 0.30$ (Scott and Kohlstedt, 2006). At melt fractions greater than the RCMF, deformation is often described by the Einstein-Roscoe equation (Einstein, 1906, 1911; Roscoe, 1952)

$$\eta_{\text{rock}} = \frac{\eta_{\text{melt}}}{(1.35\varphi - 0.35)^{2.5}}, \tag{9.35}$$

which leads to a very rapid decrease in viscosity with increasing melt fraction. The decrease in viscosity with increasing melt fraction is illustrated in Figure 9.17 for the diffusion creep regime. At melt fractions up to $\varphi \approx 0.05$, the model for diffusion creep given by Equations (9.31–9.33) and the empirical relation described by Equation (9.34) yield similar results. At higher melt fractions, however, the viscosity of partially molten rocks decreases more rapidly than predicted by this model. Above $\varphi \approx 0.26$, viscosity decreases very quickly with increasing melt fraction as a transition occurs from framework-like to suspension-like behavior.

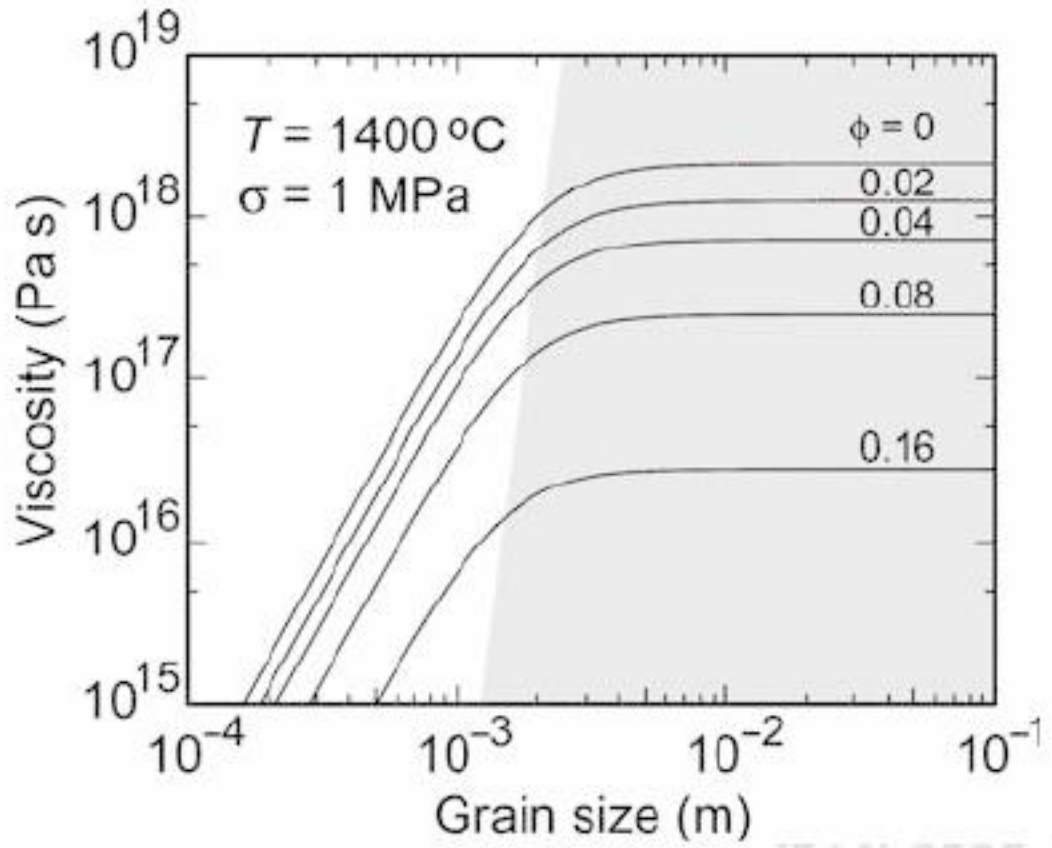

Figure 9.18. Log–log plot of viscosity as a function of grain size at 1400 °C and a stress of 1 MPa for several melt fractions based on Equation (9.34), with values of $\alpha_{\text{diff}} = 21$ in the diffusion creep regime and $\alpha_{\text{disl}} = 27$ in the dislocation creep regime (shaded region), based on the laboratory experiments of Zimmerman and Kohlstedt (2004) on partially molten lherzolite samples. Since $\alpha_{\text{diff}} < \alpha_{\text{disl}}$, the boundary between the two creep regimes moves toward smaller grain size with increasing melt fraction. In the diffusion creep regime, viscosity increases as the cube of the grain size.

The dependence of viscosity on melt fraction based on laboratory experiments and described by Equation (9.34) is further explored in Figure 9.18. Flow law parameters were taken from an experimental study of creep of partially molten lherzolite (Zimmerman and Kohlstedt, 2004). In the diffusion creep regime, $\alpha_{\text{diff}} = 21$, $Q = 370$ kJ/mol, $n = 1$ and $p = 3$, while in the dislocation creep regime $\alpha_{\text{disl}} = 27$, $Q = 550$ kJ/mol, $n = 4.3$ and $p = 0$. Results are shown for a temperature of 1400 °C and a differential stress of 1 MPa. For a melt-free sample, the viscosity is $\sim 10^{18}$ Pa s for a grain size ≥ 1 mm and decreases with decreasing grain size below ~ 1 mm as diffusion creep becomes increasingly important. In the dislocation creep regime in which the viscosity is stress dependent, the viscosity will increase to $\sim 10^{20}$ Pa s if the differential stress is decreased to 0.3 MPa. This range of viscosity is in good agreement with values calculated from observation of postglacial rebound (e.g., Peltier, 1998; Kaufmann and Lambeck, 2002) and analyses of the geoid on Earth (Craig and McKenzie, 1986; Hager, 1991; Panasyuk and Hager, 2000).

4.1.2 Effect of deformation/stress on melt distribution

Not only does a small amount of melt weaken a partially molten rock, but also the distribution of melt changes in response to an applied stress. The scale at which redistribution of melt in a deforming rock takes place is governed by the compaction length, δ_c, that is, the distance over which melt flow and matrix deformation are

coupled, such that pressure gradients can develop in the fluid, leading to melt segregation (McKenzie, 1984; Scott and Stevenson, 1986). Here we use a simplified form of the expression for compaction length in terms of the shear viscosity of the partially molten rock, η, the permeability of the partially molten rock, k, and the viscosity of the melt, μ. The bulk viscosity is assumed to be smaller than or comparable to the shear viscosity, so that

$$\delta_c \approx \sqrt{k\frac{4/3\eta}{\mu}}. \tag{9.36}$$

In experiments, melt segregation occurs if the compaction length is less than or on the order of the sample thickness, that is, $\delta_c \leq \delta_t$, and does not occur in samples for which $\delta_c \gg \delta_t$. However, even if $\delta_c \gg \delta_t$, melt reorients in response to the applied stress, even though large-scale segregation does not occur. This point is illustrated directly in samples of olivine plus a few percent basalt sheared to large strain, as shown in Figure 9.19 (Kohlstedt and Zimmerman, 1996; Zimmerman *et al.*, 1999). In these samples, the compaction length is ~10 mm, while the sample thickness is <1 mm (Holtzman *et al.*, 2003a). Stress-induced anisotropy of a partially molten analogue material of unknown compaction length has also been identified *in situ* using ultrasonic shear waves (Takei, 2001).

If $\delta_c \leq \delta_t$, melt segregates into a network of melt-rich bands that are separated by melt-depleted lenses, as illustrated in Figure 9.20, an optical micrograph of a sample deformed to high strain in simple shear. Before deformation, melt was homogeneously distributed, similar to the melt distribution in Figure 9.19a, with a starting melt fraction of $\varphi \approx 0.04$. After deformation, the anastomosing network of bands contains a relatively large melt fraction, $\varphi \approx 0.2$, while the melt-depleted lenses contain a much smaller melt fraction, $\varphi \approx 0.01$. One of the striking features of the melt-rich bands is that they are oriented, on average, ~20° to the shear plane but antithetic to the shear direction. This average orientation of the bands does not increase with increasing shear strain but remains, on average, approximately constant. Since the bands must rotate with the flow field of the matrix, they reach a maximum angle of ~30°, beyond which the melt pressure in the bands increases, forcing flow in the resulting pressure gradient. Melt can then flow from the bands at higher angles to those at lower angles through the network of high-permeability, melt-rich pathways.

Segregation of melt into melt-rich bands during high-strain experiments has a pronounced influence on both viscosity and permeability of the rock. As melt fraction rises in the melt-rich bands, extracting melt from neighboring regions, the viscosity of the bands decreases thus localizing deformation into narrow melt-rich shear zones. Likewise, as the melt fraction in the bands increases, permeability

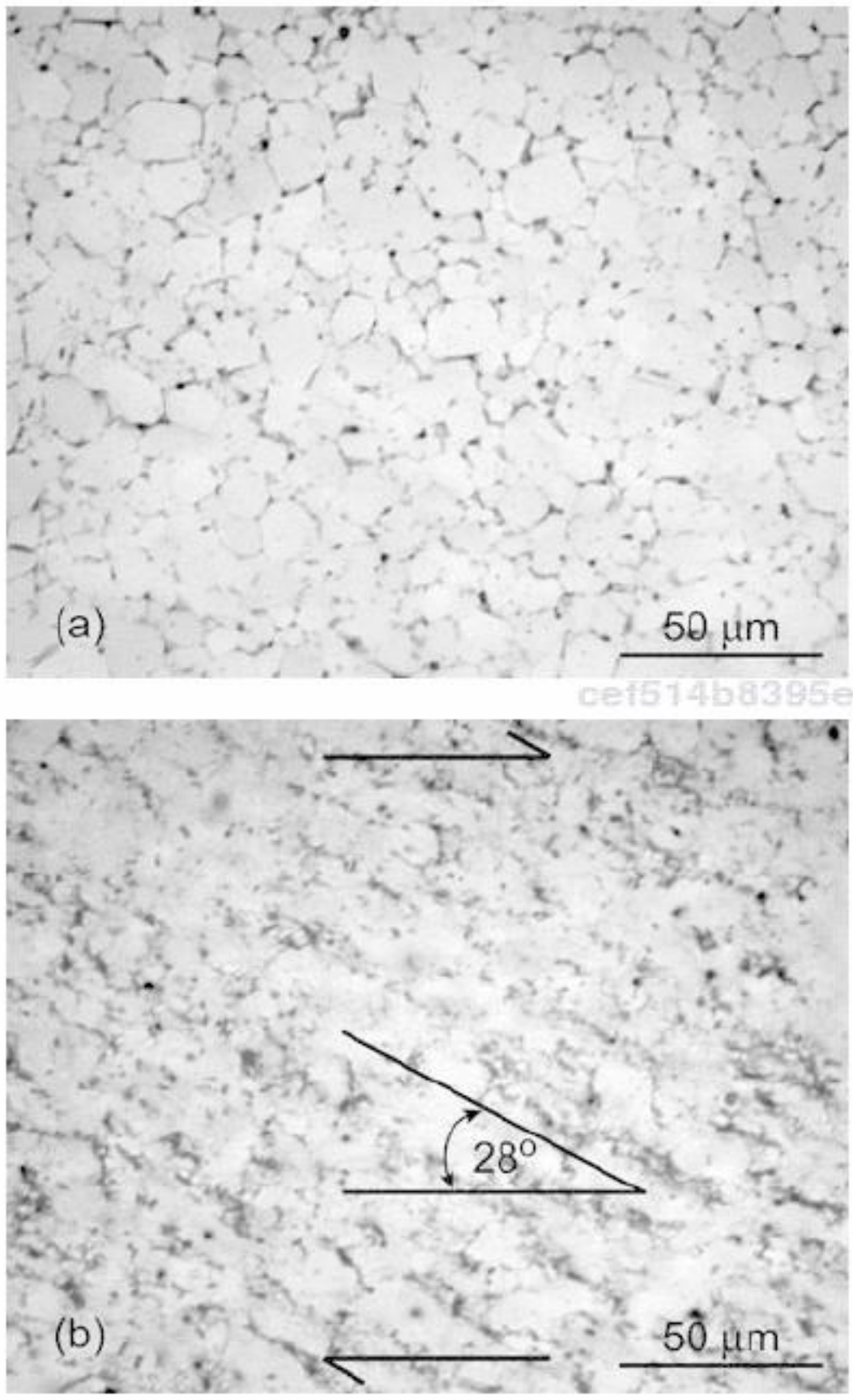

Figure 9.19. Reflected light optical micrographs of partially molten samples of olivine plus basalt. (a) In a hydrostatically annealed sample, melt is distributed in triple junctions, as well as along some grain boundaries. (b) In a sheared sample, melt is aligned ~28° to the shear plane and antithetic to the shear direction.

increases since permeability scales approximately as melt fraction squared or cubed (Turcotte and Schubert, 1982, pp. 383–384). Hence, the fluid-rich bands provide paths for rapid transport of melt and aqueous fluids from deep within the mantle to the surface (Daines and Kohlstedt, 1997; Holtzman *et al.*, 2003a,b; Hier-Majumder and Kohlstedt, 2006).

4.2 Application to Io

Io is characterized by extensive volcanic activity and an associated high surface heat flux, which is approximately 35 times that of Earth (Keszthelyi and McEwen, 1997; Lopes *et al.*, 2001). On Io, internal heat is generated by tidal dissipation associated with its Laplace resonance with Europa and Ganymede as the

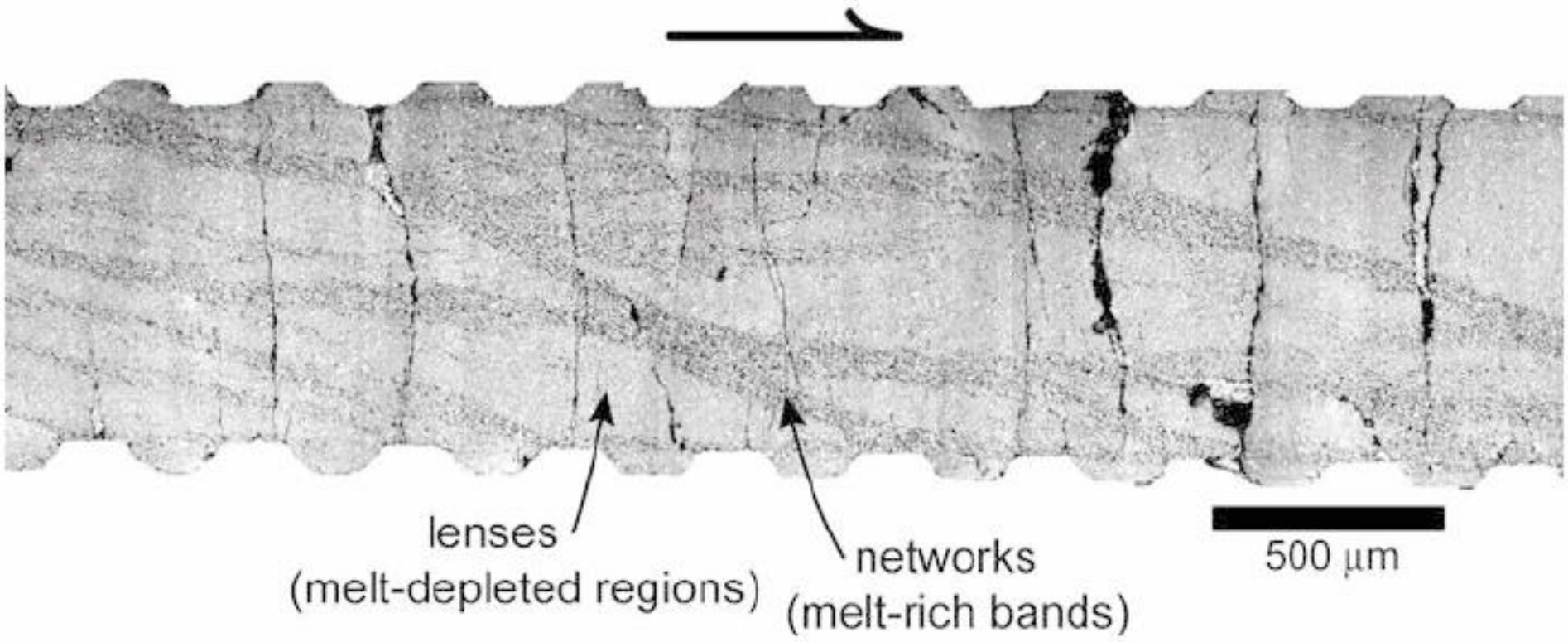

Figure 9.20. Reflected light optical micrograph of sample of olivine plus basalt plus chromite deformed in simple shear to a strain of ~3. The melt-rich bands are dark, while the melt-depleted lenses are light. The vertical cracks developed during cooling and depressurization due to the mismatch in elastic constants and thermal expansion between the samples and the tungsten pistons. The grooves along the top and bottom of the sample were formed by the pistons, which were serrated to prevent slip between the sample and the pistons.

three satellites orbit Jupiter. Two models have been proposed to account for this large amount of heating within Io. In the first, tidal heat is dissipated throughout the entire mantle with a viscosity of $\sim 10^{16}$–10^{17} Pa s; in this model, most of the tidal heating occurs near the core-mantle boundary (Ross and Schubert, 1985, 1986; Segatz *et al.*, 1988). Such a model appears to require that the entire mantle remains just above the solidus temperature throughout its depth in order to maintain these low viscosities. In the second model, heat is primarily dissipated in a thin, ~100-km thick asthenosphere with a viscosity of $\sim 10^{8}$–10^{12} Pa s (Segatz *et al.*, 1988).

A viscosity of $< 10^{12}$ Pa s cannot be obtained at 1400 °C without a melt fraction exceeding the rheologically critical melt fraction, as illustrated in Figures 9.17 and 9.18. Even at a temperature of 1600 °C, Figure 9.21, the temperature of the hottest lavas erupting on Io, viscosity is $> 10^{13}$ Pa s unless the melt fraction exceeds 0.15 or the grain size is less than ~10 μm. It is unlikely that grain size will be that small at such a high temperature for which grain growth should be rapid. The differential stress in such a system is also expected to be small, such that the dynamically recrystallized grain size should be relatively large (~10 mm for $\sigma =$ 1 MPa; van der Wal *et al.*, 1993). As pointed out by Tackley *et al.* (2001), if the melt fraction is large, gravity-driven compaction and associated melt extraction will almost certainly occur, thus forcing an increase in viscosity by reducing the melt fraction. Such extraction will be further enhanced in a convective regime for which melt segregation due to deformation will significantly increase permeability

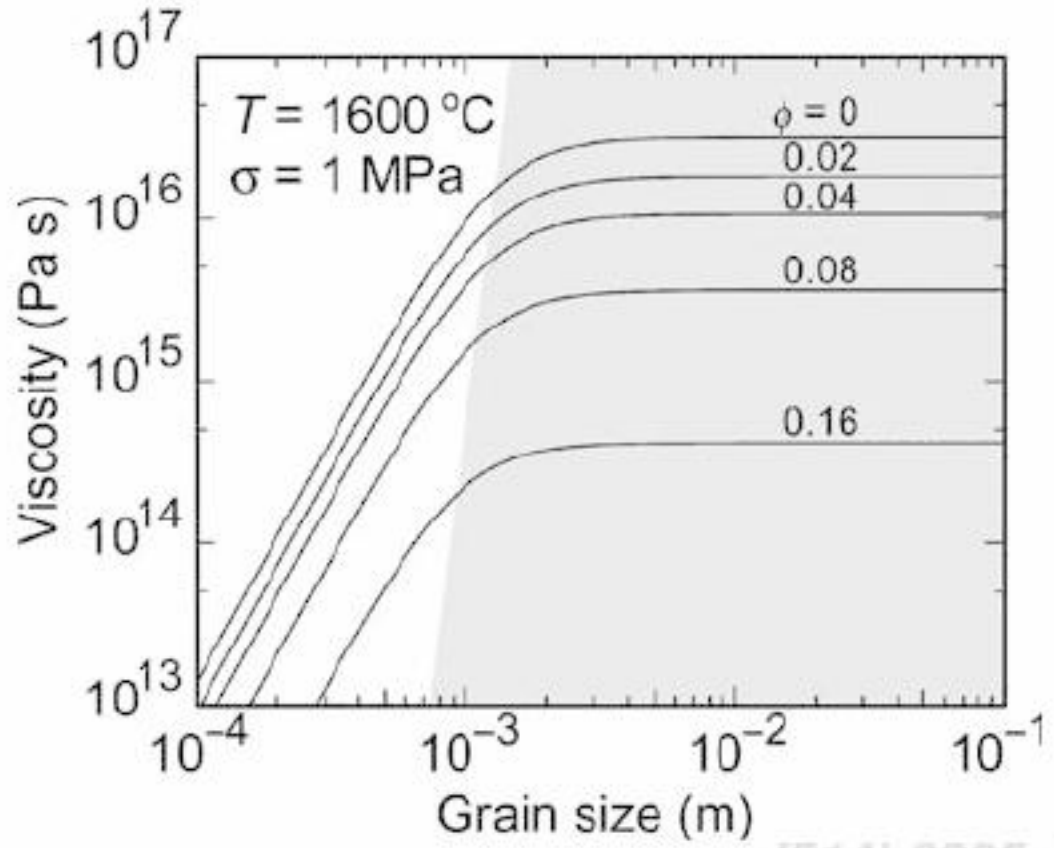

Figure 9.21. Log–log plot of viscosity as a function of grain size at 1600 °C and a stress of 1 MPa for several melt fractions based on Equation (9.34), with the same values for creep parameters as used in Figure 9.17.

(Holtzman *et al.*, 2003a,b). Hence, mantle viscosity cannot be less than $\sim 10^{16}$ Pa s, and an extremely low viscosity asthenosphere appears to be unsustainable. Thus, experimental constraints favor models of whole mantle convection on Io at high temperatures (~1600 °C) and relatively low melt fractions (<0.01).

Acknowledgments

The authors thank Ben Holtzman for his intellectual input and artistic skill in preparing Plate 26. The authors greatly appreciate the detailed critique provided by Laurent Montési. Support from NASA grants NNG04G173G and NNX07AP68G through the Planetary Geology and Geophysics Program to DLK and under CAN-NCC5–679 to SJM is gratefully acknowledged. Support from NSF grants OCE-0648020 (deformation of partially molten rocks) and EAR-0439747 (deformation of nominally anhydrous minerals) to DLK is also gratefully acknowledged. This chapter is LPI contribution #1240.

References

Bai, Q., Mackwell, S. J., and Kohlstedt, D. L. (1991). High-temperature creep of olivine single crystals: 1. Mechanical results for buffered samples. *J. Geophys. Res.*, **96**, 2441–2463.

Bai, Q., Jin, Z., and Green, H. W. (1997). Experimental investigation of partially molten peridotite at upper mantle pressure and temperature. In *Deformation Enhanced Fluid Transport in the Earth's Crust and Mantle*, ed. M. Holness. London: Chapman & Hall.

Ballhaus, C. and Ellis, D. J. (1996). Mobility of core melts during Earth's accretion. *Earth Planet. Sci. Lett.*, **143**, 137–145.

Barr, A. C., Pappalardo, R. T., and Zhong, S. (2004). Convective instability in ice I with non-Newtonian rheology: Application to the icy Galilean satellites. *J. Geophys. Res.*, **109**, E12008, doi:10.1029/2004JE002296.

Bindschadler, D. L., Schubert, G., and Kaula, W. M. (1992). Coldspots and hotspots: Global tectonics and mantle dynamics of Venus. *J. Geophys. Res.*, **97**, 13 495–13 532.

Blanchard, M. and Ingrin, J. (2004). Kinetics of deuteration in pyrope. *Eur. J. Mineral.*, **16**, 567–576.

Brace, W. F. and Kohlstedt, D. L. (1980). Limits on lithospheric stress imposed by laboratory experiments. *J. Geophys. Res.*, **85**, 6248–6252.

Braithwaite, J. S., Wright, K., and Catlow, C. R. A. (2003). A theoretical study of the energetics and IR frequencies of hydroxyl defects in forsterite. *J. Geophys. Res.*, **108**, 2284, doi:10.1029/2002JB002126.

Brenan, J. M. and Watson, E. B. (1988). Fluids in the lithosphere: 2. Experimental constraints on CO_2 transport in dunite and quartzite at elevated P-T conditions with implications for mantle and crustal decarbonation processes. *Earth Planet. Sci. Lett.*, **91**, 141–158.

Brodholt, J. P. and Refson, K. (2000). An *ab initio* study of hydrogen in forsterite and a possible mechanism for hydrolytic weakening. *J. Geophys. Res.*, **105**, 18 977–18 992.

Buening, D. K. and Buseck, P. R. (1973). Fe–Mg lattice diffusion in olivine. *J. Geophys. Res.*, **78**, 6852–6862.

Bussod, G. Y. and Christie, J. M. (1991). Textural development and melt topology in spinel lherzolite experimentally deformed at hypersolidus conditions. *J. Petrol., Spec. Vol.*, 17–39.

Byerlee, J. D. (1978). Friction of rocks. *Pure Appl. Geophys.*, **116**, 615–626.

Bystricky, M., Kunze, K., Burlini, L., and Burg, J.-P. (2000). High shear strain of olivine aggregates: Rheological and seismic consequences. *Science*, **290**, 1564–1567.

Bystricky, M. and Mackwell, S. (2001). Creep of dry clinopyroxene aggregates. *J. Geophys. Res.*, **106**, 13 443–13 454.

Caristan, Y. (1982). The transition from high temperature creep to fracture in Maryland diabase. *J. Geophys. Res.*, **87**, 6781–6790.

Carpenter Woods, S., Mackwell, S., and Dyar, D. (2000). Hydrogen in diopside: Diffusion profiles. *Amer. Min.*, **85**, 480–487.

Carter, C. B. and Sass, S. L. (1981). Electron diffraction and microscopy techniques for studying grain-boundary structure. *J. Am. Ceram. Soc.*, **64**, 335–345.

Chakraborty, S. (1997). Rates and mechanisms of Fe-Mg interdiffusion in olivine at 980° to 1300 °C. *J. Geophys. Res.*, **102**, 12 317–12 331.

Chapman, D. S. (1986). Thermal gradients in the continental crust. In *The Nature of the Continental Crust*, ed. J. B. Dawson, D. A. Carswell, J. Hall and K. H. Wedepohl, *Spec. Publ. Geol. Soc. London*, **24**, 63–70.

Chen, I. W. and Argon, A. S. (1979). Steady state power-law creep in heterogeneous alloys with microstructures. *Acta Metall.*, **27**, 785–791.

Chen, S., Hiraga, T., and Kohlstedt, D. L. (2006). Water weakening of clinopyroxene in the dislocation creep regime. *J. Geophys. Res.*, **111**, B08203, doi:10.1029/2005JB003885.

Chester, F. M. (1988). The brittle ductile transition in a deformation-mechanism map for halite. *Tectonophys.*, **154**, 125–136.

Chopra, P. N. and Paterson, M. S. (1984). The role of water in the deformation of dunite. *J. Geophys. Res.*, **89**, 7861–7876.

Clarke, D. R. (1987). On the equilibrium thickness of intergranular glass phases in ceramic materials. *J. Am. Ceram. Soc.*, **70**, 15–22.

Coble, R. (1963). A model for boundary diffusion controlled creep in polycrystalline materials. *J. Appl. Phys.*, **34**, 1679–1682.

Connerney, J. E. P., Acuña, M. H., Wasilewski, P. J., Ness, N. F., Rème, H., Mazelle, C., Vignes, D., Lin, R. P., Mitchell, D. L., and Cloutier, P. A. (1999). Magnetic lineations in the ancient crust of Mars. *Science*, **284**, 794–798.

Cooper, R. F. and Kohlstedt, D. L. (1982). Interfacial energies in the olivine–basalt system. In *High-Pressure Research in Geophysics, Advances in Earth and Planetary Sciences*, Vol. 12, ed. S. Akimota and M. H. Manghnani, Center for Academic Publications Japan, Tokyo, pp. 217−228.

Cooper, R. F. and Kohlstedt, D. L. (1984). Solution-precipitation enhanced creep of partially molten olivine-basalt aggregates during hot-pressing. *Tectonophys.*, **107**, 207–233.

Cooper, R. F. and Kohlstedt, D. L. (1986). Rheology and structure of olivine-basalt partial melts. *J. Geophys. Res.*, **91**, 9315–9323.

Cooper, R. F., Kohlstedt, D. L., and Chyung, C. K. (1989). Solution-precipitation enhanced creep in solid-liquid aggregates which display a non-zero dihedral angle. *Acta Metall.*, **37**, 1759–1771.

Costa, R. and Chakraborty, S. (2008). The effect of water on Si and O diffusion rates in olivine and implications for transport properties and processes in the upper mantle. Phys. Earth Planet. Inter. **166**, 11–29, doi:10.1016/j.pepi.2007.10.006.

Craig, C. H. and McKenzie, D. (1986). The existence of a thin low-viscosity layer beneath the lithosphere. *Earth Planet. Sci. Lett.*, **78**, 420–426.

Cuffey, K. M., Thorsteinsson, T., and Waddington, E. D. (2000a). A renewed argument for crystal size control of ice sheet strain rates. *J. Geophys. Res.*, **105**, 27 889–27 894.

Cuffey, K. M., Conway, H., Gades, A., Hallet, B., Raymond, C. F., and Whitlow, S. (2000b). Deformation properties of subfreezing glacier ice: Role of crystal size, chemical impurities, and rock particles inferred from in situ measurements. *J. Geophys. Res.*, **105**, 27 895–27 915.

Daines, M. J. and Kohlstedt, D. L. (1997). Influence of deformation on melt topology in peridotites. *J. Geophys. Res.*, **102**, 10 257–10 271.

Dash, J. G., Fu, H. Y., and Wettlaufer, J. S. (1995). The premelting of ice and its environmental consequences. *Rep. Prog. Phys.*, **58**, 115–167.

Dieckmann, R. and Schmalzried, H. (1977a). Defects and cation diffusion in magnetite (I). *Ber. Bunsenges. Phys. Chem.*, **81**, 344–347.

Dieckmann, R. and Schmalzried, H. (1977b). Defects and cation diffusion in magnetite (II). *Ber. Bunsenges. Phys. Chem.*, **81**, 414–419.

Dieckmann, R., Mason, T. O., Hodge, J. D., and Schmalzried, H. (1978). Defects and cation diffusion in magnetite (III). Tracer diffusion of foreign cations as a function of temperature and oxygen potential. *Ber. Bunsenges. Phys. Chem.*, **82**, 778–783.

Dimanov, A., Lavie, M. P., Dresen, G., Ingrin, J., and Jaoul, O. (2003). Creep of polycrystalline anorthite and diopside. *J. Geophys. Res.*, **108**, 2061, doi:10.1029/2002JB001815.

Dimos, D., Wolfenstine, J., and Kohlstedt, D. L. (1988). Kinetic demixing and decomposition of multicomponent oxides due to a nonhydrostatic stress. *Acta Met.*, **36**, 1543–1552.

Dohmen, R., Chakraborty, S., and Becker, H.-W. (2002). Si and O diffusion in olivine and implications for characterizing plastic flow in the mantle. *Geophys. Res. Lett.*, **29**, 2030, doi:10.1029/2002GL015480.

Dombard, A. J. and McKinnon, W. B. (2000). Long-term retention of impact crater topography on Ganymede. *Geophys. Res. Lett.*, **27**, 3663–3666.

Dombard, A. J. and McKinnon, W. B. (2001). Formation of grooved terrain on Ganymede: Extensional instability mediated by cold, superplastic creep. *Icarus*, **154**, 321–336.

Durham, W. B. and Stern, L. A. (2001). Rheological properties of water ice: Applications to satellites of the outer planets. *Annu. Rev. Earth Planet. Sci.*, **29**, 295–330.

Durham, W. B., Heard, H. C., and Kirby, S. H. (1983). Experimental deformation of polycrystalline H_2O ice at high pressure and low temperature: Preliminary results. *J. Geophys. Res.*, **88**, 377–392.

Durham, W. B., Ricoult, D. L., and Kohlstedt, D. L. (1985). Interaction of slip systems in olivine. In *Point Defects in Minerals*, ed. R. N. Schock, Washington, DC: American Geophysical Union, pp. 185−193.

Durham, W. B., Kirby, S. H., and Stern, L. A. (1997). Creep of water ices at planetary conditions: A compilation. *J. Geophys. Res.*, **102**, 16 293–16 302.

Durham, W. B., Kirby, S. H., and Stern, L. A. (2001). Rheology of ice I at low stress and elevated confining pressure. *J. Geophys. Res.*, **106**, 11 031–11 042.

Duval, P., Ashby, M. F., and Anderman, I. (1983). Rate-controlling processes in the creep of polycrystalline ice. *J. Phys. Chem.*, **87**, 4066–4074.

Einstein, A. (1906). Eine neue Bestimmung der Molekuldimensionen. *Annu. Phys.*, **19**, 289–306.

Einstein, A. (1911). Berichtigung zu meiner Arbeit: eine neue Bestimmung der Molekuldimensionen. *Annu. Phys.*, **34**, 591–592.

Elliot, D. (1973). Diffusion flow laws in metamorphic rocks. *Geol. Soc. Am. Bull.*, **84**, 2645–2664.

Escartin, J., Hirth, G., and Evans, B. (1997). Effects of serpentinization on the lithospheric strength and style of normal faulting at slow-spreading ridges. *Earth Planet. Sci. Lett.*, **151**, 181–189.

Evans, B. and Goetze, C. (1979). The temperature variation of hardness of olivine and its implications for polycrystalline yield stress. *J. Geophys. Res.*, **84**, 5505–5524.

Evans, B. and Kohlstedt, D. L. (1995). Rheology of rocks. In *Rock Physics and Phase Relations: A Handbook of Physical Constants*, ed. T. J. Ahrens, Washington, DC: American Geophysical Union, pp. 148–165.

Faul, U. and Jackson, I. (2006). The effect of melt on the creep strength of polycrystalline olivine (abs.). *Eos Trans. AGU*, **87**, Fall Meet. Suppl., MR11B-0129.

Flack, C. A. and Klemperer, S. L. (1990). Reflections from mantle fault zones around the British Isles. *Geology*, **18**, 528–532.

Gaetani, G. A. and Grove, T. L. (1999). Wetting of olivine by sulfide melt: Implications for Re/Os ratios in mantle peridotite and late-stage core formation. *Earth Planet. Sci. Lett.*, **169**, 147–163.

Gerard, O. and Jaoul, O. (1989). Oxygen diffusion in San Carlos olivine. *J. Geophys. Res.*, **94**, 4119–4128.

Gifkins, R. C. (1972). Grain boundary sliding and its accommodation during creep and superplasticity. *Metall. Trans.*, **7A**, 1225–1232.

Glen, J. W. (1952). Experiments on the deformation of ice. *J. Glaciol.*, **2**, 111–114.

Glen, J. W. (1955). The creep of polycrystalline ice. *Proc. R. Soc. Lond. Ser. A*, **228**, 519–538.

Gleason, G. C. and Tullis, J. (1995). A flow law for dislocation creep of quartz aggregates determined with the molten salt cell. *Tectonophysics*, **247**, 1–23.

Goetze, C. (1978). The mechanisms of creep in olivine. *Philos. Trans. R. Soc. Lond. A*, **288**, 99–119.

Goetze, C. and Evans, B. (1979). Stress and temperature in the bending lithosphere as constrained by experimental rock mechanics. *Geophys. J. R. Astron. Soc.*, **59**, 463–478.

Goldsby, D. L. (2006). Superplastic flow of ice relevant to glacier and ice sheet mechanics. In *Glacier Science and Environmental Change*, ed. P. Knight, Oxford, Blackwell Publishing, pp. 308–314.

Goldsby, D. L. and Kohlstedt, D. L. (2001). Superplastic flow of ice: Experimental observations. *J. Geophys. Res.*, **106**, 11 017–11 030.

Greskovich, C. and Schmalzried, H. (1970). Non-stoichiometry and electronic defects in Co_2SiO_4 and in $CoAl_2O_4$-$MgAl_2O_4$ crystalline solutions. *J. Phys. Chem. Solids*, **31**, 639–646.

Groves, G. W. and Kelly, A. (1969). Change of shape due to dislocation climb. *Philos. Mag.*, **19**, 977–986.

Gust, M., Goo, G., Wolfenstine, J., and Mecartney, M. (1993). Influence of amorphous grain boundary phases on the superplastic behavior of 3-mol%-yttria- stabilized tetragonal zirconia polycrystals (3Y-TZP). *J. Am. Ceram. Soc.*, **76**, 1681–1690.

Hager, B. H. (1991). Mantle viscosity: A comparison of models from postglacial rebound and from the geoid, plate driving forces, and advected heat flux. In *Glacial Isostasy, Sea-Level and Mantle Rheology*, ed. R. Sabadini *et al.*, Dordrecht: Kluwer Academic Publishers, pp. 493–513.

Hercule, S. and Ingrin, J., (1999). Hydrogen in diopside: Diffusion, kinetics of extraction-incorporation, and solubility. *Am. Min.*, **84**, 1577–1587.

Hermeling, J. and Schmalzried, H. (1984). Tracer diffusion of the Fe cations in olivine $(Fe_xMg_{1-x})_2SiO_4$ (III). *Phys. Chem. Miner.*, **11**, 161–166.

Herrick, R. R. and Phillips, R. J. (1992). Geological correlations with the interior density structure of Venus. *J. Geophys. Res.*, **97**, 16 017–16 034.

Herrick, D. L. and Stevenson, D. J. (1990). Extensional and compressional instabilities in icy satellite lithospheres. *Icarus*, **85**, 191–204.

Herring, C. (1950). Diffusional viscosity of a polycrystalline solid. *J. Appl. Phys.*, **21**, 437–445.

Hier-Majumder, S. and Kohlstedt, D. L. (2006). Role of dynamic grain boundary wetting in fluid circulation beneath volcanic arcs. *Geophys. Res. Lett.*, **33**, L08305, doi:10.1029/2006GL025716.

Hier-Majumder, S., Anderson, I. M., and Kohlstedt, D. L. (2005). Influence of protons on Fe-Mg interdiffusion in olivine. *J. Geophys. Res.*, **110**, B02202, doi:10.1029/2004JB003292.

Hirth, G. and Kohlstedt, D. L. (1995a). Experimental constraints on the dynamics of the partially molten upper mantle: Deformation in the diffusion creep regime. *J. Geophys. Res.*, **100**, 1981–2001.

Hirth, G. and Kohlstedt, D. L. (1995b). Experimental constraints on the dynamics of the partially molten upper mantle: Deformation in the dislocation creep regime. *J. Geophys. Res.*, **100**, 15 441–15 449.

Hirth, G. and Kohlstedt, D. L. (1996). Water in the oceanic upper mantle: Implications for rheology, melt extraction and the evolution of the lithosphere. *Earth Planet. Sci. Lett.*, **144**, 93–108.

Hirth, G. and Kohlstedt, D. L. (2003). Rheology of the upper mantle and the mantle wedge: A view from the experimentalists. In *Inside the Subduction Factory*, Geophysical Monograph 138, ed. J. Eiler, Washington, D.C., American Geophysical Union, pp. 83–105.

Holness, M. B. (1993). Temperature and pressure dependence of quartz-aqueous fluid dihedral angles: The control of adsorbed H_2O on the permeability of quartzites. *Earth Planet. Sci. Lett.*, **117**, 363–377.

Holness, M. B. and Graham, C. M. (1991). Equilibrium dihedral angles in the system H_2O-CO_2-NaCl-calcite, and implications for fluid flow during metamorphism. *Contrib. Mineral. Petrol.*, **108**, 368–383.

Holtzman, B. K., Groebner, N. J., Zimmerman, M. E., Ginsberg, S. B., and Kohlstedt, D. L. (2003a). Deformation-driven melt segregation in partially molten rocks. *Geochem., Geophys., Geosyst.*, **4**, 8607, doi:10.1029/2001GC000258.

Holtzman, B. K., Kohlstedt, D. L., Zimmerman, M. E., Heidelbach, F., Hiraga, T., and Hustoft, J. (2003b). Melt segregation and strain partitioning: Implications for seismic anisotropy and mantle flow. *Science*, **301**, 1227–1230.

Houlier, B., Cheraghmakani, M., and Jaoul, O. (1990). Silicon diffusion in San Carlos olivine. *Phys. Earth Planet. Inter.*, **62**, 329–340.

Hustoft, J. W. and Kohlstedt, D. L. (2006). Metal-silicate segregation in deforming dunitic rocks. *Geochem., Geophys., Geosyst.*, **7**, Q02001, doi:10.1029/2005GC001048.

Ito, G., Lin, J., and Graham, D. (2003). Observational and theoretical studies of the dynamics of mantle plume-mid-ocean ridge interaction. *Rev. Geophys.*, **41**, 1017, doi:10.1029/2002RG000117.

Iverson, N. R. (2006). Laboratory experiments in glaciology. In *Glacier Science and Environmental Change*, ed. P. Knight, Oxford, Blackwell Publishing, pp. 449–458.

Jaoul, O. (1990). Multicomponent diffusion and creep in olivine. *J. Geophys. Res.*, **95**, 17 631–17 642.

Jaoul, O., Bertran-Alvarez, Y., Liebermann, R. C., and Price, G. D. (1995). Fe-Mg interdiffusion in olivine up to 9 GPa at $T = 600$–$900\,^{\circ}C$: Experimental data and comparison with defect calculations. *Phys. Earth Planet. Inter.*, **89**, 199–218.

Jin, Z. M., Bai, Q., and Kohlstedt, D. L. (1994). Creep of olivine crystals from four localities. *Phys. Earth Planet. Inter.*, **82**, 55–64.

Kaibyshev, O. (1992). *Superplasticity of Alloys, Intermetallides, and Ceramics*. New York, Springer-Verlag.

Karato, S.-I. (1986). Does partial melting reduce the creep strength of the upper mantle? *Nature*, **319**, 309–310.

Karato, S.-I. and Jung, H. (2003). Effects of pressure on high-temperature dislocation creep in olivine. *Philos. Mag.*, **83**, 401–414.

Karato, S.-I., Paterson, M. S., and Fitz Gerald, J. D. (1986). Rheology of synthetic olivine aggregates: Influence of grain size and water. *J. Geophys. Res.*, **91**, 8151–8176.

Kaufmann, G. and Lambeck, K. (2002). Glacial isostatic adjustment and the radial viscosity profile from inverse modeling. *J. Geophys. Res.*, **107**, 2280, doi:10.1029/2001JB000941.

Kaula, W. M. (1990). Venus: A contrast in evolution to Earth. *Science*, **247**, 1191–1196.

Keefner, J. W., Mackwell, S. J., and Kohlstedt, D. L. (2005). Dunite viscosity dependence on oxygen fugacity (abs.). *Lunar Planet. Sci. Conf. XXXVI*, 1915.

Kelemen, P. B., Hirth, G., Shimizu, N., Spiegelman, M., and Dick, H. J. B. (1997). A review of melt migration processes in the adiabatically upwelling mantle beneath spreading ridges. *Philos. Trans. R. Soc. Lond. A*, **355**, 283–318.

Keszthelyi, L. and McEwen, A. (1997). Magmatic differentiation of Io. *Icarus*, **130**, 437–448.

Kohlstedt, D. L. (1992). Structure, rheology and permeability of partially molten rocks at low melt fractions. In *Mantle Flow and Melt Generation at Mid-Ocean Ridges*,

Monograph 71, ed. J. Phipps-Morgan, D. K. Blackman and J. M. Sinton. Washington, DC: American Geophysical Union. pp. 103–121.

Kohlstedt, D. L. (2002). Partial melting and deformation. In *Plastic Deformation in Minerals and Rocks*, ed. S. I. Karato and H. R. Wenk. Reviews in Mineralogy and Geochemistry, Vol. 51, Mineralogical Society of America, pp. 105–125.

Kohlstedt, D. L. (2006). Water and rock deformation: The case for and against a climb-controlled creep rate. In *Water in Nominally Anhydrous Minerals*, ed. H. Keppler and J. R. Smyth. Reviews in Mineralogy and Geochemistry, Vol. 62, ser. ed. J. J. Rosso, Mineralogical Society of America, pp. 377–396.

Kohlstedt, D. L. (2007). Properties of rocks and minerals: constitutive equations, rheological behavior, and viscosity of rocks. In *Treatise on Geophysics*, ed. G. Schubert. Vol. 2.14. Oxford: Elsevier, pp. 389–417.

Kohlstedt, D. L. and Holtzman, B. K. (2009). Shearing melt out of the Earth: An experimentalist's perspective on the influence of deformation on melt extraction. *Annu. Rev. Earth Planet. Sci.*, **37**, 561–593, doi:10.1146/annurev.earth.031208.100104.

Kohlstedt, D. L. and Hornack, P. (1981). The effect of oxygen partial pressure on creep in olivine. In *Anelasticity in the Earth, Geodynamic Series*, 4, ed. F. D. Stacey, M. S. Paterson and A. Nicolas. Washington, American Geophysical Union, pp. 101−107.

Kohlstedt, D. L. and Mackwell, S. J. (1998). Diffusion of hydrogen and intrinsic point defects in olivine. *Z. Phys. Chem.*, **207**, 147–162.

Kohlstedt, D. L. and Mackwell, S. J. (1999). Solubility and diffusion of 'water' in silicate minerals. In *Microscopic Processes in Minerals*, ed. K. Wright and C. R. A. Catlow, NATO-ASI Series. Dordrecht, Kluwer Academic Publisher, pp. 539–559.

Kohlstedt, D. L. and Ricoult, D. L. (1984). High-temperature creep of olivines. In *Deformation of Ceramics II*, ed. R. E. Tressler and R. C. Bradt. New York, Plenum Publishing, pp. 251−280.

Kohlstedt, D. L. and Zimmerman, M. E. (1996). Rheology of partially molten mantle rocks. *Annu. Rev. Earth Planet. Sci.*, **24**, 41–62.

Kohlstedt, D. L., Evans, B., and Mackwell, S. J. (1995). Strength of the lithosphere: Constraints imposed by laboratory experiments. *J. Geophys. Res.*, **100**, 17 587–17 602.

Kröger, F. A. and Vink, H. J. (1956). Relation between the concentration of imperfections in crystalline solids. In *Solid State Physics 3*, ed. F. Seitz and D. Turnball. New York, Academic Press, pp. 367–435.

Langdon, T. G. (1994). A unified approach to grain boundary sliding in creep and superplasticity. *Acta Met.*, **42**, 2437–2443.

Lange, F. F., Davis, B. I., and Clarke, D. R. (1980). Compressive creep of Si_3N_4/MgO alloys. Part 1: Effect of composition. *J. Mater. Sci.*, **15**, 601–610.

Lee, V., Mackwell, S. J., and Brantley, S. L. (1991). The effect of fluid chemistry on wetting textures in novaculite. *J. Geophys. Res.*, **96**, 10 023–10 037.

Liftshitz, I. M. (1963). On the theory of diffusion-viscous flow of polycrystalline bodies. *Soviet Phys. JETP*, **17**, 909–920.

Lopes, R. M. C., Kamp, L. W., Douté, S., Smythe, W. D., Carlson, R. W., McEwen, A. S., Geissler, P. E., Kieffer, S. W., Leader, F. E., Davies, A. G., Barbinis, E., Mehlman, R., Segura, M., Shirley, J., and Soderblom, L. A. (2001). Io in the near-infrared: NIMS results from the Galileo flybys in 1999 and 2000. *J. Geophys. Res.*, **106**, 33 053–33 078.

Mackwell, S. J. and Kohlstedt, D. L. (1990). Diffusion of hydrogen in olivine: Implications for water in the mantle. *J. Geophys. Res.*, **95**, 5079–5088.

Mackwell, S. J., Kohlstedt, D. L., and Paterson, M. S. (1985). The role of water in the deformation of olivine single crystals. *J. Geophys. Res.*, **90**, 11 319–11 333.

Mackwell, S. J., Zimmerman, M., Kohlstedt, D. L., and Scherber, D. (1995). Experimental deformation of dry Columbia diabase: Implications for tectonics on Venus. In *Proceedings of the 35*th *U.S. Symposium on Rock Mechanics*, ed. J. J. K. Daemen and R. A. Schultz, pp. 207–214.

Mackwell, S. J., Zimmerman, M. E., and Kohlstedt, D. L. (1998). High-temperature deformation of dry diabase with application to tectonics on Venus. *J. Geophys. Res.*, **103**, 975–984.

McGarr, A. (1984). Scaling of ground motion parameters, state of stress, and focal depth. *J. Geophys. Res.*, **89**, 6969–6979.

McGarr, A., Zoback, M. D., and Hanks, T. C. (1982). Implications of an elastic analysis of in situ stress measurements near the San Andreas fault. *J. Geophys. Res.*, **87**, 7797–7806.

McKenzie, D. (1984). The generation and compaction of partially molten rock. *J. Petrol.*, **25**, 713–765.

McKinnon, W. B. (1999). Convective instability in Europa's floating ice shell. *Geophys. Res. Lett.*, **26**, 951–954.

Mei, S. and Kohlstedt, D. L. (2000a). Influence of water on plastic deformation of olivine: 1. Diffusion creep regime. *J. Geophys. Res.*, **105**, 21 457–21 469.

Mei, S. and Kohlstedt, D. L. (2000b). Influence of water on plastic deformation of olivine: 2. Dislocation creep regime. *J. Geophys. Res.*, **105**, 21 471–21 481.

Mei, S., Bai, W., Hiraga, T., and Kohlstedt, D. L. (2002). Influence of water on plastic deformation of olivine-basalt aggregates. *Earth Planet. Sci. Lett.*, **201**, 491–507.

Mibe, K., Fujii, T., and Yasuda, A. (1998). Connectivity of aqueous fluid in the Earth's upper mantle. *Geophys. Res. Lett.*, **25**, 1233–1236.

Minarik, W. G., Ryerson, F. J., and Watson, E. B. (1996). Textural entrapment of core-forming melts. *Science*, **272**, 530–533.

Misener, D. J. (1974). Cationic diffusion in olivine to 1400 °C and 35 kbar. In *Geochemical Transport and Kinetics*, ed. A. W. Hofmann, B. J. Giletti, H. S. Yoder Jr. and R. A. Yund. Washington, DC: Carnegie Institution of Washington, pp. 117–129.

Montési, L. G. J. and Hirth, G. (2003). Grain size evolution and the rheology of ductile shear zones: From laboratory experiments to postseismic creep. *Earth Planet. Sci. Lett.*, **211**, 97–110.

Montési, L. G. J. and Zuber, M. T. (2002). A unified description of localization for application to large-scale tectonics. *J. Geophys. Res.*, **107**, doi:10.1029/2001JB000465.

Nabarro, F. (1948). Deformation of crystals by the motion of single ions. In *Report on a Conference on the Strength of Solids*. London, Physical Society, pp. 75–90.

Nakamura, A. and Schmalzried, H. (1984). On the Fe^{2+}-Mg^{2+} interdiffusion in olivine (II). *Ber. Bunsenges. Phys. Chem.*, **88**, 140–145.

Panasyuk, S. V. and Hager, B. H. (2000). Inversion for mantle viscosity profiles constrained by dynamic topography and the geoid, and their estimated errors. *Geophys. J. Int.*, **143**, 821–836.

Passey, Q. R. and Schoemaker, E. M. (1982). Craters and basins on Ganymede and Callisto: Morphological indicators of crustal evolution. In *Satellites of Jupiter*, ed. D. Morrison and M. S. Matthews. Tucson, University of Arizona Press, pp. 379–434.

Paterson, M. S. (1969). The ductility of rocks. In *Physics of Strength and Plasticity*, ed. A. S. Argon. Cambridge, MA, MIT Press, pp. 377–392.

Peltier, W. R. (1998). Global glacial isostasy and relative sea level: Implications for solid earth geophysics and climate system dynamics. In *Dynamics of the Ice Age Earth*, ed. P. Wu. Switzerland: Trans Tech Publications, pp. 17–54.

Phillips, R. J., Johnson, C. L., Mackwell, S. J., Morgan, P., Sandwell, D. T., and Zuber, M. T. (1997). Lithospheric mechanics and dynamics of Venus. In *Venus II*, ed. S. W. Bougher, D. M. Hunten and R. J. Phillips. Tucson, AZ: University of Arizona Press, pp. 1163–1204.

Morgan, J. P. (1997). The generation of a compositional lithosphere by mid-ocean ridge melting and its effect on subsequent off-axis hotspot upwelling and melting. *Earth Planet. Sci. Lett.*, **146**, 213–232.

Pitzer, K. S. and Sterner, S. M. (1994). Equations of state valid continuously from zero to extreme pressures for H_2O and CO_2. *J. Chem. Phys.*, **101**, 3111–3116.

Poirier, J.-P. (1985). *Creep of Crystals: High-temperature Deformation Processes in Metals, Ceramics and Minerals*. Cambridge, Cambridge University Press.

Post, A. D., Tullis, J., and Yund, R. A. (1996). Effects of chemical environment on dislocation creep of quartzite. *J. Geophys. Res.*, **101**, 22 143–22 155.

Raj, R. (1982). Creep in polycrystalline aggregates by matter transport through a liquid phase. *J. Geophys. Res.*, **87**, 4731–4739.

Raj, R. and Ashby, M. F. (1971). On grain boundary sliding and diffusional creep. *Metall. Trans.*, **2**, 1113–1127.

Ramsey, J. G. (1980). Shear zone geometry: A review. *J. Structural Geol.*, **2**, 83–99.

Ranero, C. R., Phipps Morgan, J., McIntosh, K., and Reichert, C. (2003). Bending-related faulting and mantle serpentinization at the Middle America Trench. *Nature*, **425**, 367–373.

Reese, C. C., Solomatov, V. S., and Moresi, L.-N. (1998). Heat transport efficiency for stagnant lid convection with dislocation viscosity: Application to Mars and Venus. *J. Geophys. Res.*, **103**, 13 643–13 658.

Regenauer-Lieb, K. and Kohl, T. (2003). Water solubility and diffusivity in olivine: Its role for planetary tectonics. *Mineral. Mag.*, **67**, 697–717.

Regenauer-Lieb, K., Yuen, D. A., and Branlund, J. (2001). The initiation of subduction: Criticality by addition of water? *Science*, **294**, 578–580.

Reston, T. J. (1990). Mantle shear zones and the evolution of the northern North Sea basin. *Geology*, **18**, 272–275.

Ricoult, D. L. and Kohlstedt, D. L. (1983). Structural width of low-angle grain boundaries in olivine. *Phys. Chem. Minerals*, **9**, 133–138.

Ricoult, D. L. and Kohlstedt, D. L. (1985). Creep of Co_2SiO_4 and Fe_2SiO_4 crystals in a controlled thermodynamic environment. *Philos. Mag. A*, **51**, 79–93.

Roscoe, R. (1952). The viscosity of suspensions of rigid spheres. *Brit. J. Appl. Phys.*, **3**, 267–269.

Ross, J. V. and Nielsen, K. C. (1978). High-temperature flow of wet polycrystalline enstatite. *Tectonophys.*, **44**, 233–261.

Ross, M. and Schubert, G. (1985). Tidally forced viscous heating in a partially molten Io. *Icarus*, **64**, 391–400.

Ross, M. and Schubert, G. (1986). Tidal dissipation in a viscoelastic planet. *J. Geophys. Res.*, **91**, 447–452.

Rubie, D. C., Gessmann, C. K., and Frost, D. J. (2004). Partitioning of oxygen during core formation on the Earth and Mars. *Nature*, **429**, 58–61.

Ruiz, J. and Tejero, R. (2000). Heat flows through the ice lithosphere of Europa. *Geophys. Res. Lett.*, **105**, 29 283–29 289.

Ruiz, J. and Tejero, R. (2003). Heat flow, lenticulae spacing, and possibility of convection in the ice shell of Europa. *Icarus*, **162**, 362–373.

Ruoff, A. L. (1965). Mass transfer problems in ionic crystals with charge neutrality. *J. Appl. Phys.*, **36**, 2903–2907.

Rutter, E. H. (1976). The kinetics of rock deformation by pressure solution. *Philos. Trans. R. Soc. Lond. A*283, 203–219.

Rybacki, E. and Dresen, G. (2000). Dislocation and diffusion creep of synthetic anorthite aggregates. *J. Geophys. Res.*, **105**, 26 017–26 036.

Ryerson, F. J., Durham, W. B., Cherniak, D. J., and Lanford, W. A. (1989). Oxygen diffusion in olivine: Effect of oxygen fugacity and implications for creep. *J. Geophys. Res.*, **94**, 4105–4118.

Schenk, P. M. (2002). Thickness constraints on the icy shells of Galilean satellites from a comparison of crater shapes. *Nature*, **417**, 419–421.

Schmalzried, H. (1978). Reactivity and point defects of double oxides with emphasis on simple silicates. *Phys. Chem. Minerals*, **2**, 279–294.

Schmalzried, H. (1981). *Solid State Reactions*. Weinheim, Verlag Chemie, pp. 37–57; 174–175.

Schamzlried, H. (1995). *Chemical Kinetics of Solids*. New York, VCH Publishers, pp. 27–37.

Scott, D. R. and Stevenson, D. J. (1986). Magma ascent by porous flow. *J. Geophys. Res.*, **91**, 9283–9296.

Scott, T. and Kohlstedt, D. L. (2006). The effect of large melt fraction on the deformation behavior of peridotite. *Earth Planet. Sci. Lett.*, **246**, 177–187.

Segatz, M., Spohn, T., Ross, M. N., and Schubert, G. (1988). Tidal dissipation, surface heat flow, and figure of viscoelastic models of Io. *Icarus*, **75**, 187–206.

Shelton, G. and Tullis, J. (1981). Experimental flow laws for crustal rocks (abs.). *Eos Trans. AGU*, **62**, 396.

Shewmon, P. G. (1983). *Diffusion in Solids*. Jenks, OK, J. Williams Book Company, pp. 155–160.

Sibson, R. H. (1974). Frictional constraints on thrust, wrench and normal faults. *Nature*, **249**, 542–544.

Sibson, R. H. (1977). Fault rocks and fault mechanisms. *J. Geol. Soc. London*, **133**, 191–213.

Sockel, H. G. (1974). Defect structure and electrical conductivity of crystalline ferrous silicate. In *Defects and Transport in Oxides*, ed. M. S. Seltzer and R. I. Jaffe. New York, Plenum Press, pp. 341–354.

Solomatov, V. S. and Moresi, L.-N. (2000). Scaling of time-dependent stagnant lid convection: Application to small-scale convection on Earth and other terrestrial planets. *J. Geophys. Res.*, **105**, 21 795–21 818, doi:10.1029/2000JB900197.

Stalder, R. and Skogby, H. (2002). Hydrogen incorporation in enstatite. *Eur. J. Mineral.*, **14**, 1139–1144.

Stern, L. A., Durham, W. B., and Kirby, S. H. (1997). Grain-sized-induced weakening of H_2O ices I and II and associated anisotropic recrystallization. *J. Geophys. Res.*, **102**, 5313–5325.

Tackley, P., Schubert, G., Glatzmaier, G. A., Schenk, P., Ratcliff, J. T., and Matas, J.-P. (2001). Three-dimensional simulations of mantle convection in Io. *Icarus*, **149**, 79–93.

Takei, Y. (1998). Constitutive mechanical relations of solid-liquid composites in terms of grain-boundary contiguity. *J. Geophys. Res.*, **103**, 18 183–18 203.
Takei, Y. (2000). Acoustic properties of partially molten media studied on a simple binary system with a controllable dihedral angle. *J. Geophys. Res.*, **105**, 16 665–16 682.
Takei, Y. (2001). Stress-induced anisotropy of partially molten media inferred from experimental deformation of a simple binary system under acoustic monitoring. *J. Geophys. Res.*, **106**, 567–588.
Takei, Y. (2002). Effect of pore geometry on V_P/V_S: From equilibrium geometry to crack. *J. Geophys. Res.*, **107**(B21), 2043, 10.1029/2001JB000522.
Takei, Y. and Holtzman, B. K. (2009a). Viscous constitutive relations of solid–liquid composites in terms of grain-boundary contiguity: I. Grain boundary diffusion-control model. *J. Geophys. Res.*, **114**, B06205, doi:10.1029/2008JB005850.
Takei, Y. and Holtzman, B. K. (2009b). Viscous constitutive relations of solid–liquid composites in terms of grain-boundary contiguity: II. Compositional model for small melt fractions. *J. Geophys. Res.*, **114**, B06206, doi:10.1029/2008JB005851.
Takei, Y. and Holtzman, B. K. (2009c). Viscous constitutive relations of solid–liquid composites in terms of grain-boundary contiguity: III. Causes and consequences of viscous anisotropy. *J. Geophys. Res.*, **114**, B06207, doi:10.1029/2008JB005852.
Takei, Y. and Shimizu, I. (2003). The effects of liquid composition, temperature, and pressure on the equilibrium dihedral angles of binary solid–liquid systems inferred from a lattice-like model. *Phys. Earth Planet. Inter.*, **139**, 225–242.
Tharp, T. M. (1983). Analogies between the high-temperature deformation of polyphase rocks and the mechanical behavior of porous powder metal. *Tectonophys.*, **96**, T1-T11.
Toramaru, A. and Fujii, N. (1986). Connectivity of melt phase in a partially molten peridotite. *J. Geophys. Res.*, **91**, 9239–9252.
Turcotte, D. L. (1993). An episodic hypothesis for Venusian tectonics. *J. Geophys. Res.*, **98**, 17 061–17 068.
Turcotte, D. L. (1995). How does Venus lose heat? *J. Geophys. Res.*, **100**, 16 931–16 940.
Turcotte, D. L. and Schubert, G. (1982). *Geodynamics: Applications of Continuum Physics to Geological Problems*. New York, John Wiley, pp. 163–167; 383–384.
van der Wal, D., Chopra, P. N., Drury, M., and Fitz Gerald, J. D. (1993). Relationships between dynamically recrystallized grain size and deformation conditions in experimentally deformed olivine rocks. *Geophys. Res. Lett.*, **20**, 1479–1482.
von Bargen, N. and Waff, H. S. (1986). Permeabilities, interfacial areas and curvatures of partially molten systems: Results of numerical computations of equilibrium microstructures. *J. Geophys. Res.*, **91**, 9261–9276.
von Mises, R. (1928). Mechanik der plastischen Formänderung von Kristallen. *Z. Angew. Math. Mech.*, **8**, 161–185.
Waff, H. S. and Bulau, J. R. (1979). Equilibrium fluid distribution in an ultramafic partial melt under hydrostatic stress conditions. *J. Geophys. Res.*, **84**, 6109–6114.
Waff, H. S. and Faul, U. H. (1992). Effects of crystalline anisotropy on fluid distribution in ultramafic partial melts. *J. Geophys. Res.*, **97**, 9003–9014.
Wang, Z. (2002). Effect of pressure and water on the kinetics properties of olivine, Ph.D. thesis, University of Minnesota.
Wang, Z., Hiraga, T., and Kohlstedt, D. L. (2004). Effect of H^+ on Fe-Mg interdiffusion in olivine, $(Mg,Fe)_2SiO_4$. *Appl. Phys. Lett.*, **85**, 209–211.
Wang, L. and Zhang, Y. (1996). Diffusion of the hydrous component in garnet. *Am. Min.*, **81**, 706–718.

Watson, E. B. and Brenan, J. M. (1987). Fluids in the lithosphere: 1. Experimentally determined wetting characteristics of CO_2-H_2O fluids and their implications for fluid transport, host-rock physical properties, and fluid inclusion formation. *Earth Planet. Sci. Lett.*, **85**, 497–515.

Weertman, J. (1968). Dislocation climb theory of steady-state creep. *Trans. Am. Soc. Metals*, **61**, 681–694.

Weertman, J. (1970). The creep strength of the Earth's mantle. *Rev. Geophys. Space Phys.*, **8**, 145–168.

Weertman, J. (1983). Creep deformation of ice. *Annu. Rev. Earth Planet. Sci.*, **11**, 215–240.

Weertman, J. (1999). Microstructural mechanisms in creep. In *Mechanics and Materials: Fundamentals and Linkages*, ed. M. A. Meyers, R. W. Armstrong and H. Kirchner. New York: John Wiley and Sons, pp. 451–488.

Weertman, J. and Weertman, J. R. (1975). High temperature creep of rock and mantle viscosity. *Annu. Rev. Earth Planet. Sci.*, **3**, 293–315.

Woods, S. (2000). The kinetics of hydrogen diffusion in single crystal enstatite. Ph.D. thesis, Pennsylvania State University.

Xu, Y., Zimmerman, M. E., and Kohlstedt, D. L. (2004). Deformation behavior of partially molten mantle rocks. In *Rheology and Deformation of the Lithosphere at Continental Margins*. MARGINS Theoretical and Experimental Earth Science Series, Vol. I. ed. G. D. Karner, N. W. Driscoll, B. Taylor and D. L. Kohlstedt. Columbia University Press, pp. 284–310.

Zahnle, K., Dones, L., and Levison, H. F. (1998). Cratering rates on Galilean satellites. *Icarus*, **136**, 202–222.

Zhao, Y. H., Ginsberg, S. G., and Kohlstedt, D. L. (2004). Solubility of hydrogen in olivine: Effects of temperature and Fe content. *Contrib. Mineral. Petrol.*, **147**, 155–161, doi:10.1007/s00410-003-0524-4.

Zhao, Y.-H., Zimmerman, M. E., and Kohlstedt, D. L. (2009). Effect of iron content on the creep behavior of olivine: 1. Anhydrous conditions, *Earth Planet. Sci. Lett.* **287**, 229–240, doi:10.1016/j.epsl.2009.08.006.

Zimmerman, M. E. and Kohlstedt, D. L. (2004). Rheological properties of partially molten lherzolite. *J. Petrol.*, **45**, 275–298.

Zimmerman, M. E., Zhang, S., Kohlstedt, D. L., and Karato, S. (1999). Melt distribution in mantle rocks deformed in shear. *Geophys. Res. Lett.*, **26**, 1505–1508.